Nonlinear effects in the Josephson-vortex terahertz photonic crystal

by
Alexander Daniel Wall-Clarke

Doctoral Thesis

Submitted in partial fulfillment of the requirements

for the award of

Doctor of Philosophy

of

Loughborough University

July 2013

Abstract

Analysis has been made of the amplitudes of the second and third harmonics when pumping a discrete frequency ω to the Josephson-vortex photonic crystal within the THz range of the electromagnetic spectrum. The results of numerical simulations show that there are certain resonance frequencies for these harmonics where the amplitudes are strongly enhanced. The frequencies at which these resonances occur can be tuned by an applied magnetic field h_{ab} and tilting the material with respect to the incident radiation. For the second harmonic it has been possible to describe these resonances analytically with a resonance approximation which displays good agreement with numerical simulations at and near the resonances.

A similar perturbative method has been used to simulate the nonlinear mixing of two discrete THz frequencies ω_1 and ω_2 in the JV photonic crystal, producing resonances for harmonics at the sum $\omega_1 + \omega_2$ and the difference $\omega_1 - \omega_2$ of these two input frequencies. This method can allow a high degree of control over the harmonic frequencies produced.

Acknowledgements

It's satisfying to look back over the past few years of research and see how far i've progressed through all of it both academically and personally, things often weren't straight forward but the challenge has been rewarding and well worth it. I'd like to thank my supervisor and collaborator Pf. Sergey Saveliev for his valuable help and guidance during this project.

Thanks also have to go to Loughborough University for the funding which made the research possible. This included a grant from the Physics department to attend the CMMP 2012 conference in Edinburgh and present work from this thesis there.

I also have to thank my fellow PhD students and friends at Loughborough throughout the three years for their support and suggestions, as well as the fun times that helped to keep an important balance of work and relaxation. Lastly thanks to my family who always offered encouragement along the way.

Contents

Chapter 1

Introduction

1.1 The THz gap

The THz frequency range of the electromagnetic spectrum remains the only real region between long wavelength radio waves and short wavelength gamma rays that isn't widely employed in technologies by humankind [1]. The THz gap lies between frequencies of around 0.3-30THz which as a wavelength corresponds to 10-1000μm or a photon energy of 1.25-125meV. As a blackbody colour temperature, THz frequencies range from 14-1400K which importantly includes the temperature range of biological processes and a substantial fraction of the background radiation from the birth of the universe. There are many potential applications for devices that operate at THz frequencies in fields as wide ranging as physics, astronomy, chemistry, biology and medicine [1]. This has led to a rising interest in THz science and technology in order to bridge this gap and open up applications such as THz imaging and spectroscopy, health monitoring, medical diagnosis and tomography [2]. Unlike some other forms of radiation such as X-rays, THz frequencies aren't

believed to be damaging to the human body since photon energies are too low for photoionization of biological material [3]. Fig. 1.1 shows the position of the THz gap in the electromagnetic spectrum between microwave and infra red frequencies.

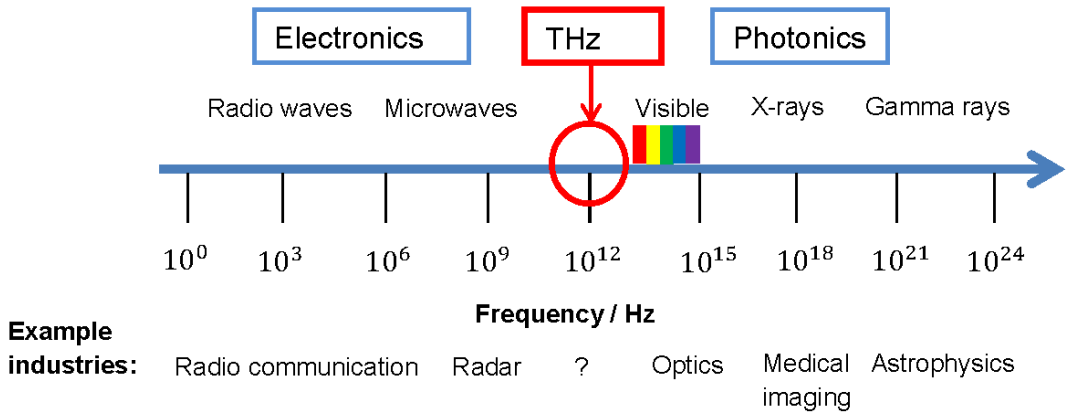

Figure 1.1: Showing the position of the THz gap in the Electromagnetic spectrum as well as some example industries that use different frequencies, figure has been adapted from [2].

There are several optical and electronic (microwave) THz devices currently competing for the THz market [1, 4]. Optical devices can employ several approaches to reduce their frequency. On the other hand, the frequency of microwave devices (usually electronic devices based on semiconductors) has to be increased in order to reach the THz range. Recent advances in nanotechnology have led to the development of electronic THz sources including THz-quantum cascade lasers [5], resonant tunneling diodes [6, 7], THz plasma-wave photomixers [8], and Bloch oscillators [9]. Several types of THz detectors for time-domain systems have been proposed so far, e.g. (i) GaAs used as a photoconductive antenna [10]; (ii) electro-optic sampling techniques for ultrawideband time-domain detection [11]; (iii) a 10-fs-laser

and a thin nonlinear crystal such as GaSe [12]; (iv) deuterated triglycine sulphate crystals [13]; (v) bolometers [14]; (vi) single-electron transistors [15]. THz wave guiding using conventional structures [16], such as metal tubes, plastic ribbons [17] and dielectric fibres has also been demonstrated but due to high losses, some of these devices have limited applications.

1.2 Josephson THz devices : the aims of this thesis

A variety of THz sources, detectors, and waveguides have been proposed and even developed, but despite this there is still a demand for more highly controllable, well-integrated and compact THz devices. Some of the devices mentioned above have problems for applications in miniaturized electronics, they are either too large, not easily assembled together or not frequency tunable. Superconducting devices employing the Josephson effect [18] can now be considered as a prominent candidate to make single chip multi-functional THz devices. Indeed, the growing number of studies [19] of Josephson structures is partly motivated by the THz frequency range of the electromagnetic waves, also known as Josephson plasma waves (JPWs) propagating in these systems [20]. These THz electromagnetic waves interact nonlinearly with the Josephson medium itself and with magnetic flux quanta (Josephson vortices), which, in turn, can be conveniently manipulated by varying an in-plane magnetic field and/or an out-of-plane electric current. Such a level of controllability can be used to propose a set of well-integrated classical and even quantum THz devices [19], including pulse and continuous wave generators,

tunable filters, detectors, wave mixers, lenses, converters, and amplifiers.

In this PhD project the focus has been on basic and advanced mechanisms of filtering THz radiation using nonlinear photonic crystals made of layered superconductors where an applied magnetic field can be used to tune the distance between vortices, hence changing the period of the structure. This important property allows layered superconductors to be switched from fully transparent to fully reflecting for a particular frequency of THz radiation by changing the strength of an applied magnetic field [21]. Thus, the system studied in this project is a tunable filter for THz radiation known as the Josephson-vortex (JV) terahertz photonic crystal , focussing on the nonlinear properties which could have wide application in compact THz devices.

Chapter 2

Review : THz radiation in layered superconductors

It's now appropriate to review some of the published literature on layered superconductors and their interactions with electromagnetic radiation. An important principle affecting the properties of these materials is the Josephson effect [22, 23], which occurs when two superconductors are separated by an insulating barrier. This effect will be reviewed in Section 2.1. These principles, along with Maxwell's equations [24] will be used to derive the sine-Gordon equation [25] in Section 2.1.1 that can describe the evolution of fields in layered superconductors, these equations will be the basis for all subsequent work in this thesis. The relevant solutions to these equations are discussed in Section 2.1.2.

Since this work considers a photonic crystal for THz radiation it makes sense to review the basic properties of photonic crystals [26], this is covered in Chapter 3 whilst some applications of photonic crystals are outlined in Section 3.1. The implications of nonlinearity in a photonic crystal are discussed in Section 3.2. Finally

this is all brought together in Section 3.3, which discusses the linear properties of the Josephson-vortex terahertz photonic crystal, which has been previously investigated [27]. This work has been the basis for the core research of this thesis, which is considering the nonlinear properties of the JV photonic crystal.

2.1 Josephson junctions and electromagnetic radiation

A macroscopic system in a superconducting state can be described by a single wavefunction $\psi = |\psi|e^{i\theta}$ [28]. When two superconductors are in close proximity to each other, Cooper pairs can tunnel through the barrier in between, which makes the two subsystems intervene with each other [29]. The gauge-invariant phase difference $\varphi = \theta_a - \theta_b - \frac{2\pi}{\phi_0}\int_a^b \vec{A}.d\vec{s}$ is important for describing superconductivity where A is the vector potential, $\phi_0 = \frac{hc}{2e}$ is the flux quantum, h is the Plank constant, c the speed of light and e the charge on the electron.

In 1962 Brian Josephson predicted [22, 23, 30] that the current flow associated with coherent quantum tunnelling of Cooper pairs through a barrier between two superconducting electrodes, known as a Josephson junction, is proportional to the sinusoidal function of the phase difference φ. This is known as the dc Josephson relation. He also predicted that the time derivative of the phase difference is proportional to the voltage across the barrier, known as the ac Josephson relation.

The current flow between the two superconductors can be described by the dc Josephson relation given by

$$J = J_c \sin \varphi, \tag{2.1}$$

where J_c is the critical current density, which is the maximum current allowed through a Josephson junction. When a voltage V is applied across the barrier, the phase difference evolves with time following the ac Josephson relation

$$2eV = \hbar \frac{d\varphi}{dt}. \tag{2.2}$$

Here $\hbar = h/2\pi$ is the reduced Plank constant. Josephson junctions can come in different arrangements or geometries which have different physical properties, the one relevant to this work is called the long Josephson junction [31] as shown in Fig. 2.1. In this case the width of the junction is much greater than the so called Josephson penetration depth λ_J. This is the depth to which a magnetic field can penetrate a long Josephson junction and is greater than the London penetration depth λ_L for bulk superconductors.

2.1.1 Derivation of the sine-Gordon equation for Josephson junctions

In this section the basic derivation of the sine-Gordon equation for a single Josephson junction will be shown following the review [28].

The Josephson relations defined in Section 2.1 impose rules for the spatial and temporal variations of the gauge-invariant phase difference (and, thus, the voltage

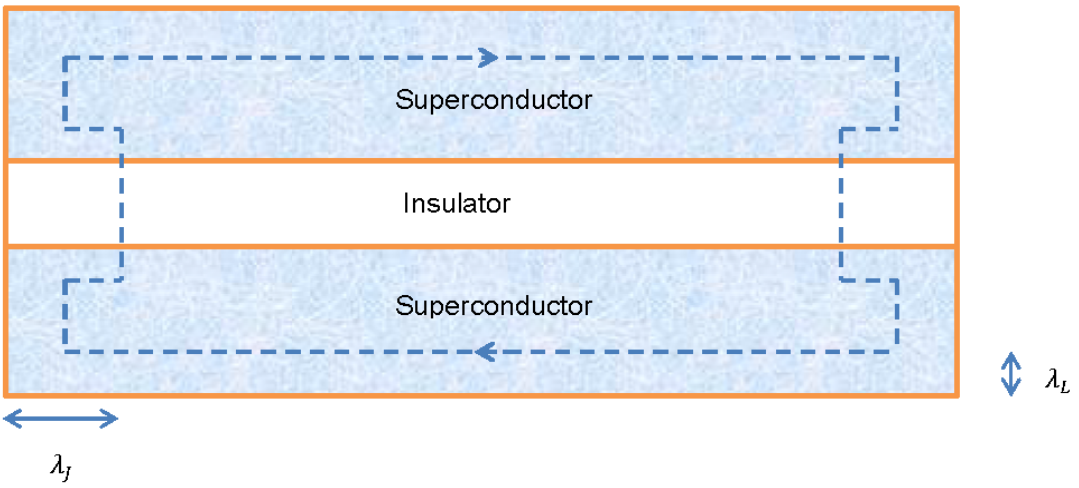

Figure 2.1: Geometry of a long Josephson junction with two superconductors separated by an insulating barrier, where the Josephson penetration depth λ_J is much larger than the London penetration depth λ_L as indicated by the dashed blue line. Figure adapted from [31].

and current in a Josephson junction), since the electric and magnetic fields themselves follow Maxwell's equations. The spatial variation of gauge-invariant phase difference across a Josephson junction with separation d along the z direction is given by

$$\bigtriangledown\varphi = \frac{2\pi(2\lambda + d)}{\phi_0} B \times \hat{z},$$

where $\bigtriangledown = \left(\frac{\partial}{\partial x}, \frac{\partial}{\partial y}\right)$ is the gradient operator in lateral directions, λ is the London penetration depth for an isotropic superconductor and $\hat{z}$ is the unit vector along the z-axis. Using both Maxwell's equation

$$\bigtriangledown \times \vec{B} = \frac{4\pi}{c}\vec{J} + \frac{\epsilon}{c}\frac{\partial \vec{E}}{\partial t},$$

and the current $J^z = \sin\varphi + \sigma V/d$, where the first term is given by the dc Josephson

current and the second term the quasiparticle current with conductivity σ and voltage V. The sine-Gordon equation can be derived, given by Eq. (2.3)

$$\frac{\partial^2\varphi}{\partial x^2}+\frac{\partial^2\varphi}{\partial y^2}+\frac{1}{c'^2}\frac{\partial^2\varphi}{\partial t^2}-\frac{\beta'}{c'^2}\frac{\partial\varphi}{\partial t}=\frac{1}{\lambda_J^2}\sin\varphi \tag{2.3}$$

$c' = \frac{c}{\sqrt{\epsilon(1+2\lambda/d)}}$ is the Swihart velocity(the characteristic maximum velocity for electromagnetic waves in a long Josephson junction), $\lambda_J = \sqrt{c\phi_o/(8\pi^2 J_c(d+2\lambda))}$ the Josephson penetration depth, $\beta' = 4\pi\sigma/\epsilon$. The sine-Gordon equation describes the spatial and temporal evolution of the gauge-invariant phase difference in a Josephson junction.

Neglecting damping and the y dependence of the Josephson phase we can write the sine-Gordon equation (Eq. (2.4)) for a single Josephson junction in the following general form which will be more applicable to the particular problem considered in this thesis

$$(\frac{1}{c'^2}\frac{\partial^2\varphi}{\partial t^2}+\frac{1}{\lambda_J^2}\sin\varphi)-\frac{\partial^2\varphi}{\partial x^2}=0. \tag{2.4}$$

The motivation for these assumptions will be described in more detail when the sine-Gordon equations for layered superconductors are derived in later chapters.

2.1.2 Solutions of the sine-Gordon equation

The sine-Gordon equation allows two types of solutions, the first is a soliton solution representing Josephson vortices (JVs) , given by

$$\varphi = 4\arctan[\exp(x - vt/1 - v^2/(c^{'2})^{1/2})]. \tag{2.5}$$

The physical interpretation of the soliton solutions can be described as follows. In a bulk type-I superconductor the superconducting phase only persists up to a critical applied magnetic field H_c. Above this field strength the Cooper pairs and hence the superconductivity are broken allowing the field to penetrate the material. Type-II superconductors have more complex behaviour, and can also display a vortex state, or mixed state of superconducting and normal phase, where the applied field can penetrate the material in the form of vortices. Abrikosov vortices [32] have a normal (normally conducting) core surrounded by a circulating supercurrrent, typically the magnetic flux of a vortex is equal to the flux quantum ϕ_0.

In a Josephson junction the so-called Josephson vortices [33] can penetrate the material between the superconducting layers when a magnetic field is applied parallel to the layers. Unlike Abrikosov vortices, Josephson vortices have no normal core since the field penetrates the insulating barrier, instead supercurrents circulate around the mathematical center of the vortex.

The second solution to Eq. (2.4) is an oscillating solution representing Josephson plasma waves (JPWs) propagating in a Josephson junction which is given by

$$\varphi = \varphi_0 \exp(iqx - i\omega t + k(q,\omega)y), \tag{2.6}$$

where k is the x-axis wavevector and q the y-axis wavevector of the waves with angular frequency ω and amplitude φ_0. It will be shown in Section 3.3 that Josephson vortices can play a useful role in controlling JPWs.

2.1.3 Linear spectrum of Josephson plasma waves

The transverse linear spectrum $\omega(k)$ of Josephson plasma waves can be written as Eq. (2.7) and is plotted in Fig. 2.2

$$\omega^2 = \omega_J^2 + c'^2 k^2. \tag{2.7}$$

Layered superconductors have a plasma frequency ω_J, waves below this frequency cannot propagate as they are screened out by the Josephson plasma [34]. This is in analogy with the plasma frequency in metals where low frequency radiation is screened by electrons [35]. Typical values for ω_J in layered superconductors are in the range of 0.1-0.5THz and are dependent on the critical current density of the material. This demonstrates what is an important property of layered superconductors, that they allow the propagation of THz frequency waves.

The Josephson effect also causes many unique, highly nonlinear phenomena. For example, when a Josephson junction is irradiated by microwaves, the current-voltage (IV) characteristics display a series of equally spaced plateaus of constant voltage called Shapiro steps [36, 37] at specific values of dc bias voltage. Since the separation of voltages is given by $\omega h/2e$ with ω the angular frequency of the microwave, the Shapiro steps are used as a voltage standard [38] or can be also employed to detect THz radiation [39]. In the opposite case, the Josephson effect provides a way to excite high frequency electromagnetic (EM) waves [22, 23, 40],

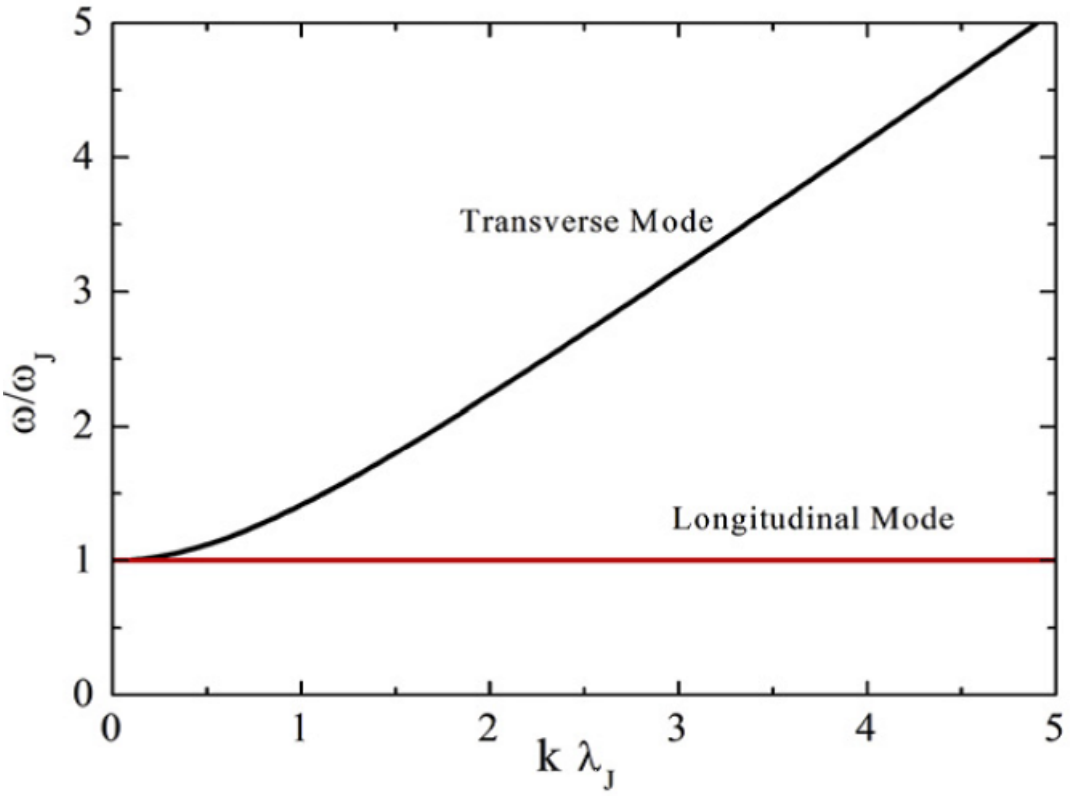

Figure 2.2: Plasma modes in a single Josephson junction. The longitudinal mode represents a fixed field at a frequency ω_J, transverse modes represent propagating Josephson plasma waves [28].

which was first confirmed in single junctions [18], and later in Josephson junction arrays [19].

Since the discovery of the cuprate high-T_c superconductors having layered structure [41], and the demonstration of the intrinsic Josephson effect in BSCCO [42], the effort to explore a strong EM source based on the nanoscale, built-in Josephson junctions has been accelerated [43, 44]. These so-called intrinsic Josephson junctions (IJJs) have obvious advantages superior to the artificial ones since the former are homogeneous at the atomic scale guaranteed by the high quality of

single crystals, and the superconducting gap is large, typically tens of MeV, which allows the frequency to cover the whole range of the terahertz range. An experimental challenge was to synchronize a stack of N IJJs to achieve a condition called super-radiance in which the radiation intensity increases proportional to N^2. This is compared with the weak increase of radiation from non-synchronized junctions which is proportional to N.

In 2007 an important experimental breakthrough was achieved when a substrate of a single crystal of the layered superconductor BSSCO was used to emit coherent THz super-radiance at up to 0.85THz and a power of around $0.5\mu W$ [45]. This was achieved by applying a c-axis bias voltage to a rectangular mesa mounted on top of the crystal with no applied magnetic field. The strong EM emission takes place at the bias voltage when the frequency determined by the ac Josephson relation equals the fundamental cavity mode, corresponding to a half-wavelength of the Josephson plasma in the mesa [45]. These experimental observations cannot be understood by the conventional understanding on Josephson phenomena developed mainly based on single Josephson junctions, since the known cavity modes associated with a finite external magnetic fields are clearly irrelevant and solitons, which can be excited in the absence of an external magnetic field and correspond to cavity modes, cannot be stacked uniformly in the c axis to achieve in-phase dynamics in all the junctions. It is also not clear why it is possible to synchronize the superconductivity phase differences of a total of about 600 junctions. Motivated by recent experiments [46, 47], theoretical investigations on the sine-Gordon equations for the IJJs have been carried out with special focus on the case of strong inductive coupling originating in the extremely small junction spacing of $s = 1.5nm$ as compared to the London penetration depth $\lambda_{ab} = 400nm$.

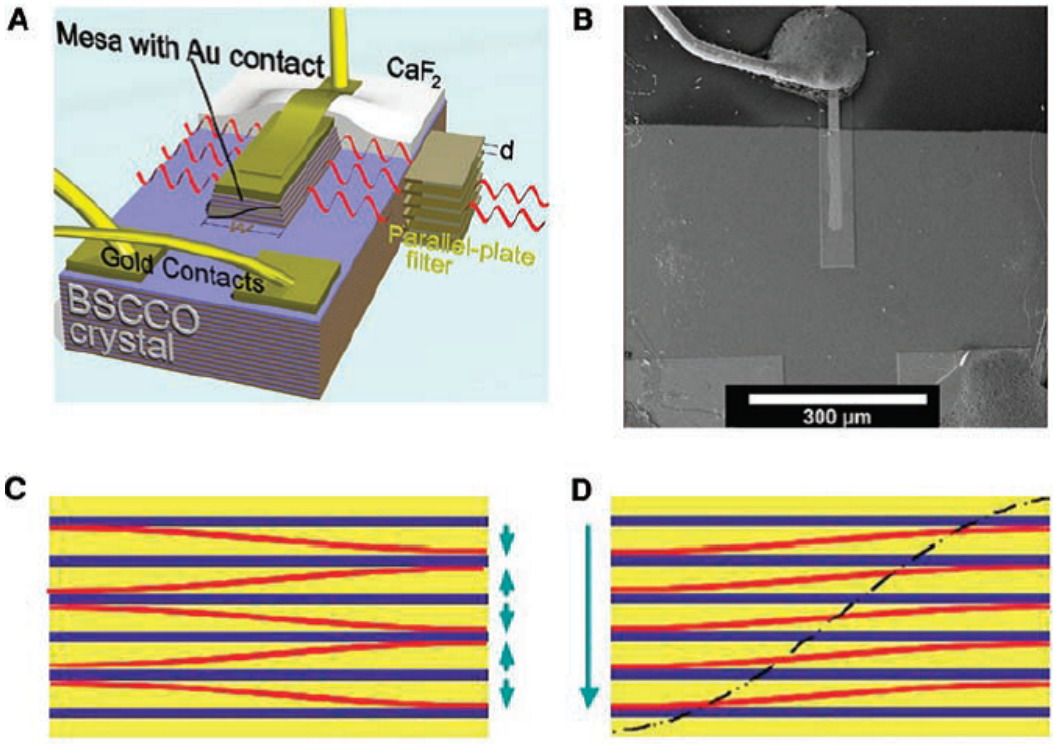

Figure 2.3: A) Schematic of BSSCO mesa for coherent emission of THz waves (red) B) SEM image of the mesa. Also shown are schematics of C) Out of phase mode and D) In phase mode, where the blue layers are CuO_2 and the yellow layers Bi-Sr-O. Red lines represent the electric field in each layer which for the in phase case sums up to a larger coherent wave (black dashed line). From [45], reprinted with permission from AAAS.

As well as the attempts to develop powerful THz emitters based on high-T_c layered superconductors, further research indicates that other THz devices can be fabricated based on these same materials. This opens up the possibility [19] of designing a well integrated set of THz devices using layered superconductors. A few of them are briefly outlined below.

Filters: Tuneable THz filters have been recently proposed [21, 27, 48] that use the Josephson vortex lattice as a tunable photonic crystal. Since the JV lattice is a

periodic array that scatters electromagnetic waves in the THz frequency range. It was shown that JV lattices can produce a controllable photonic band gap structure (THz photonic crystal) with easily tunable forbidden zones controlled by the in-plane magnetic field. The scattering of electromagnetic waves by JVs results in a strong magnetic-field dependence of the reflection and transparency.

Detectors: It was theoretically proven [49, 50] that surface Josephson plasma waves could propagate along the superconductor-vacuum interface with a frequency below the Josephson plasma frequency. This effect could be used for the development of frequency-sensitive bolometers using idea that an incident THz wave can resonantly excite these surface waves for certain angles of the incident wave with the sample surface (see Fig. 2.4). This results in a strong increase of the absorption of the THz wave in the sample and in a resonant peak of the sample resistance which can be measured. The position of this peak allows one to detect the frequency and direction of the incident THz wave.

Nonlinear THz devices: The effects of nonlinearity [51, 52] on the propagation of THz waves through layered superconductors has also been studied. It was analytically derived that (a) localized THz beam can propagate in layered superconductors for frequencies slightly below plasma frequency and (b) resonances related to standing waves can be abruptly destroyed above a certain energy threshold. These could be potentially useful for THz lenses, amplifiers, and continuous/pulse radiation converters.

Metamaterials: Materials which can be artificially fabricated to have physical properties not found in nature are known as metamaterials [53]. Recently proposals

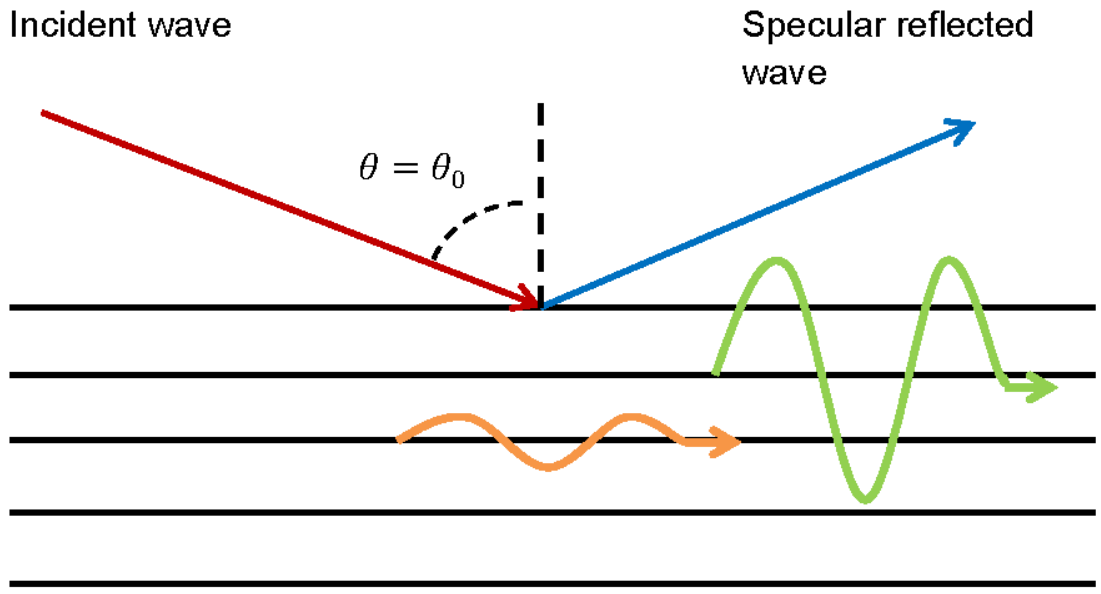

Figure 2.4: Schematic diagram of the excitation of surface JPWs (green wave) due to an incident THz wave (solid red line) at angle θ_0 to a layered superconductor. Also visible are the reflected wave (solid blue line) and damped wave (orange wave) within the superconductor [49]. Figure has been adapted from [49].

have been made [54, 55] for using layered superconductors as negative-refractive-index metamaterials which can offer sub wavelength resolution and aberration free imaging.

Chapter 3

Review : Photonic crystals

Photonic crystals [26, 56, 57] are composite materials in which the building blocks of the crystal unit cell are dielectric media. In photonic crystals there is a periodic spatial variation in the index of refraction, where the period is given by the size of the unit cell. The dimension of the photonic crystal is given by the number of independent spatial directions along which the variation of refractive index occurs. Example models for a one-, two- and three-dimensional photonic crystal have been depicted in Fig. 3.1.

An electromagnetic field incident upon a photonic crystal will be reflected periodically inside the medium at the boundaries between regions of different refractive index, the reflectance of each unit cell will increase when there is a higher contrast between the refractive indices of the constituent materials. When, for applied harmonic plane waves that propagate in a given direction, the wavelength and the crystal period along the propagation direction compare such that the back-reflected waves interfere constructively, the field will be strongly rejected from the crystal. In this case, the amplitude of the field within the crystal decays exponen-

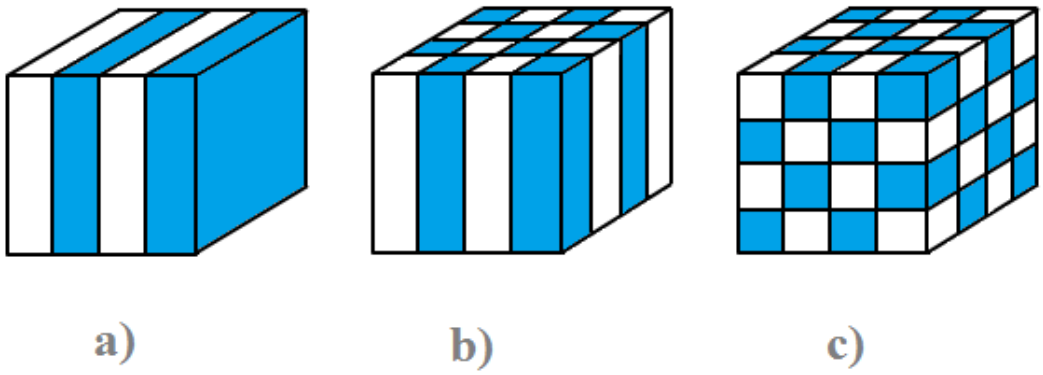

Figure 3.1: Photonic crystals with periodicity in a) One dimension b) Two dimensions and c) Three dimensions, where the building blocks (represented by white and blue) are materials with different dielectric properties. Figure adapted from [56].

tially with the distance to the boundary surface of the medium hence there will be no travelling wave of this field within the medium. The range of wavelengths or, equivalently, frequencies, for which no propagating wave solutions exist in the crystal is called the photonic band gap. If the photonic band gap extends to all possible propagation directions of the field, it is called a complete gap [26].

The opposite case of field rejection from the crystal occurs when the wavelength and crystal period along the propagation direction of the incident harmonic plane waves compare such that the back-reflected waves from unit cells interfere destructively. In that case, the field will be well-transmitted through the crystal. Depending on the wave-vector of an incoming electromagnetic wave, a photonic crystal can exhibit either high transmission and high reflection coefficients.

Fig. 3.2 depicts a sketch of the dispersion relation for electromagnetic harmonic plane waves in a uniform one-dimensional homogeneous medium and in a one-dimensional photonic crystal. The effects of the inhomogeneities of the medium

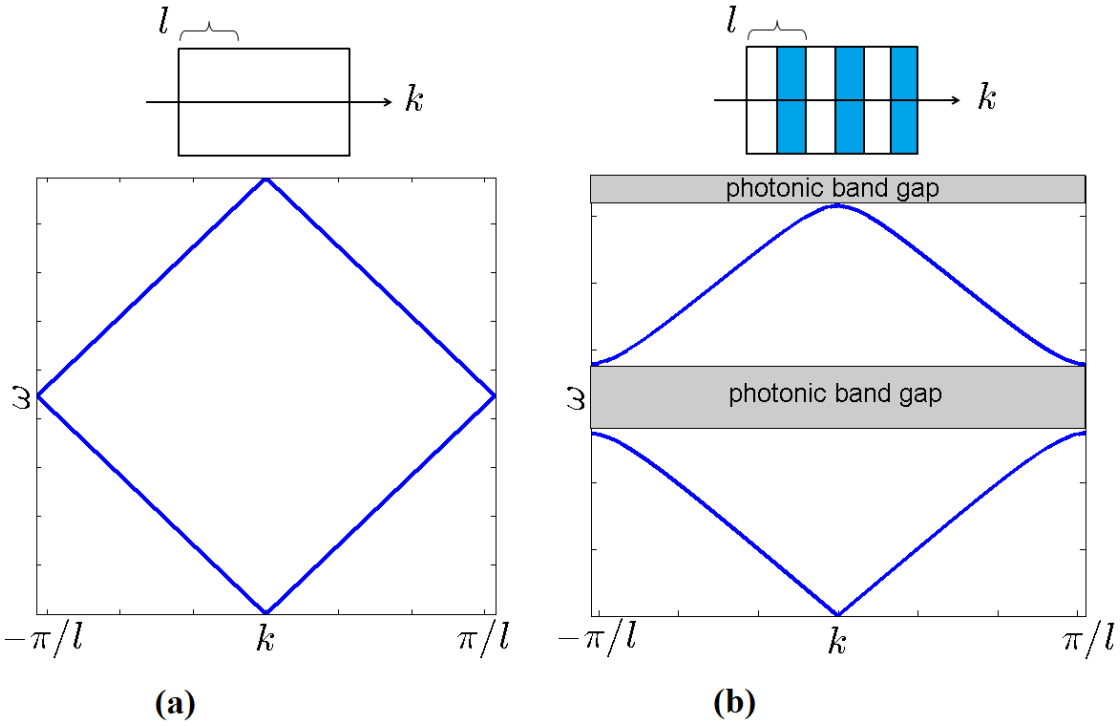

Figure 3.2: For materials with a constant permittivity ϵ the dispersion relation is continuous as shown in a) but as some periodicity in ϵ is introduced a band gap in the spectrum opens up as shown in b. Figure adapted from [56].

are seen in a splitting of the bands, the frequency solutions that correspond to the real wave number k, at the edges of the Brillouin zone at $k = \pm\pi/l$, resulting in the photonic band gap.

Due to such a band-gap structure of the light spectra, electromagnetic waves in photonic crystals have a strong analogy in the field of solid state physics. This similarity is given by electrons in interaction with a crystal lattice of atoms or molecules, where the crystal represents a periodic potential for the electrons. An electronic band gap results if the electrons are Bragg diffracted [58]. The charge configuration of the atoms or molecules and the structure of the crystal together determine the conduction properties of the medium. In photonic crystals, the index

of refraction of the material components and the crystal structure both determine the dispersion of light. The differences are that the electromagnetic wave has a polarization and satisfies the Maxwell equations whereas the electron wave is a scalar field that obeys Schrödinger's equation [59].

The main properties of 1D linear photonic crystals can be summarized as follows [60]:

- A photonic band gap characterized by an inhibited region in the transmission spectrum.
- Oscillations in the transmission spectrum whose number is given by the number of periods N of the structure.
- Dependence of the band gap on the building criteria of the crystal.
- Inside the structure the electric field is distributed in a selective way.

The unusual dispersion relation of electromagnetic waves in photonic crystals and in particular the possible presence of a photonic band gap render photonic crystals useful for manipulating the propagation of light. A legitimate question that could arise at this point is: why use such complex materials as photonic crystals and why not simply use the reflective properties of metals or the phenomenon of total internal reflection in dielectrics to control the propagation of light? Photonic crystals also offer added advantages over these other systems since they are much less dissipative than metal mirrors for the control of electromagnetic waves [61], so energy losses are reduced. Also, as compared to total internal reflection based

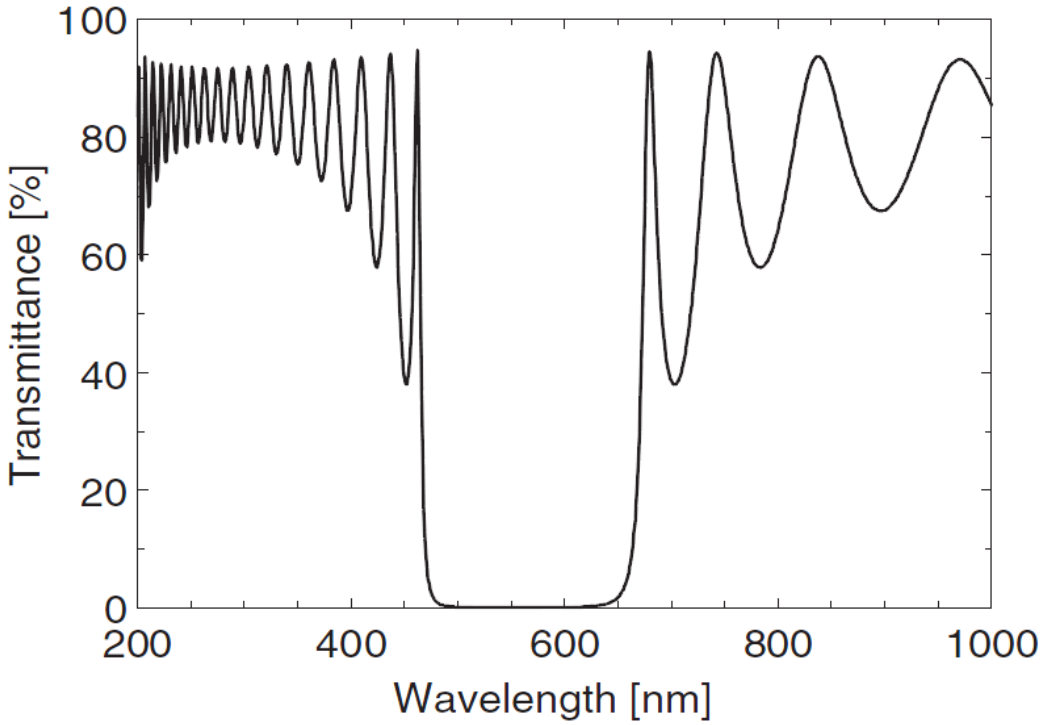

Figure 3.3: Typical transmittance against wavelength for a 1D photonic crystal, figure taken from [60].

waveguides such as for instance glass fibre cables, photonic crystals can manipulate the flow of light at a much smaller scale, namely that of the wavelength of the guided light itself [56].

3.1 Applications of photonic crystals

There are numerous applications of photonic crystals, the simplest being a filter for specific frequencies within the photonic band gap [62]. In 1994, Meade et al. [63] first proposed using them as waveguides. A waveguide is obtained from a photonic crystal by introducing a line of defects in it. Since the light cannot continue to

propagate in the perfect part of the crystal, it is forced to follow the defect route along which the periodicity is broken, even if this line has sharp bends. Although the light does not escape the photonic crystal waveguide at bends, part of the light undergoes backward reflection there, which also results in transmission loss. Much effort has been spent to reduce these back-reflection losses, for instance by rearranging the lattice near the bend [64], smoothing the bend and changing locally the width of the guide [65] and adding appropriate defects at the bend corners [66]. Confinement of the light to the waveguide that is independent of the shape of the guide can not be achieved in waveguides that are based on total internal reflection, where there exists a minimal bend radius below which the light escapes from the waveguide. For the guiding of for instance telecom waves (wavelength $1.5\mu m$ in vacuum [56]) in a glass fibre cable surrounded by air, the bend radius, which is the outer radius of the circularly bent cable, should be at least a few millimetres. As compared to a photonic crystal waveguide, which has extensions of the order of the wavelength of the guided light, this is a significant difference in size. This explains why photonic crystals can manipulate the flow of light at small scale.

If instead of a line of defects, only a single point defect is introduced in the photonic crystal, as Yablonovitch and Gmitter [67] first proposed in 1991, local electromagnetic modes can exist with frequencies that lie within the photonic band gap. Thus, photonic crystals can be used as microcavities, which are essential components of lasers and filters. For good performance, it is required that the cavity has a high quality factor, meaning a low energy loss per radiation cycle which implies having a well-defined frequency and a small mode amplitude, ensuring high coherence. Since these local electromagnetic modes can be confined with low loss, the quality factor of such a cavity can reach high values of over ten thousand [68]. Moreover,

the size of the cavity can be brought down to the order of the wavelength, which implies a rather small mode volume for the cavity. Various methods have been proposed to further increase the quality factor and decrease the mode volume, as for instance by adjusting the cavity geometry [69] and recycling the radiated field [70, 71]. The first working pulsed laser based on a photonic crystal microcavity was reported in 1999 by Lee et al. [72].

Further proposed photonic crystal applications are beam splitters [73], add/drop filters [74], switches [75, 76], waveguide branches [77], transistors [78], limiters [79, 80], modulators [81, 82], amplifiers [83, 84] and optical delay lines [85]. Many photonic crystal applications have been realized with good performance such as the drop filter [86], optical filter [74], polarization splitter [87], Y-splitter [88, 89] and Mach-Zehnder interferometer [90].

3.2 Nonlinear effects in photonic crystals

Nonlinear optics [91] is the study of phenomena that occur as a consequence of the modification of the optical properties of a material system by the presence of light. Typically, only laser light has sufficient intensity to modify the optical properties of a material. Shortly after the demonstration of the first working laser in 1960 came the discovery of second harmonic generation by Franken et al. in 1961 [92], which is considered the start of the field of nonlinear optics . Nonlinear optical phenomena are 'nonlinear' in the sense that they occur in the response of a material system to an applied electromagnetic field. Consequently the intensity of the light generated at the second harmonic frequency tends to increase as the square of the intensity of the applied laser light.

In order to describe more precisely what is meant by an optical nonlinearity we can consider how the polarization $\tilde{P}(t)$ of a material system (the dipole moment per unit volume), depends upon the strength of an applied electric field $\tilde{E}(t)$. In the case of conventional linear optics, the induced polarization depends linearly upon the electric field strength in a manner that can often be described in Gaussian units by

$$\tilde{P}(t) = \chi^{(1)}\tilde{E}(t), \tag{3.1}$$

where the constant of proportionality $\chi^{(1)}$ is known as the linear susceptibility. In nonlinear optics, the optical response can often be described by generalizing Eq. (3.1) by expressing the polarization as a power series in the field strength as in Eq. (3.2) which shows the series up to third order.

$$\tilde{P}(t) = \chi^{(1)}\tilde{E}(t) + \chi^{(2)}\tilde{E}^2(t) + \chi^{(3)}\tilde{E}^3(t) + ... \tag{3.2}$$

The quantities $\chi^{(2)}$ and $\chi^{(3)}$ respectively are known as the second and third order nonlinear optical susceptibilities.

The most common procedure for describing nonlinear optical phenomena is based on expressing the polarization $\tilde{P}(t)$ in terms of the applied electric field strength $\tilde{E}(t)$, as we have done in Eq. (3.2). The reason why the polarization plays a key role in the description of nonlinear optical phenomena is that a time-varying polarization can act as the source of new components of the electromagnetic field. For example, the wave equation in nonlinear optical media often has the form given in Eq. (3.3).

$$\nabla^2 E - \frac{n^2}{c^2}\frac{\partial^2 E}{\partial t^2} = \frac{4\pi}{c^2}\frac{\partial^2 \tilde{P}^{NL}}{\partial t^2}, \tag{3.3}$$

where n is the usual linear refractive index and c is the speed of light in a vacuum. We can interpret Eq. (3.3) as a nonlinear wave equation in which the polarization $\tilde{P}^{NL}$ associated with the nonlinear response drives the electric field $\tilde{E}$.

As an example of a nonlinear optical interaction, we can consider the process of second harmonic generation. This is appropriate since second harmonic generation will be analyzed in Chapter 4 for the JV photonic crystal. Here we can consider a laser beam of frequency ω whose electric field strength is represented by Eq. (3.4), incident upon a crystal for which the second-order susceptibility $\chi^{(2)}$ is nonzero.

$$\tilde{E}^{(1)}(t) = E^{(1)}e^{-i\omega t} + cc. \tag{3.4}$$

$E^{(1)}$ here is the linear electric field amplitude incident upon the crystal. The nonlinear polarization that is created in such a crystal is given according to Eq. (3.2) as $\tilde{P}^{(2)} = \chi^{(2)}\tilde{E^{(1)}}(t)^2$ which can also be written in the form of Eq. (3.5).

$$\tilde{P}^{(2)} = 2\chi^{(2)}E^{(1)}E^{(1)^*} + (\chi^{(2)}{E^{(1)}}^2 e^{-2\omega t} + cc.) \tag{3.5}$$

The first term in Eq. (3.5) for the second order polarization is a contribution that has zero frequency component, it should be noted that this term does not generate electromagnetic radiation since its second time derivative is zero. It creates a static electric field within the nonlinear material, a process called optical rectification. The second term has a contribution at frequency 2ω. According to the nonlinear wave equation Eq. (3.5), this latter contribution can lead to the generation of

radiation at the second harmonic frequency. Other nonlinear processes include higher harmonic generation, optical parametric oscillation and sum and difference generation in response to two frequency inputs to the nonlinear material [91].

Since this thesis considers Josephson-vortex-THz photonic crystals taking into account nonlinear properties of the Josephson media, it is natural here to review properties of more usual nonlinear optical photonic crystals based on the review [60] by Bertolotti. This discusses the nonlinear properties of photonic crystals in higher dimensions, and introduces a multiscale approach to analyzing the field amplitudes within them. The first section of the review describes a parametric optical process in a nonlinear photonic crystal, the basic approach used is to use a plane wave solution (3.6) to the nonlinear wave equation of monochromatic form.

$$E(x,t) = E(x)E_L(x,t) \tag{3.6}$$

Where E_L is the plane wave solution to the linear part of the wave equation. Substituting (3.6) in a nonlinear wave equation a set of 3 coupled nonlinear equations can be derived for the electric field amplitudes of pump, signal and idler waves for the case of a parametric oscillator, eliminating the time varying exponential make the expressions time independent. The equations also involve the second order susceptibility $\chi^{(2)}$, as part of the nonlinear term on the right hand side and can be used to describe any parametric optical process in a second order nonlinear material. Here the mathematical procedure will only be described qualitatively.

Assuming that the nonlinearity of the photonic crystal is weak, we can consider the nonlinearity to only affect the linear solutions over a large length scale, greater than the period d of the structure. This makes it possible to apply a multiscale

expansion, separating the solution into independent variables $x_\alpha = \lambda^\alpha x$, with λ the perturbing parameter and α an integer value.

Separating the electric field into a fast and slow varying function of position and assuming weak nonlinearity allows a perturbative solution of the form (3.7) to be found for the electric field inside a nonlinear crystal.

$$E(x_0, x_1) = A(x_1)E_L(x_0) \tag{3.7}$$

Here A is a slowly varying nonlinear amplitude with a characteristic length scale of variation x_1 and E_L the solution of the linear wave equation with the scale of variation $x_0 \ll x_1$. Substituting (3.7) to the coupled system of equations and collecting terms proportional to λ gives a first order expression for the electric field. The separation of the solution into linear and nonlinear parts with different length scales will be used in Section 4.5 to develop an analytical approximation for the second harmonic in the JV photonic crystal.

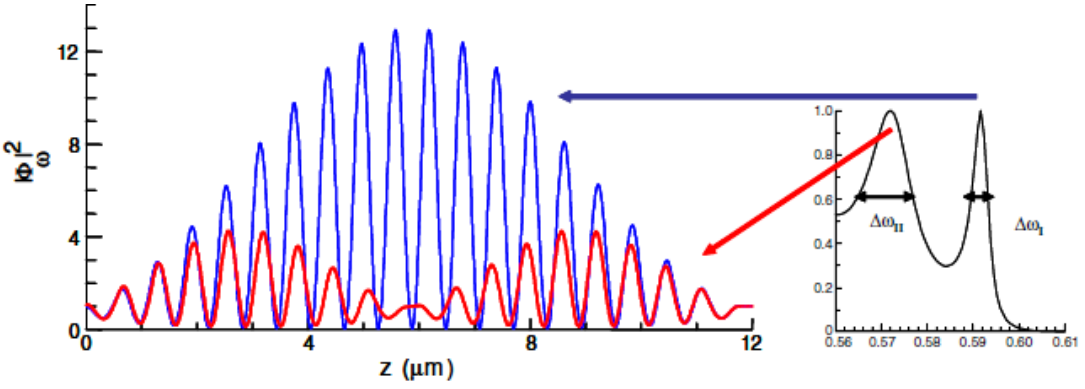

Figure 3.4: Localization of the electric field modulus inside a nonlinear 1D photonic crystal, plotted for the two transmission peaks in the spectrum shown in red and blue [60].

Fig. 3.4 shows the electric field distribution calculated within a crystal for the two

transmission peaks in the spectrum in this case. The two length scales of variation can be clearly seen. The nonlinearity affects the wave amplitude of the linear solution only on a large distance scale. Nonlinearity allows optical photonic crystals to display second harmonic generation, giving a signal at double the fundamental frequency ω. This is a possible way to increase the frequencies emitted by current THz devices.

In addition to the multiscale mathematical method mentioned above in this section, it should be mentioned that there are several useful properties of nonlinear waves in photonic crystals. Ostrovskaya and Kivshar [93] have shown how nonlinear periodic structures can support both optical waves and matter waves (as described by their de Broglie wavelength [94]). Parallels are drawn between the two for the case of Bose-einstein condensates in optical lattices and nonlinear photonic crystal structures. This indicates that nonlinear waves can behave like particles and can be described by a nonlinear Schrödinger equation. Nonlinearity in materials allows for localized modes to appear in the band gap of the spectrum, also known as gap solitons [95]. A soliton is by definition a localized solution to the nonlinear dispersive wave equation that remains invariant upon propagation, in Section 2.1.2 JVs are described mathematically by their soliton solutions. In fully integrable systems, these waves remain intact after collision events and in essence they behave as particle-like entities. Gap solitons occur in materials with third order or Kerr nonlinearity (which is similar to the nonlinearity in Josephson media) and open up new applications of photonic crystals for optical signal processing and switching. Also for generating tunable band gap structures and waveguides.

3.3 The Josephson-vortex THz photonic crystal

There are two main types of layered superconductors which have interesting physical properties, including highly anisotropic (Bi-, Tl- and Hg-based) high-T_c superconductors as well as artificial multilayered heterostructures such as ($Nb - Al - AlO_x - Nb$). These layered structures consist of superconducting and insulating layers which are parallel to the crystallographic ab plane, and can be described as stacks of Josephson junctions (SJJ) [33]. When an external magnetic field H_{ab} is applied parallel to the ab plane, Josephson vortices (JVs) can penetrate the sample and form a triangular lattice [96]. Josephson vortices have a very weak interaction with lattice crystal defects and consequently can form a near perfect lattice at low temperatures. These materials offer the possibility to design a THz photonic crystal which can be tuneable by an applied in-plane magnetic field.

The JV lattice is a periodic array that scatters electromagnetic waves in the THz-frequency range. It has already been shown [21, 27, 48] that JV lattices can produce a theoretical photonic band-gap structure (THz photonic crystal) with easily tuneable forbidden zones controlled by the in-plane magnetic field. The scattering of electromagnetic waves by JVs results in a strong magnetic-field dependence of the reflection and transparency. Fully transparent or fully reflected frequency windows can be conveniently tuned by the in-plane magnetic field. These proposals are potentially useful for controllable THz filters.

By studying the influence of a fixed JV lattice on the propagation of THz electromagnetic waves, it was found [27] that the interaction of the propagating wave and JV lattice results in forbidden gaps in the frequency spectrum (i.e., a THz photonic crystal) conveniently tuneable by the applied magnetic field H_{ab}. Moreover,

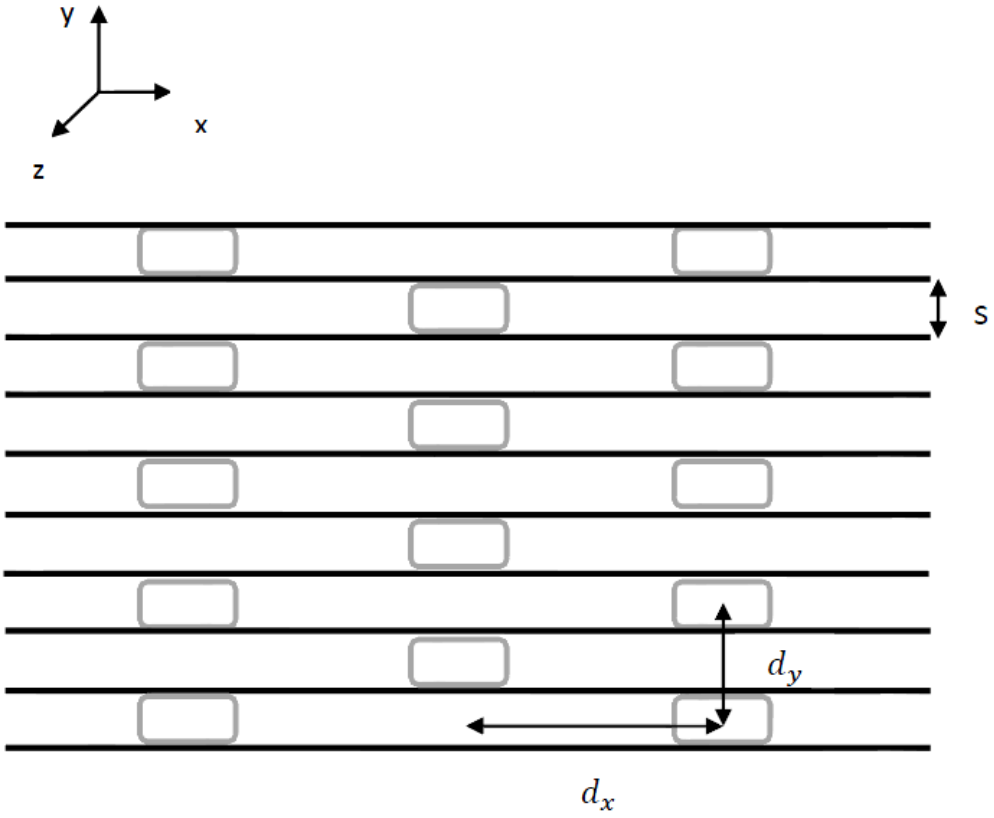

Figure 3.5: Structure of the JV lattice in layered superconductors where black horizontal lines represent thin superconducting layers separated by a distance s and grey rectangles represent the triangular lattice of JVs between the layers, separated by distances d_x and d_y along the x and y axes respectively. Taken from [102], with kind permission of the European Physical Journal (EPJ).

by changing H_{ab} one can easily change, by an order of magnitude, both the transmission, T, and reflection, $R = 1 - T$, coefficients of the electromagnetic waves. Thus, the layered superconducting sample can operate as a THz-frequency filter tuned by the applied magnetic field H_{ab}.

3.3.1 Model for linear JV photonic crystal

What follows is a brief description of the model for analyzing the linear properties of the JV photonic crystal [27], this will be the basis for investigating the nonlinear properties in later chapters. Considering a high-T_c superconductor with superconducting layers in the xz coordinate plane, which coincides with crystallographic ab plane with the coordinate y axis (along the c axis) across the layers. In this case the superconducting layers are much thinner than their separation s along the y axis, which allows the spatial variation of electromagnetic fields to be ignored within the superconducting layers.

The high anisotropy of the system is quantified by the anisotropy coefficient $\gamma = \lambda_c/\lambda_{ab}$ given by the the ratio of the out-of-plane penetration depth λ_c and the in-plane penetration depth λ_{ab}. The in-plane field H_{ab} is applied in the xz plane, with the Josephson vortices parallel to the z axis. The distance d_x between JVs in the lattice along the x direction is much larger than along the y direction d_y, so the lattice consists of densely packed rows of vortices along the y-axis. According to the anisotropic London model [97] for layered superconductors, the ratio $d_x/d_y =$ and is independent of the applied magnetic field and can also be described by $d_x/d_y = \gamma$. The typical value of γ for a single crystal of $Bi2212$ is 300-600 [27].

We consider waves propagating along the superconducting layers so that their oscillating magnetic field is in the same axis as the Josephson vortices

$$H(x, y, t) = \hat{z} H_0(x) \exp(iqy - i\omega t),$$

where $\hat{z}$ is the unit vector along the z-axis and q the y-axis wavevector (perpendicular to the superconducting layers). The gauge-invariant phase difference φ_n

in a layered superconductor can be described by the set of coupled sine-Gordon equations [25]

$$\left(1-\frac{\lambda_{ab}^2}{s^2}\partial_n^2\right)\left(\frac{\partial^2\varphi^{(n)}}{\partial t^2}+\omega_r\frac{\partial\varphi^{(n)}}{\partial t}+\omega_J^2\sin\varphi^{(n)}\right)-\frac{c^2}{\epsilon}\frac{\partial^2\varphi^{(n)}}{\partial x^2}=0. \tag{3.8}$$

Here n is an integer that labels each superconducting layer of the system along the y-axis, ω_J is the plasma frequency, ∂_n^2 is an operator responsible for coupling between the layers and is given by $\partial_n^2 f_n = f_{n-1} + f_{n+1} - 2f_n$ when acting on a function f_n.

The equations are similar in form to the sine-Gordon equation for a single Josephson junction as derived in Section 2.1.1, however the inductive coupling of junctions through the operator $(1 - \lambda_{ab}^2/s^2\partial_n^2)$ has to be considered. This takes into account the coupling of the magnetic field between superconducting layers and is the strongest coupling present in layered superconductors. The capacitive coupling constant in layered superconductors can been shown to be negligible [98] and hence can be ignored.

$\omega_r = 4\pi\sigma_\perp/\epsilon$ is the damping frequency which is proportional to the transverse conductivity $\sigma_\perp$, for low enough temperatures this can be reduced to a negligibly small value where $\omega_r/\omega_J \ll 1$ [27]. Eq. (3.8) was derived to find the radiation given off when a triangular vortex lattice was accelerated by a current perpendicular to the superconducting layers.

Since φ can be represented as a superposition of the two solutions mentioned in Section 2.1.1, φ_0 for Josephson vortices and φ_1 for Josephson plasma waves. It can be assumed that $|\varphi_1(x,y,t)| \ll |\varphi_0^{(n)}(x,t)|$, so a first order Taylor expansion $\sin\varphi \approx \sin\varphi_0 + (\cos\varphi_0)\varphi_1$ can be substituted in Eq. (3.8).

The soliton solution for the phase $\varphi_0(x)$ due to a single Josephson vortex centred at $x = 0$ is given by Eq. (3.9) [99]

$$\varphi_0 = \pi + 2\tan^{-1}(x/l_0) \tag{3.9}$$

where l_0 is the vortex radius. It's useful here to define a normalised magnetic field $h_{ab} = H_{ab}/H_1$, where $H_1 = 2\phi_0/\gamma s^2$, the condition $h_{ab} \ll 1$ must apply for the vortex solutions to be valid.

The period d_x of the vortex lattice along the x-axis can be calculated using Eq. (3.10), which explicitly shows that the lattice spacing is inversely proportional to the applied magnetic field.

$$d_x = \frac{2l_0}{\sqrt{h_{ab}}} \tag{3.10}$$

Since in equation 3.8 the vortex 'potential term' is given by $\langle\cos\varphi_0\rangle$ we should take the cosine of Eq. (3.9) which gives us

$$\cos\varphi_0(x) = -\frac{l_0^2 - x^2}{l_0^2 + x^2}. \tag{3.11}$$

Eq. (3.11) is plotted in Fig. 3.6, showing that the 'potential' decays quickly away from a Josephson vortex. Due to the high anisotropy of the vortex lattice given by γ, an important simplification can be made at this point. The close packing of vortices along the y-axis in this model means that radiation of THz frequencies cannot probe the structure of individual vortices in this direction and the problem can be reduced to a one dimensional photonic crystal. This approximation is called the continuous 1D limit and has the consequence that the function $\cos\varphi_0$ can be

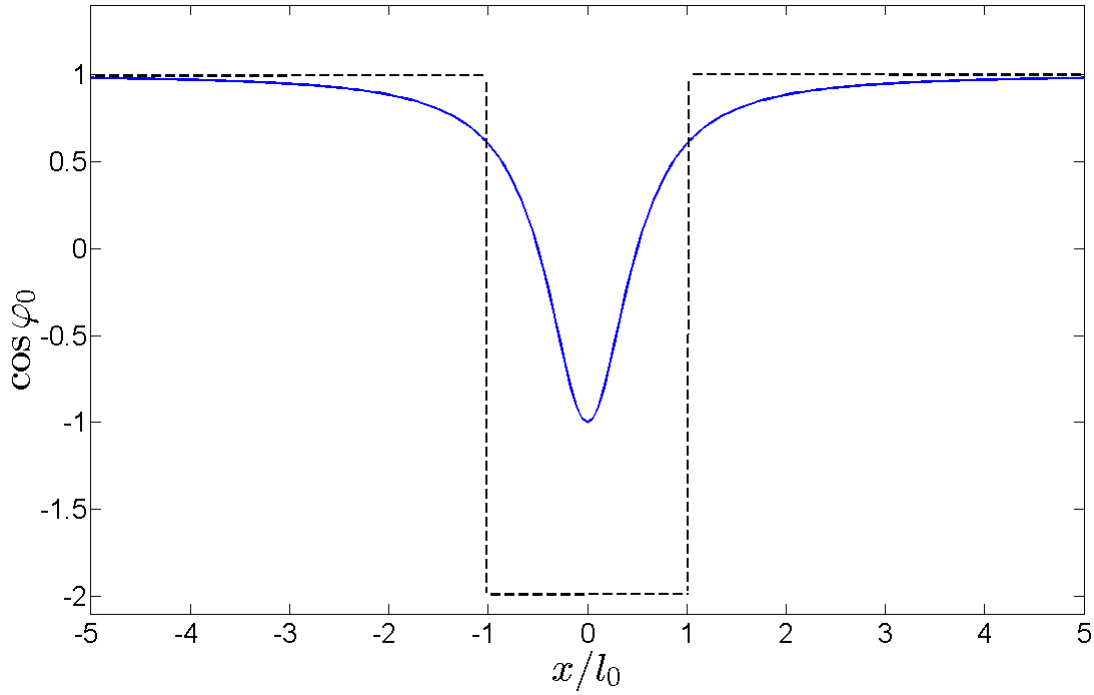

Figure 3.6: Plot of $\cos\varphi_0$(blue) for a single Josephson vortex located at $x = 0$ [27].The step function approximation (dashed black line) can be used to calculate the linear spectrum.

represented by the average over the layers in the y direction, given by Eq. (3.12).

$$\langle \cos\varphi_0^{(n)} \rangle = \frac{1}{2N} \sum_{l=n-N}^{n+N} \cos\varphi_0^{(l)} \tag{3.12}$$

where n labels each superconducting layer along the y-axis and N is the number of vortices summed either side of this layer.

Since the decay of $\langle \cos\varphi_0 \rangle$ away from a vortex is so sudden the function can be approximately represented by a step function that has the same value for the integral over the unit cell of the vortex lattice. To calculate the linear spectrum for the JV photonic crystal, we can use this step function approximation for the

vortex potential to define constant values for $\langle \cos \varphi_0 \rangle$ in two separate regions of the unit cell, plotted in Fig. 3.6. Region 1 is the space between vortex cores in the x-direction and region 2 corresponds to a vortex core.

Using Bloch wave solutions of the form $\psi(x) = u(x,k) \exp(ikx)$ to the linear Sine-Gordon equation, an equation for the periodic function u can be found. Applying periodic boundary conditions with the same periodicity L of the vortex lattice, the linear spectrum for Josephson plasma waves in the Josephson-vortex photonic crystal can be derived. The expression for this is given in Eq. (3.13) and plotted in Fig. 3.7 [27]. Since the spectrum for the second harmonic will be derived by the same basic method in Chapter 4 and this represents original work in this thesis, the detail of the derivation will be shown there.

$$\cos(\alpha b)\cos(\beta) - \frac{\alpha^2 + \beta^2}{2\alpha\beta} = \cos[k(b+1)] \tag{3.13}$$

α and β represent effective wavevectors in region 1 and region 2 respectively and b is the width of region 1 along the x-axis, or the distance between vortices. Fig. 3.7 shows us that the spectrum of Josephson plasma waves in the presence of JVs has a photonic band gap structure with a THz band gap tunable by the applied magnetic field h_{ab}. From this the reflection and transmission coefficients can be found by the transfer matrix method.

It should also be noted that the JV lattice can be driven by applying a c-axis current perpendicular to the superconducting layers. In this case the spectrum has been predicted to display a Doppler effect which could be used to further tune the reflectivity of the JV photonic crystal.

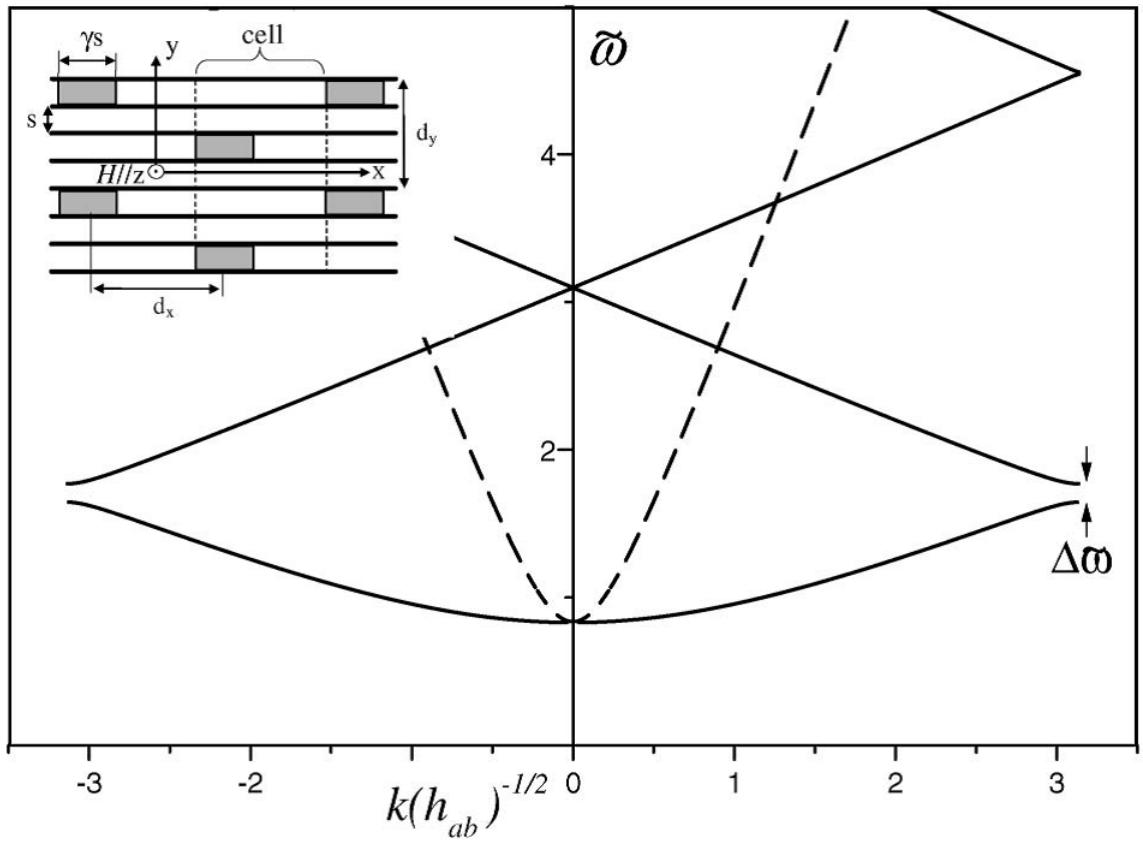

Figure 3.7: Linear band gap structure for EM waves in the JV photonic crystal. Plotting dimensionless $\tilde{\omega}$ against $k(h_{ab})^{-1/2}$ for $qs = 0.3\pi$ (solid line) and $qs = 0.05\pi$ (dashed line). Dimensionless magnetic field $h_{ab} = 0.2$, $s = 15\mathring{A}$, $\lambda_{ab} = 2000\mathring{A}$ and $\gamma = 600$. Reprinted figure with permission from [21]. Copyright (2005) by the American Physical Society.

Chapter 4

Second harmonic generation

This thesis will now move on to investigate the effects of the nonlinearity of the Josephson-vortex THz photonic crystal. Specifically the focus will be on higher harmonic generation in the next two chapters, and then the nonlinear mixing of THz waves in Chapter 6.

It is well known in nonlinear optics that materials that display nonlinear behaviour, i.e. a nonlinear response to an applied electromagnetic field, can exhibit unusual optical properties. These nonlinear effects are displayed for high amplitude fields. As shown in Section 3.2, a material with second order nonlinear susceptibility $\chi^{(2)}$ can produce a second harmonic at a frequency 2ω in response to an input at frequency ω. The second harmonic generation process is illustrated schematically in Fig. 4.1.

The nonlinearity of the JV THz photonic crystal occurs due to the nonlinear Josephson coupling between the superconducting layers, this gives the possibility of second harmonic generation in the crystal. By extending the approach outlined in Section 3.3.1, it is hoped that an analysis can be made of the second harmonic

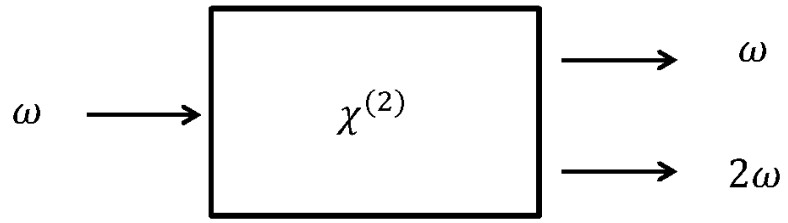

Figure 4.1: Schematic diagram for second harmonic generation in a nonlinear material with non-zero second order susceptibility $\chi^{(2)}$ represented by the rectangular box. The left arrow represents an input at frequency ω and the two right arrows represent the waves generated from the crystal at ω (first harmonic) and 2ω (second harmonic). Figure adapted from [91].

in the JV photonic crystal.

4.1 Deriving the second harmonic equations

The spatial and temporal variance of the inter-layer gauge-invariant phase difference φ of the order parameter for layered superconductors is once again given by the coupled sine-Gordon equations, which can be written in the continuous limit approximation as Eq. (6.1) [101].

$$\left[1 - \lambda_{ab}^2 \frac{\partial^2}{\partial y^2}\right] \left(\frac{1}{\omega_J^2} \frac{\partial^2 \varphi}{\partial t^2} + \sin\varphi\right) - \lambda_c^2 \frac{\partial^2 \varphi}{\partial x^2} = 0, \tag{4.1}$$

Here Eq. (3.8) from the previous chapter has been divided through by ω_J and simplified using the expression $\lambda_c = c^2/\sqrt{\epsilon}$. Since φ_1 varies slowly on the scale of the distance s between layers we can replace the discrete differential operator from Eq. (3.8) with a continuous derivative w.r.t. y.

Note that the damping term has been neglected in Eq. (6.1), which is valid for samples thinner than the skin depth (about 0.3 mm for standard high-T_c superconductors). For samples thicker than this, the dissipation of Josephson plasma waves should be taken into account. Since the distance between vortices however is much smaller than the characteristic scale of damping for magnetic fields ($H \lessapprox \Phi_0/\gamma s^2$), this damping can be safely neglected. So for low enough temperatures, Josephson plasma waves scatter many times before they significantly decay in amplitude.

Using the same procedure of averaging the phase contribution from vortices along the y-axis as used in Section 3.3.1 we can also take the Taylor expansion $\sin\varphi \approx \sin\varphi_0 + (\cos\varphi_0)\varphi_1 - (\sin\varphi_0\varphi_1^2/2$. This time we are including the second order term which allows Eq. (4.2) to be derived, taking in to account the nonlinear current contribution.

$$\left[1 - \lambda_{ab}^2 \frac{\partial^2}{\partial y^2}\right]\left(\frac{1}{\omega_J^2}\frac{\partial^2\varphi_1}{\partial t^2} + \langle\cos\varphi_0\rangle\varphi_1 + \frac{\langle\sin\varphi_0\rangle}{2}\varphi_1^2\right) - \lambda_c^2\frac{\partial^2\varphi_1}{\partial x^2} = 0. \tag{4.2}$$

Here the functions $\langle\cos\varphi_0\rangle$ and $\langle\sin\varphi_0\rangle$ represent the average values of these functions in the y direction. It's important to not here that without the presence of vortices, there would be no second harmonic generation in layered superconductors since the nonlinear expansion of the Josephson current would contain only odd powers of φ_1.

We can insert a solution (4.3) to Eq. (4.2) for the first and second harmonic amplitudes respectively,

$$\varphi_1 = \psi_1\cos(\omega t - qy) + \psi_2\cos(2\omega t - 2qy) \tag{4.3}$$

where ψ_1 is the amplitude of the first harmonic and ψ_2 the amplitude of the second harmonic. This gives us two coupled nonlinear equations Eq. (4.4) and Eq. (4.5) for ψ_1 and ψ_2 respectively when all higher harmonics from this substitution are ignored.

$$(\langle\cos\varphi_0\rangle - \tilde{\omega}^2)\psi_1 - \frac{\lambda_c^2}{(1+\lambda_{ab}^2 q^2)}\psi_1'' = \frac{\langle\sin\varphi_0\rangle}{2}\psi_1\psi_2 \tag{4.4}$$

$$(\langle\cos\varphi_0\rangle - 4\tilde{\omega}^2)\psi_2 - \frac{\lambda_c^2}{(1+4\lambda_{ab}^2 q^2)}\psi_2'' = \frac{\langle\sin\varphi_0\rangle}{4}\psi_1^2 \tag{4.5}$$

We also introduce the dimensionless frequency $\tilde{\omega} = \omega/\omega_J$. The coupling of these two equations is significant since it allows for feedback between the two harmonics. It's interesting to note that these equations are in the form of a nonlinear Schrödinger type equation for THz waves in the JV photonic crystal, where $\langle\cos\varphi_0\rangle$ represents the potential due to vortices. The second term (containing $\psi_{1,2}''$) can be thought to represent the effective mass of THz waves in the JV photonic crystal.

4.2 Harmonic interaction potential

Eq. (4.4) and Eq. (4.5) contain a potential $\langle\sin\varphi_0\rangle$ as part of the nonlinear term not seen in the linear calculations, this can be called the 'vortex interaction potential'. An expression for $\langle\sin\varphi_0\rangle$ can be derived in a similar way to $\langle\cos\varphi_0\rangle$ as discussed in Section 3.3.1. For a single Josephson vortex the harmonic interaction potential can be given by Eq. (4.6), and is plotted in Fig. 4.2. The value of $\sin\varphi_0$ also decays away from a vortex but not as quickly as $\cos\varphi_0$.

$$\sin\varphi_0(x) = -\frac{2l_0 x}{l_0^2 + x^2} \tag{4.6}$$

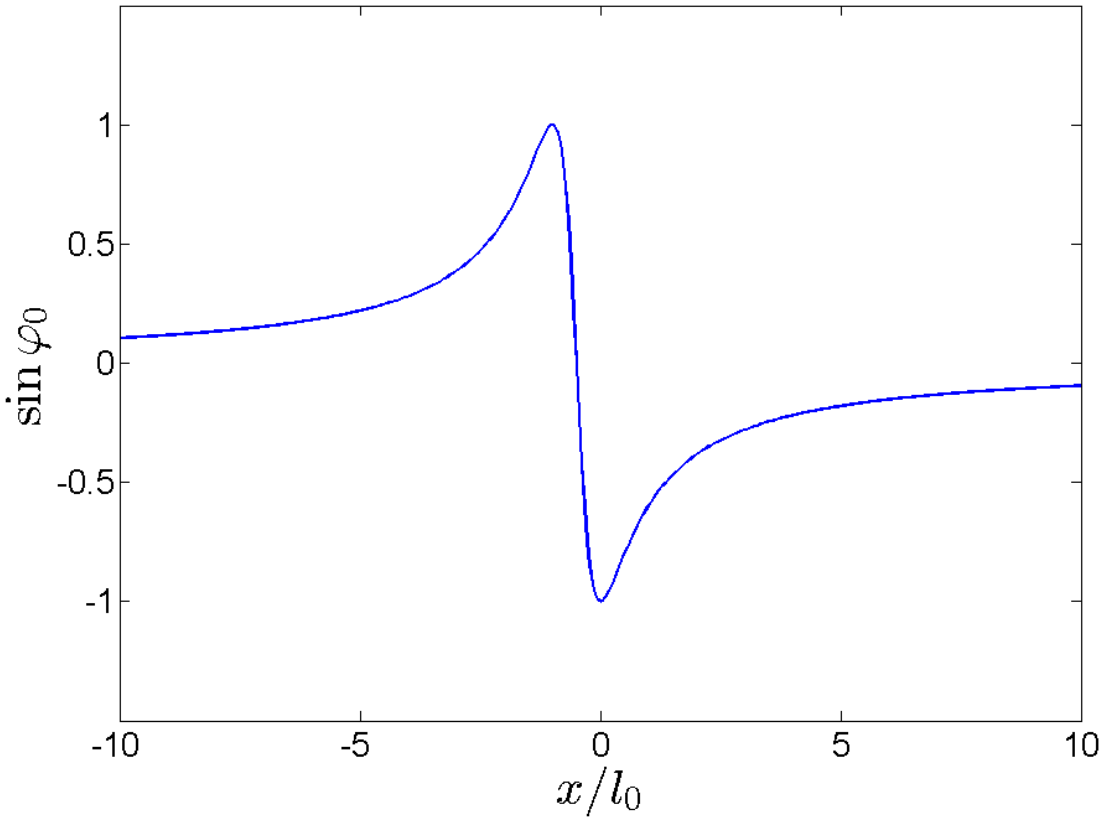

Figure 4.2: Plot of $\sin\varphi_0$ based on Eq. (4.6) for a single Josephson vortex located at $x = 0$. Distance x has been normalised by the vortex radius l_0.

To model $\langle\cos\varphi_0\rangle$ and $\langle\sin\varphi_0\rangle$ over the entire vortex lattice these functions need to be made periodic. Although it would be possible to sum the contribution due to all vortices in the lattice at any given coordinate x this is unnecessary since the contribution due to even neighbouring vortices is small for the magnetic field strengths that will be considered here. It has been taken as sufficient here to simply consider the $\langle\sin\varphi_0\rangle$ contribution from the nearest vortex only.

The periodic functions are given in Eq. (4.7) and Eq. (4.8).

$$\langle \cos \varphi_0 \rangle = -\frac{s}{dy} \sum_n \frac{(x - \frac{2n+1}{2} d_x)^2 - l_0^2}{(x - \frac{2n+1}{2} d_x)^2 + l_0^2} \tag{4.7}$$

$$\langle \sin \varphi_0 \rangle = -\frac{s}{dy} \sum_n \frac{2l_0(x - \frac{2n+1}{2} d_x)}{(x - \frac{2n+1}{2} d_x)^2 + l_0^2} \tag{4.8}$$

Here n is an integer labelling each unit cell of the vortex lattice, it assures that the potential considered for both $\langle \cos \varphi_0 \rangle$ and $\langle \sin \varphi_0 \rangle$ is only considering the closest vortex at each point. We can refer to this as the nearest vortex approximation. At the boundary between vortices in the x direction the potential function switches from the n^{th} vortex to the $(n+1)^{th}$ vortex. As shown in Fig. 4.4, this introduces a discontinuity in $\langle \sin \varphi_0 \rangle$. The factor s/d_y has the effect of averaging in the y direction based on the number of vortices per layer.

Fig. 4.3 shows that it's fairly straight forward to make $\langle \cos \varphi_0 \rangle$ periodic and continuous over the entire vortex lattice by just taking into account the nearest vortex approximation at each point.

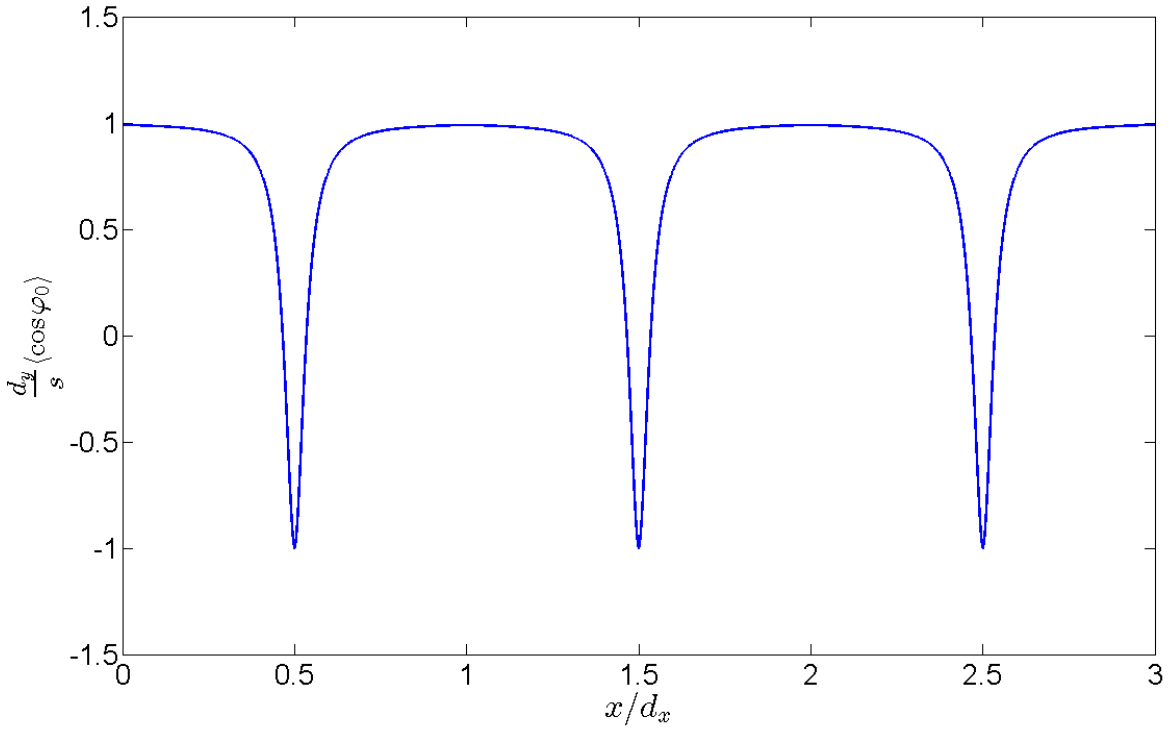

Figure 4.3: Plot of the value of $\langle\cos\varphi_0\rangle$ to a series of 3 unit cells of the vortex lattice based on Eq. (4.7), where only the contribution of the nearest vortex is taken into account. $h_{ab} = 0.005$.

Fig. 4.4 however shows that $\langle\sin\varphi_0\rangle$ is discontinuous at the midpoint between vortices when only taking into account the nearest vortex. Taking a sum over more nearest neighbours, first a sum over 3 vortices, (i.e. the n^{th} vortex plus two nearest neighbours) and then a sum over 5 vortices (n^{th} plus 4 nearest neighbours) allows this discontinuity to be reduced. The effect of this approximation on the final results will be discussed in Section 4.4.

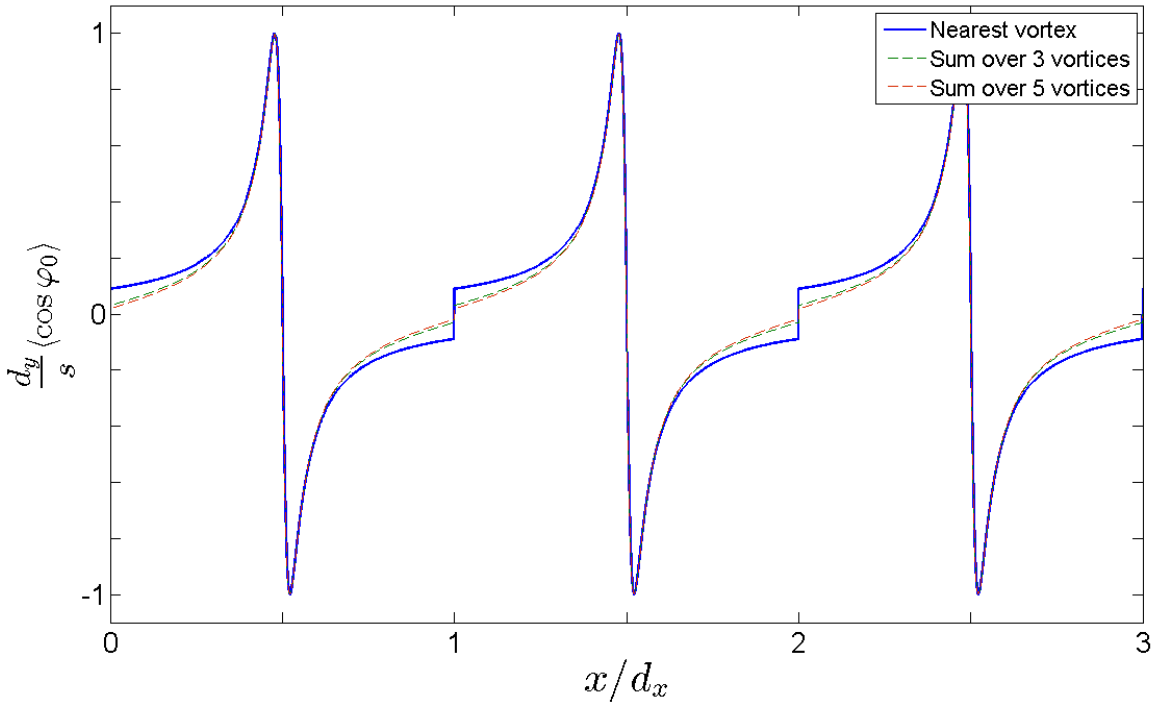

Figure 4.4: Plot of the the value of $\langle \sin \varphi_0 \rangle$ due to a series of 3 unit cells of the vortex lattice based on Eq. (4.8), taking into account first the contribution of the nearest vortex (solid blue line), then using a sum over the 3 nearest vortices (dashed green line) and a sum over the 5 nearest vortices (dashed red line). $h_{ab} = 0.005$.

4.3 Second harmonic linear spectrum

The linear spectrum for the second harmonic can be calculated in the same way as the first harmonic that was briefly described in Section 3.3, using Bloch wave solutions to the linear part of the second harmonic equation given by Eq. (4.9). Here the nonlinear term on the right hand side has been ignored.

$$(\langle \cos \varphi_0 \rangle - 4\tilde{\omega}^2)\psi_{L2} - \frac{\gamma^2}{4q^2}\psi''_{L2} = 0 \tag{4.9}$$

Here ψ_{L2} is the linear solution to Eq. (4.5). We can substitute a Bloch wave solution of the form $\psi_{L2} = v(x,k)e^{ikx}$ into Eq. (4.9) to give a quadratic expression

(4.10) for the periodic function v.

$$v^{''} + 2ikv^{'} + (\frac{4q^2}{\gamma^2}(4\tilde{\omega^2} - \langle\cos\varphi_0\rangle) - k^2)v = 0 \tag{4.10}$$

We can write the linear solutions for v in terms of right travelling and left travelling waves with amplitudes D_+ and D_- respectively, each with wavevectors $k_\pm$ given by Eq. (4.11).

$$v = D_+ e^{ik_+ x} + D_- e^{ik_- x}$$

$$k_\pm = -k \pm \frac{2q}{\gamma}\sqrt{4\tilde{\omega^2} - \langle\cos\varphi_0\rangle} \tag{4.11}$$

Using the step function approximation for $\langle\cos\varphi_0\rangle$ outlined in Section 3.3 again we can define the function separately in the first region between vortex cores and the second region corresponding to a vortex core as shown in Fig. 4.5.

v can be defined separately in the the two regions, from this point onwards the index (1) represents a quantity in region 1 and the index (2) a quantity in region 2.

$$v^{(1)} = D_+^1 e^{i(k_+^{(1)})x} + D_-^1 e^{i(k_-^{(1)})x}$$

$$v^{(2)} = D_+^2 e^{i(k_+^{(2)})(x-L)} + D_-^2 e^{i(k_-^{(2)})(x-L)}$$

The expression for $v^{(2)}$ is defined at $x - L$ for reasons of simplicity later on which is valid because of the periodic boundary conditions which will be used. So we can

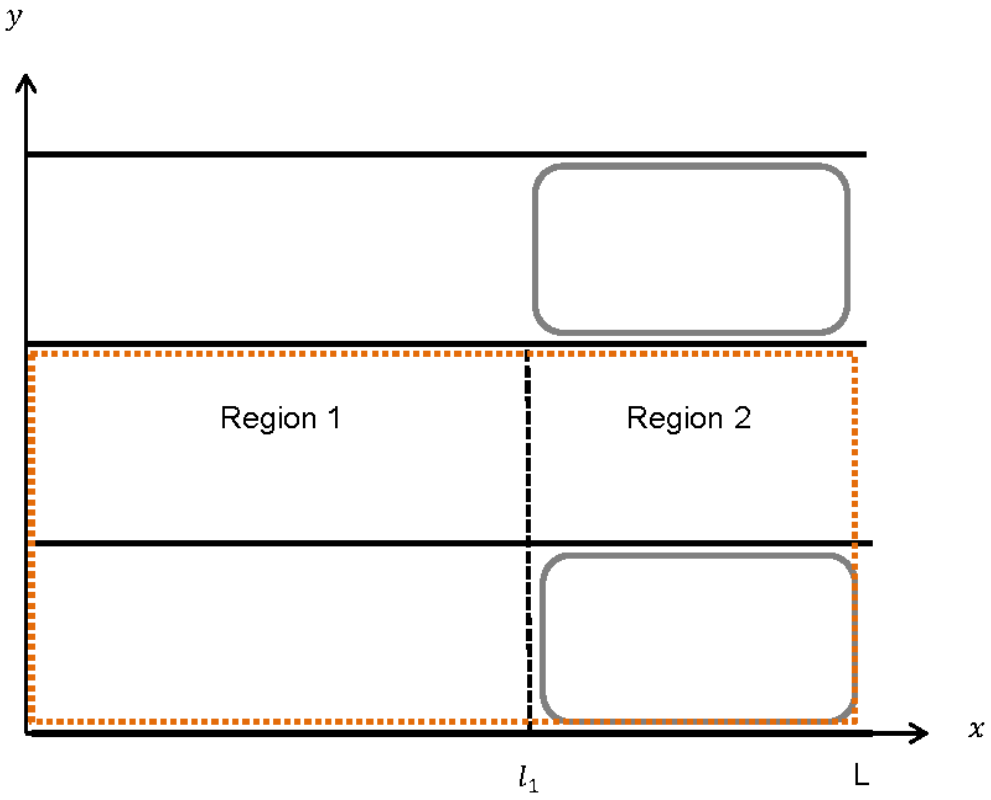

Figure 4.5: 2D representation of the Josephson-vortex photonic crystal with periodicity $L = l_1 + l_2$, where Region 1 represents the space between vortices of thickness l_1 along the x-axis and Region 2 represents the space where a vortex (Grey rectangle) is present, with diameter l_2.

apply the periodic boundary condition matching the period of the vortex lattice L for v where we require $v(x+L)^{(1)} = v(x)^{(2)}$, which gives the following condition on the coefficients

$$D_+^{(1)} + D_-^{(1)} = D_+^{(2)} + D_-^{(2)}. \tag{4.12}$$

We also need to apply these periodic boundary conditions to the first spatial deriva-

tive denoted by $v^{'}$ for which we require that $v^{'}(x+L)^{(1)} = v^{'}(x)^{(2)}$, this gives us the condition.

$$-ik(D_{+}^{(1)} + D_{-}^{(1)}) + \frac{2iq}{\gamma}\sqrt{\epsilon_1} = -ik(D_{+}^{2} + D_{-}^{2}) + \frac{2iq}{\gamma}\sqrt{\epsilon_2}, \tag{4.13}$$

where $\epsilon_{1,2} = 4\tilde{\omega}^2 - \langle \cos\varphi_0 \rangle_{1,2}$. We can combine Eq. (4.12) and Eq. (4.13) to give Eq. (4.14) and Eq. (4.15)

$$D_{+}^{(1)} = \frac{1}{2}(D_{+}^{(2)} + D_{-}^{(2)}) + \frac{1}{2}\frac{\sqrt{\epsilon_2}}{\sqrt{\epsilon_1}}(D_{+}^{(2)} - D_{-}^{(2)}) \tag{4.14}$$

$$D_{-}^{(1)} = \frac{1}{2}(D_{-}^{(2)} + D_{-}^{(2)}) - \frac{1}{2}\frac{\sqrt{\epsilon_2}}{\sqrt{\epsilon_1}}(D_{+}^{(2)} - D_{-}^{(2)}) \tag{4.15}$$

Now we also require that the two solutions are matched at the boundary between the two regions (At $x = l_1$ as defined above). Hence we use the condition $v^{(1)}(l_1) = v^{(2)}(l_1)$ in order to make v continuous at the boundary. Introducing the effective wavevectors α in region 1 and β in region 2

$$\alpha = \frac{2q}{\gamma}\sqrt{\epsilon_1},$$

$$\beta = \frac{2q}{\gamma}\sqrt{\epsilon_2},$$

we can write Eq. (4.16) as follows

$$D_{+}^{(1)}e^{i\alpha l_1} + D_{-}^{(1)}e^{-i\alpha l_1} = (D_{+}^{(2)}e^{-i\beta l_2} + D_{-}^{(2)}e^{i\beta l_2})e^{ikL}. \tag{4.16}$$

Matching the derivatives at the boundary $x = l_1$ using the condition $v^{'}(l_1)^{(1)} =$

$v^{'}(l_1)^{(2)}$ gives us

$$\epsilon_1(D_+^{(1)}e^{i\alpha l_1} - D_-^{(1)}e^{-i\alpha l_1}) = \epsilon_2(D_+^{(2)}e^{-i\beta l_2} + D_-^{(2)}e^{i\beta l_2})e^{ikL}. \tag{4.17}$$

Using all these four boundary conditions we can derive four simultaneous homogeneous equations for the coefficients and introducing new variables x and y given by

$$x = D_+^{(2)} + D_-^{(2)},$$

$$y = i(D_+^{(2)} - D_-^{(2)}),$$

$$D_+^{(1)} = \frac{1}{2}x + \frac{1}{2}\frac{\sqrt{\epsilon_2}}{\sqrt{\epsilon_1}}\frac{y}{i}, \tag{4.18}$$

$$D_-^{(1)} = \frac{1}{2}x - \frac{1}{2}\frac{\sqrt{\epsilon_2}}{\sqrt{\epsilon_1}}\frac{y}{i}. \tag{4.19}$$

Substituting Eq. (4.18) and Eq. (4.19) into first Eq. (4.16) and then Eq. (4.17) allows us to derive the following two homogeneous equations:

$$(\cos\alpha - e^{ikL}\cos\beta)x + (\frac{\sqrt{\epsilon_2}}{\sqrt{\epsilon_1}}\sin\alpha + \sin\beta e^{ikL})y = 0 \tag{4.20}$$

$$-(\frac{\sqrt{\epsilon_2}}{\sqrt{\epsilon_1}}e^{ikL}\sin\beta - \sin\alpha)x + (\frac{\sqrt{\epsilon_2}}{\sqrt{\epsilon_1}}\cos\alpha - \frac{\sqrt{\epsilon_2}}{\sqrt{\epsilon_1}}e^{ikL}\cos\beta)y = 0. \tag{4.21}$$

In order to solve the two simultaneous homogeneous Eq. (4.20) and Eq. (4.21) we can put them into a matrix form (4.22)

$$\begin{pmatrix} A & B \\ C & D \end{pmatrix} \begin{pmatrix} x \\ y \end{pmatrix} = 0 \tag{4.22}$$

The matrix elements A-D here are defined by

$$A = \cos\alpha - e^{ikL}\cos\beta$$

$$B = \frac{\sqrt{\epsilon_2}}{\sqrt{\epsilon_1}}\sin\alpha + e^{ikL}\sin\beta$$

$$C = \frac{\sqrt{\epsilon_2}}{\sqrt{\epsilon_1}}e^{ikL}\sin\beta - \sin\alpha$$

$$D = \frac{\sqrt{\epsilon_2}}{\sqrt{\epsilon_1}}\cos\alpha - \frac{\sqrt{\epsilon_2}}{\sqrt{\epsilon_1}}e^{ikL}\cos\beta$$

Eq. (4.22) has two solutions, a trivial solution when the amplitudes are equal to zero so we have no waves at all and the solution where the matrix determinant is equal to zero. Setting the determinant to zero and rearranging allows us to derive an expression for the second harmonic spectrum $\omega(k)$.

The second harmonic spectrum given here by Eq. (4.23) has the same basic form as the first harmonic spectrum (i.e. Eq. (3.13)). The only change for the case of the second harmonic is that the values of the effective wavevectors α and β are different to the first harmonic as defined below:

$$\cos(kd_x) = \cos(\alpha l_1)\cos(\beta l_2) - \frac{\alpha^2+\beta^2}{2\alpha\beta}\sin\alpha l_1 \sin\beta l_2, \tag{4.23}$$

$$\alpha_l = k_0(q)\sqrt{l^2\omega^2 - 1},$$

$$\beta_l = k_0(q)\sqrt{l^2\omega^2 + \pi\sqrt{h_{ab} - 1}},$$

l is an integer that labels the harmonic number, i.e. 1 for the first harmonic and 2 for the second harmonic; k_0 is defined by:

$$k_0^2 = \frac{1 + l^2\lambda_{ab}^2 q^2}{\lambda_c^2}.$$

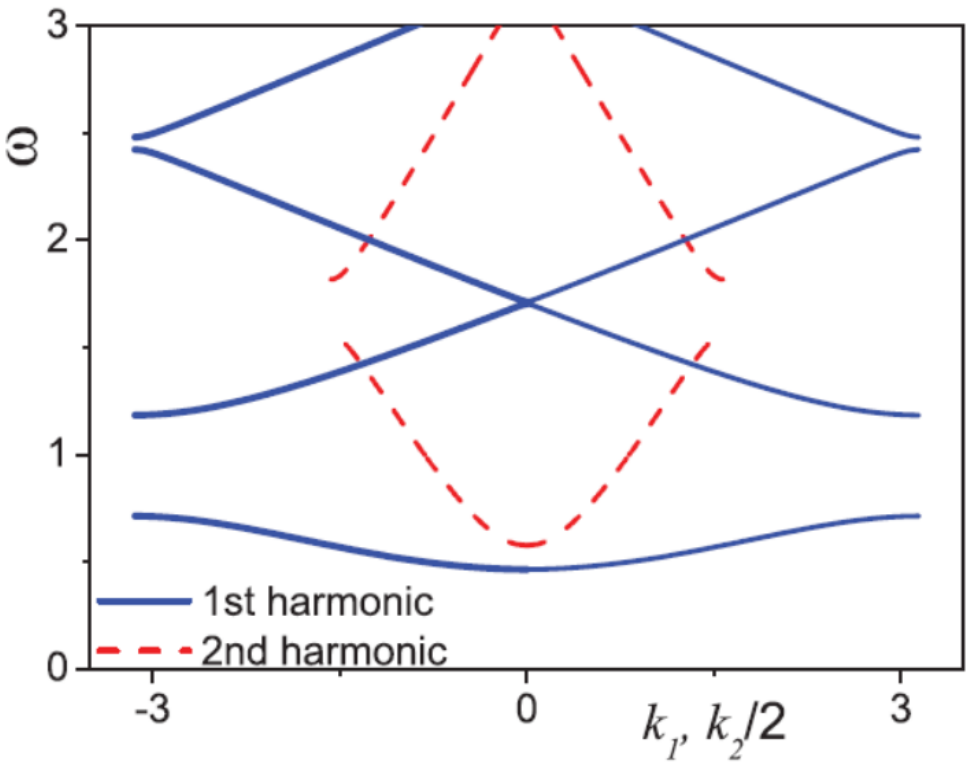

Figure 4.6: The linear spectra for the first harmonic $\omega(k_1)$) (blue line) and second harmonic $\omega(k_2)$) (red dashed line) in the JV photonic crystal for $h_{ab} = 0.2$. The scaling of the x-axis for the first and second harmonics is so that crossing points correspond to the resonance condition $k_2 = 2k_1$. Reprinted figure with permission from [101]. Copyright (2012) by the American Physical Society.

Fig. 4.6 shows that both the first and second harmonic spectra have the same basic form and both display a photonic bandgap in their spectrum. There are a number of crossing points for the spectra of the two harmonics. Resonances for the second harmonic can be shown to occur where the resonance condition $k_2 = 2k_1$ is satisfied, hence the reason for the rescaling of the x-axis for k_2. With this rescaled axis we would expect the crossing points of these two spectra to be significant in terms of resonances for the second harmonic.

4.4 Numerical results

Using a second order multiderivative numerical method for the integration of ordinary differential equations [100] ,we can calculate the amplitudes for the first harmonic $\psi_1(x)$ and second harmonic $\psi_2(x)$ through the crystal based on Eq. (4.4) and Eq. (4.5). To simplify the problem numerically we can introduce the new variable $P_{1,2} = \psi'_{1,2}$ and a normalised displacement $\tilde{x} = \frac{\sqrt{h_{ab}}x}{2l_0}$ leaving us with Eq. (4.24) and Eq. (4.25).

$$(\langle\cos\varphi_0\rangle - \tilde{\omega}^2)\psi_1(\tilde{x}) - \frac{\lambda_c^2}{(1+\lambda_{ab}^2 q^2)}\ P_1^{'} = \frac{\langle\sin\varphi_0\rangle}{2}\psi_1\psi_2, \tag{4.24}$$

$$(\langle\cos\varphi_0\rangle - 4\tilde{\omega}^2)\psi_2(\tilde{x}) - \frac{\lambda_c^2}{(1+4\lambda_{ab}^2 q^2)}\ P_2^{'} = \frac{\langle\sin\varphi_0\rangle}{4}\psi_1^2. \tag{4.25}$$

The numerical values of $\psi_{1,2}$ and $P_{1,2}$ can be calculated at successive points based on the second order Taylor expansions given in Eq. (4.26) and Eq. (4.27).

$$P_{1,2}(\tilde{x}+d\tilde{x}) = P_{1,2}(\tilde{x}) + P'_{1,2}(\tilde{x})d\tilde{x} + \frac{1}{2!}P''_{1,2}(\tilde{x})d\tilde{x}^2, \tag{4.26}$$

$$\psi_{1,2}(\tilde{x}+d\tilde{x}) = \psi_{1,2}(\tilde{x}) + P_{1,2}(\tilde{x})d\tilde{x} + \frac{1}{2!}P'_{1,2}(\tilde{x})d\tilde{x}^2. \tag{4.27}$$

Based on Eq. (4.24) and Eq. (4.25) the first spatial derivatives $P'_{1,2}$ can be written as :

$$P'_1 = \frac{4l_0^2q^2}{h_{ab}\gamma^2}\left[(\langle\cos\varphi_0\rangle - \tilde{\omega}^2)\psi_1(\tilde{x}) - \frac{\langle\sin\varphi_0\rangle}{2}\psi_1(\tilde{x})\psi_2(\tilde{x})\right],$$

$$P'_2 = \frac{4l_0^2q^2}{h_{ab}\gamma^2}\left[(\langle\cos\varphi_0\rangle - 4\tilde{\omega}^2)\psi_2(\tilde{x}) - \frac{\langle\sin\varphi_0\rangle}{4}\psi_1^2(\tilde{x})\right].$$

The second derivatives can be found by differentiating analytically once more with respect to $\tilde{x}$.

$$P''_1 = \frac{4l_0^2q^2}{h_{ab}\gamma^2}\left[(\langle\cos\varphi_0\rangle - \tilde{\omega}^2)P_1 + \langle\cos\varphi_0\rangle'\psi_1 - \frac{\langle\sin\varphi_0\rangle}{2}(P_1\psi_2 + \psi_1P_2) - \frac{\langle\sin\varphi_0\rangle'}{2}\psi_1\psi_2\right],$$

$$P''_2 = \frac{16l_0^2q^2}{h_{ab}\gamma^2}\left[(\langle\cos\varphi_0\rangle - 4\tilde{\omega}^2)P_2 + \langle\cos\varphi_0\rangle'\psi_2 - \frac{\langle\sin\varphi_0\rangle}{4}2P_1\psi_1 - \frac{\langle\sin\varphi_0\rangle'}{4}\psi_1^2\right].$$

Using the change of variables introduced here, expressions (4.7) and (4.8) must be rewritten as :

$$\langle \cos \varphi_0 \rangle (\tilde{x}) = \frac{s}{d_y} \frac{4\tilde{x}^2 - h_{ab}}{4\tilde{x}^2 + h_{ab}},$$

$$\langle \sin \varphi_0 \rangle (\tilde{x}) = -\frac{s}{d_y} \frac{4\sqrt{h_{ab}}\tilde{x}}{4\tilde{x}^2 - h_{ab}}.$$

The derivatives of $\langle \cos \varphi_0 \rangle$ and $\langle \sin \varphi_0 \rangle$ can be calculated analytically using the product rule and are given by :

$$\langle \cos \varphi_0 \rangle' (\tilde{x}) = \frac{s}{d_y} \frac{16 h_{ab} \tilde{x}}{(4\tilde{x}^2 + h_{ab})^2},$$

$$\langle \sin \varphi_0 \rangle' (\tilde{x}) = \frac{s}{d_y} \frac{4\sqrt{h_{ab}}(4\tilde{x}^2 - h_{ab})}{(4\tilde{x}^2 + h_{ab})^2}.$$

We apply boundary conditions, where the value of $\psi_2(0) = 0$ at $x = 0$, i.e. at the interface between the vacuum and the JV photonic crystal, assuming that the second harmonic wave is generated within the crystal due to nonlinearity. For the first harmonic $\psi_1(0) = 0.5$, a small amplitude at the crystal interface. Eq. (4.26) and Eq. (4.27) can be used to calculate successive amplitudes at $(\tilde{x} + d\tilde{x})$ which can be computed as a function of distance $\tilde{x}$ of propagation through the crystal as shown plotted in Fig. 4.7. The average value of the second harmonic amplitude has been calculated for each input frequency to find resonances where the amplitude increases.

We can define a tuning parameter $Q = \frac{d_x^2(1+\lambda_{ab}^2 q^2)}{\lambda_c^2}$ which can be used to vary the frequency of resonances for the second harmonic. The value of Q depends on both the applied field h_{ab} which will affect the vortex lattice spacing as given by Eq.

(3.10), as well as the y axis wavevector q which is altered by tilting the layered superconductor with respect to the incoming radiation.

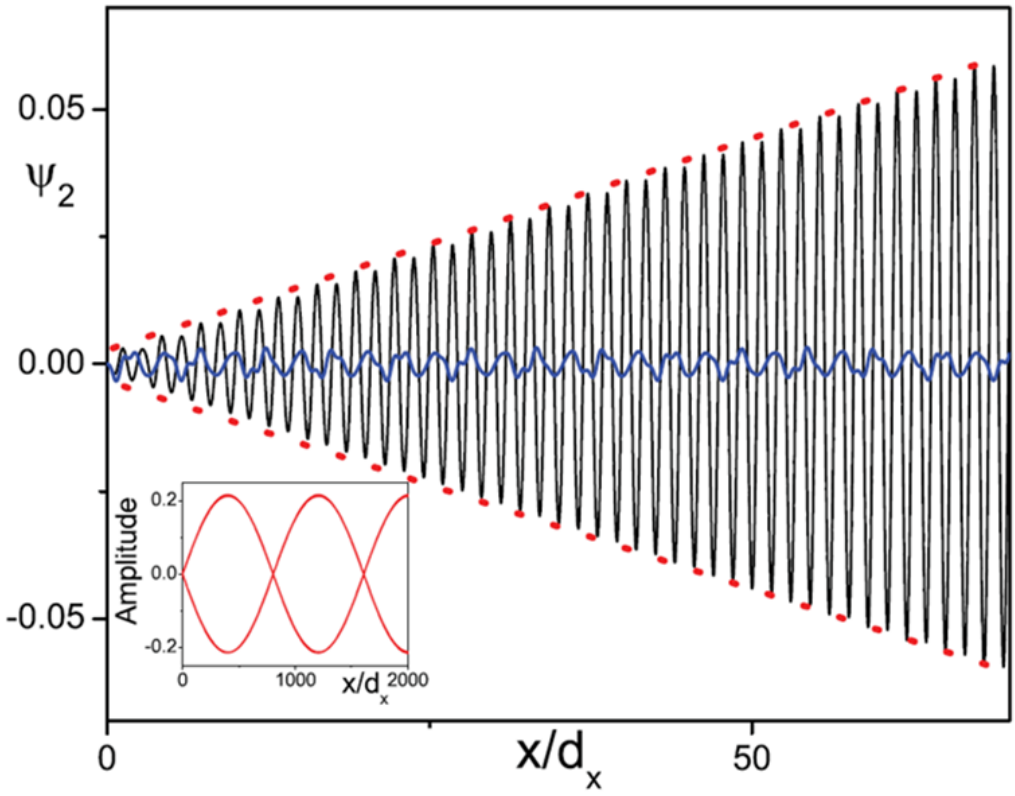

Figure 4.7: Spatial distribution $\psi_2(x)$ for the second harmonic near the resonance $\omega^{(1)}$ at $\omega = 3.5$ (black line) and away from this resonance (blue line) for $Q = 0.09$. By plotting the amplitude of the oscillations shown by the dashed line on the main plot we can observe the larger scale oscillations of the second harmonic amplitude. Reprinted figure with permission from [101]. Copyright (2012) by the American Physical Society.

It can be seen from Fig. 4.7 that when plotting the amplitude ψ_2 as a function of propagation distance there is a sharp contrast in behaviour of the second harmonic away from resonance and close to resonance. Away from resonance for the second harmonic the amplitude is relatively small and constant, the disordered oscillation in this case shows that the wavelengths of the two harmonics are not commensurate

so we have destructive interference of the two. Close to a resonance frequency for the second harmonic we see ordered oscillations with an overall amplitude that increases steadily to a much larger value, eventually showing a saturation behaviour as the second harmonic reaches a maximum value. Over larger distances we see a long range oscillation in the amplitude which is shown by the envelope function plotted in the inset of Fig. 4.7.

The different scales of oscillation of the second harmonic amplitude shown here display the same behaviour qualitatively as for the electric field in a nonlinear optical photonic crystal [60], whereby the linear oscillations are modulated in amplitude over a larger distance due to the weak nonlinearity(see Fig. 3.4).

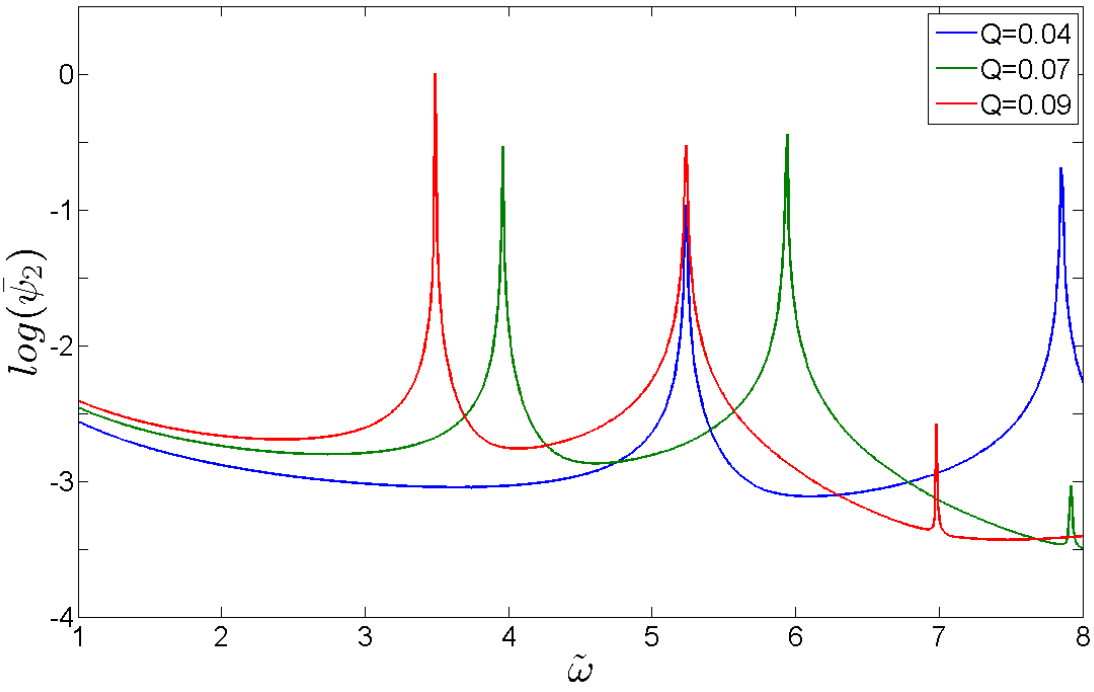

Figure 4.8: Second harmonic resonances as a function of frequency for different values of the tuning parameter Q as shown in the plot legend. Amplitudes are normalised by the largest resonance and plotted on a log_{10} scale. $l_0/d_x = 0.2$, $\psi_2(0) = \psi_2'(0) = 0$, $\psi_1(0) = 0.5$, $\psi_1'(0) = 0.2$, integration step $d\tilde{x} = 0.001$.

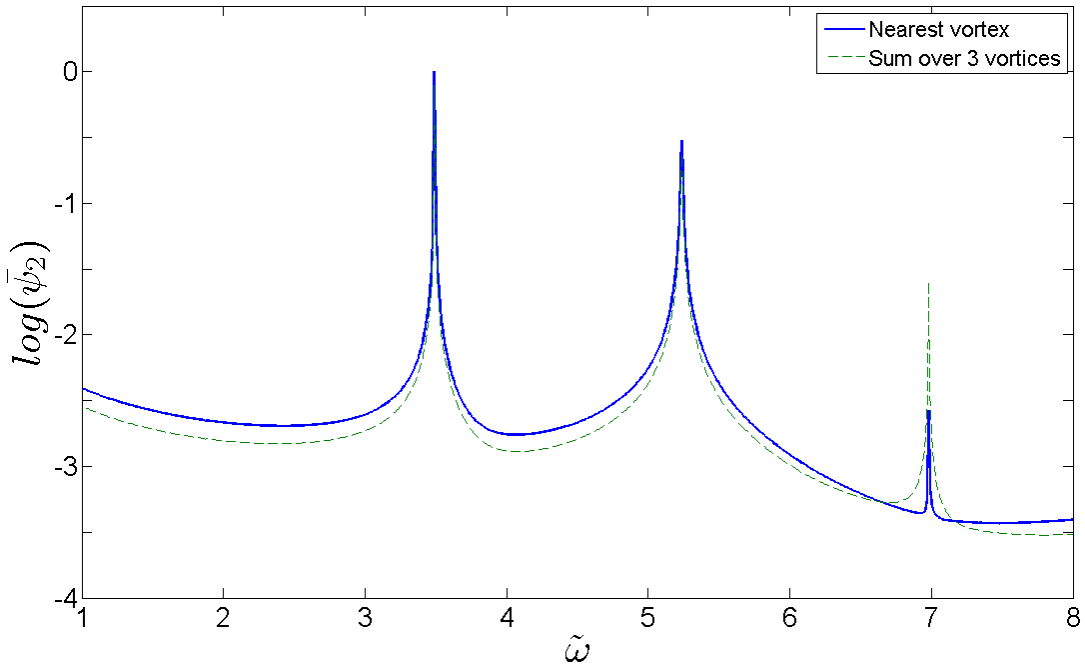

Figure 4.9: $\bar{\psi}_2$ as a function of $\tilde{\omega}$ for the nearest vortex approximation (blue) compared to the case where a sum over 3 vortices has been used (green dashed line), $Q = 0.09$, all other parameters as Fig. 4.8.

The frequencies at which these resonances are displayed can be calculated by finding the maximum value $\bar{\psi}_2$ reached by the long range oscillation of ψ_2. At resonance $\bar{\psi}_2$ is enhanced by several orders of magnitude when plotted on a log scale. This is shown clearly in Fig. 4.8 for a number of values of the resonance tuning parameter Q. Increasing the value of Q has the effect of reducing the frequency $\tilde{\omega}$ of resonances $\omega^{(1)}$ and $\omega^{(2)}$. The resonances also correspond to the crossing points of the first and second harmonic linear spectra calculated in Section 4.3.

Fig. 4.9 shows the effect on the resonances of summing over a larger number of vortices rather than just the nearest vortex approximation, it can be seen that there is no change in the frequencies of resonances although the amplitude of the third resonance at $\tilde{\omega} = 6.98$ in particular is larger when summing over three vortices. This indicates that for locating resonances of the second harmonic, the nearest vortex approximation for $\langle \sin \varphi_0 \rangle$ is sufficient. The change to the resonance amplitudes when summing over five vortices is negligible.

Using Eq. (3.10) we can write the resonance tuning parameter as $Q = \frac{4l_0^2(1+\lambda_{ab}^2)}{\lambda_c^2} \frac{q^2}{h_{ab}}$ to explicitly show its dependence on h_{ab}. It makes sense to vary the two parameters q and h_{ab} separately whilst holding the other constant to investigate the affect on the second harmonic resonance frequencies. At this point we also introduce a normalised wavevector $\tilde{q} = q/q_{max}$, where $q_{max} = 0.3\pi/s$, above this value the continuous limit of the sine-Gordon equation is no longer valid and the discrete coupled sine-Gordon equations should be used.

Fig. 4.10 shows the shift in the resonance frequencies from Fig. 4.8 when $\tilde{q}$ is varied over a wider range of values while holding h_{ab} (and hence d_x) constant. As the y-axis wavevector q is increased, the resonances are shifted to lower frequency. This corresponds to increasing the component of the wavevector perpendicular to the layers.

Fig. 4.11 shows that the resonance frequencies can also be shifted to higher frequency by increasing the strength of the applied magnetic field h_{ab}. In standard units the magnetic field strengths used here are in the approximate range 0.1-1T. It's clear though that the second harmonic resonances can be readily tuned by varying the applied magnetic field as well as the relative transverse and longitudinal wavevectors.

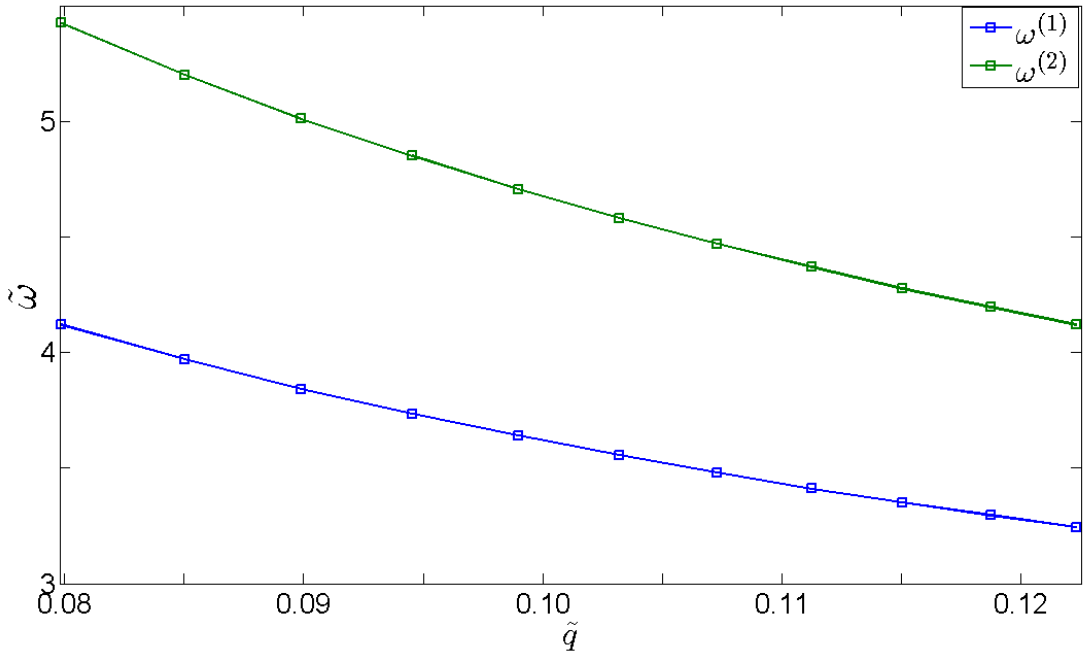

Figure 4.10: Dependence of the resonance frequencies from Fig. 4.8 on the normalised y-axis wavevector $\tilde{q}$ with h_{ab} fixed so that $l_0/d_x = 0.2$. All other parameters are the same as in Fig. 4.8.

4.5 Second harmonic resonance approximation

The next question to be asked is whether the second harmonic resonances found numerically in Section 4.4 can be described by an analytical method. Following the same general approach that was described in Section 3.2 for the analysis of nonlinear optical photonic crystals. We can separate the linear and nonlinear parts of the solution by defining a slowly varying nonlinear amplitude A_1 for the first harmonic and A_2 for the second harmonic, so the solutions can be represented by $\psi_1 = A_1\psi_{L1}$ and $\psi_2 = A_2\psi_{L2}$. The linear solutions to Eq. (4.9) are represented by their real parts, which can be given by

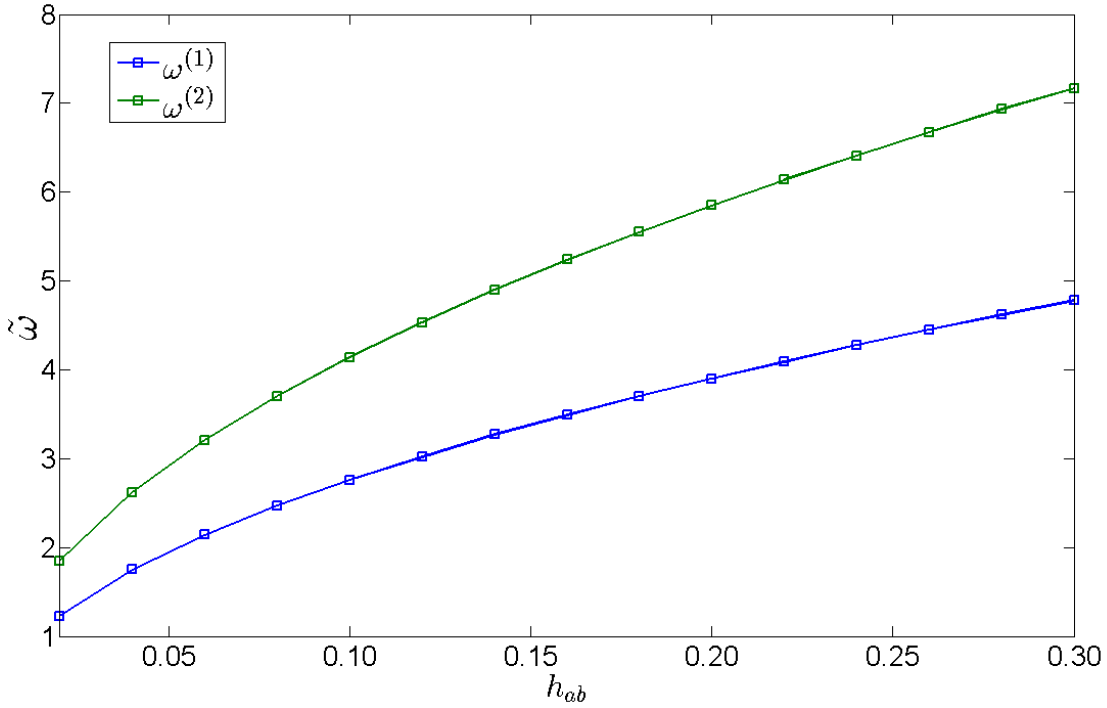

Figure 4.11: Dependence of the resonance frequencies from Fig. 4.8 on the applied magnetic field h_{ab}. $\tilde{q} = 0.127$ All parameters are the same as in Fig. 4.8

$$\psi_{L1} = Re(\psi_{L1}) = u_1 \cos k_1 x - v_1 \sin k_1 x, \tag{4.28}$$

$$\psi_{L2} = Re(\psi_{L2}) = u_2 \cos k_2 x - v_2 \sin k_2 x. \tag{4.29}$$

Now we can assume that the nonlinear amplitudes are slowly varying in comparison to the linear solutions and in doing so neglect the term containing the second spatial derivatives $A''_{1,2}$. More explicitly we can assume that $A_{1,2}/dA_{1,2}/dx \gg \lambda_{1,2} \gg d_x$. Substituting the linear solutions above into Eq. (4.4) and Eq. (4.5) we can obtain two equations for these nonlinear amplitudes.

$$\psi_{L1}^{'}A_1^{'} = -\frac{q^2}{\gamma^2}\frac{\langle \sin\varphi_0 \rangle}{2}\psi_{L1}\psi_{L2}A_1A_2 \tag{4.30}$$

$$\psi_{L2}^{'}A_2^{'} = -\frac{q^2}{\gamma^2}\langle \sin\varphi_0 \rangle \psi_{L1}^2 A_1^2 \tag{4.31}$$

Now we can utilise the fact that there are 3 different spatial periods to consider in this problem. The first and shortest is the x-axis unit cell of the vortex lattice d_x which is much smaller than the wavelengths of the JPWs $\lambda_{1,2} = 2\pi/k_{1,2}$ when considering waves in the first Brillouin zone $\pm\pi/d_x$. However these wavelengths are still much shorter than the scale of variation of the nonlinear amplitudes for weak nonlinearity. This allows us to average the equations on two scales, the first being within the unit cell d_x and the second being over a wavelength of the JPWs. Eq. (4.30) and Eq. (4.31) can be expressed in the simplified form given in Eq. (4.32) and Eq. (4.33),

$$A_1^{'} = I_1 A_1 A_2, \tag{4.32}$$

$$A_2^{'} = I_2 A_1^2, \tag{4.33}$$

where I_1 and I_2 are the values of the integrals which are not functions of x, defined as

$$
\begin{aligned}
I_1 &= -\frac{q^2 \int_0^L dx \langle \sin\varphi_0 \rangle [\mu_1(u_1u_2 + v_1v_2) + \eta_1(u_1v_2 - v_1u_2)]}{4\gamma^2 \int_0^L dx(\mu_1^2 + \eta_1^2)} \\
I_2 &= -\frac{q^2 \int_0^L dx \langle \sin\varphi_0 \rangle [\mu_2(u_1^2 - v_1^2) + 2\eta_2 u_1 v_1]}{2\gamma^2 \int_0^L dx(\mu_2^2 + \eta_2^2)}
\end{aligned} \tag{4.34}
$$

with $\mu_j = u_j' - k_j v_j$, $\eta_j = v_j' + k_j u_j$ and $j = 1$ or 2 (see Appendix 1 for details).

Eq. (4.32) and Eq. (4.33) are valid in the resonance points $k_2 = 2k_1$, the complete procedure for averaging them is given in the appendix. It's now possible to find analytical solutions for A_1 and A_2 which are valid at resonance points for the second harmonic.

Dividing Eq. (4.32) by Eq. (4.33) it's possible to separate A_1 and A_2 and form an integrable expression Eq. (4.35). Using the boundary condition $A_2(0) = 0$ which comes from assuming that the second harmonic is generated only within the sample and not the vacuum. The second condition is $A_1(0) = A_0$ which comes from the assumption that the first harmonic has a non zero amplitude A_0 at the sample boundary $x = 0$.

$$
A_1 A_1^{'} = \frac{I_1}{I_2} A_2 A_2^{'} \tag{4.35}
$$

Using the boundary conditions described above, Eq. (4.35) can be integrated, giving Eq. (4.36) linking A_1 and A_2.

$$
A_1^2 = \frac{I_1}{I_2} A_2^2 + A_0^2. \tag{4.36}
$$

This can be used to decouple Eq. (4.32) and Eq. (4.33), resulting in

$$A_2^{'} = I_1 A_2^2 + I_2 A_0^2. \tag{4.37}$$

The solutions to Eq. (4.37) will depend strongly in the sign of the integrals I_1 and I_2, when these integrals have the same signs the solutions for nonlinear first and second harmonic amplitudes can be written in the form given by Eq. (4.38) and Eq. (4.39).

$$A_1(x) = A_0 \mathrm{sec}(A_0 \sqrt{I_1 I_2} x) \tag{4.38}$$

$$A_2(x) = A_0 \sqrt{\frac{I_2}{I_1}} \tan(A_0 \sqrt{I_1 I_2} x) \tag{4.39}$$

These solutions have singularities on the scale $x = \pi/2A_0\sqrt{I_1 I_2}$ which we can refer to as a Type-1 resonance. Fig. 4.12 shows the divergence of these solutions for both the first and second harmonics. When compared to the envelope function of the first and second harmonic amplitudes from Section 4.4 (plotted in Fig. 4.12), a good agreement between analytical and numerical results can be seen.

For the case where the integrals I_1 and I_2 have opposite signs we can find solutions given by Eq. (4.40) and Eq. (4.41) which have so singularities, we can refer to this as a Type-2 resonance the distribution of which can be plotted in Fig. 4.13.

$$A_1(x) = A_0 \mathrm{sech}(A_0 \sqrt{I_1 |I_2|} x) \tag{4.40}$$

$$A_2(x) = -A_0 \sqrt{\frac{|I_2|}{I_1}} \tanh(A_0 \sqrt{I_1 |I_2|} x) \tag{4.41}$$

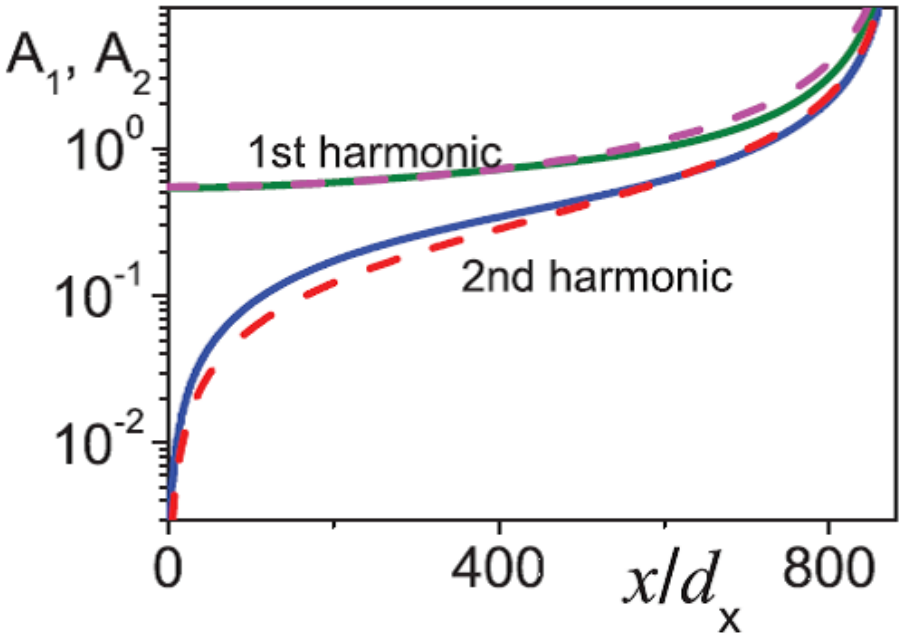

Figure 4.12: Harmonic amplitudes against normalised distance x/d_x from the sample surface. Solid black curves were simulated using Eq. 4.4 and Eq. 4.5 at the resonance $\omega = 3.49$ with other parameters the same as Fig. 4.7. The dashed curves are solutions of (4.38) and (4.39) in the resonance approximation for a Type-1 resonance for $\sqrt{I_1 I_2} = 0.0036$ and $\sqrt{I_2/I_1} = 0.65$. Reprinted figure with permission from [101]. Copyright (2012) by the American Physical Society.

Since the solutions 4.38 and 4.39 diverge at the resonance point it's necessary to detune slightly from resonance by a small amount $\delta k = 2k_1 - k_2$ to plot a finite distribution of the second harmonic amplitude. By doing this we can derive the expressions Eq. 4.42 and Eq. 4.43.

$$A_1^{'} = \tilde{I}_1 A_1 A_2 \cos(\delta k x + \alpha_1) \tag{4.42}$$

$$A_2^{'} = \tilde{I}_2 A_1^2 \cos(\delta k x + \alpha_2) \tag{4.43}$$

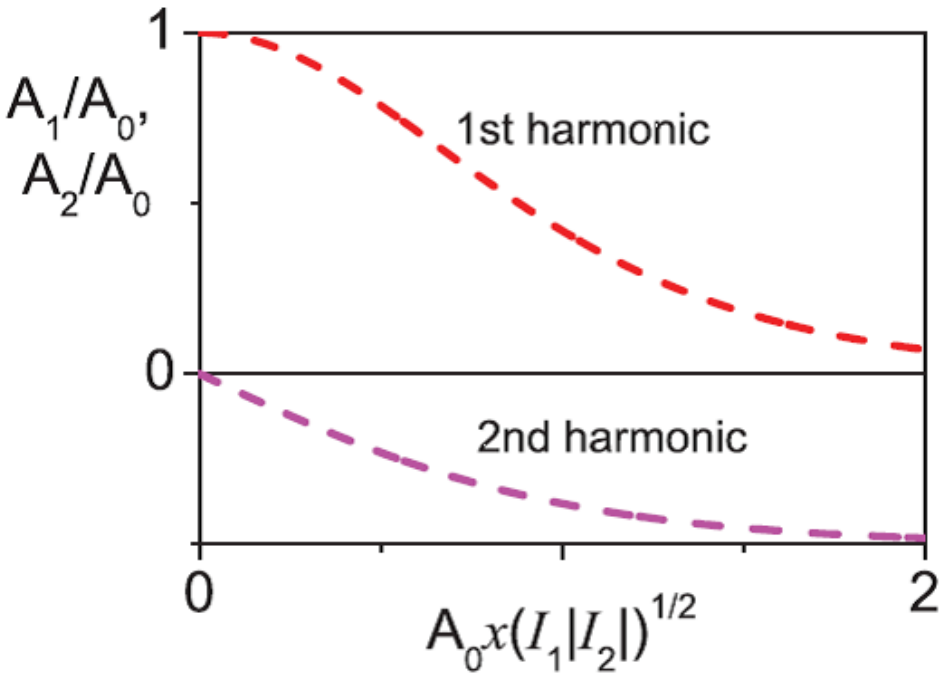

Figure 4.13: Harmonic amplitudes against normalised distance $A_0 x\sqrt{I_1 I_2}$ from the sample surface. The dashed curves are solutions of (4.40) and (4.41) in the resonance approximation for a type-2 resonance for $\sqrt{I_2/I_1} = 0.5$. Reprinted figure with permission from [101]. Copyright (2012) by the American Physical Society.

For frequencies slightly detuned from resonance we can derive analytical solutions Eq. 4.44 and Eq. 4.45,

$$A_1(x) = A_0 \sec(A_0\sqrt{\tilde{I}_1\tilde{I}_2}\sin(\delta k x)/\delta k), \tag{4.44}$$

$$A_2(x) = A_0\sqrt{\frac{\tilde{I}_2}{\tilde{I}_1}}\tan(A_0\sqrt{\tilde{I}_1\tilde{I}_2}\sin(\delta k x)/\delta k), \tag{4.45}$$

these can again be plotted against the numerical simulations covered in Section 4.4 as shown in Fig. 4.14. Extremely good agreement between numerical simulation and analytical resonance approximation can be displayed for the first and second

harmonic distributions close to a type-2 resonance for the case where $|\delta k|/k_2 \ll 1$. For the case shown in Fig. 4.14, we require that $\delta k \gtrapprox 10^{-3}$ for the solutions to Eq. 4.44 and Eq. 4.45 to not be divergent.

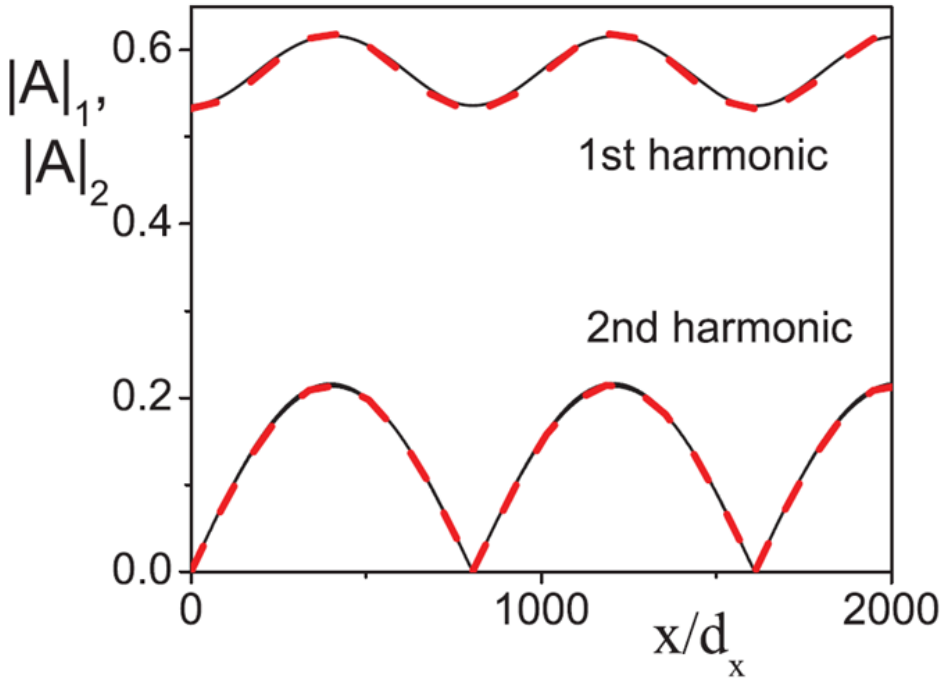

Figure 4.14: Harmonic amplitudes against normalised distance x/d_x from the sample surface. The solid black line was obtained by numerical simulation of Eq. (4.4) and Eq. (4.5) at $\omega = 3.5$(near but not at resonance). Other parameters correspond to Fig. 4.7. The dashed curve is the solution from (4.44) and (4.45) in the near-resonance approximation for $\sqrt{\tilde{I}_1\tilde{I}_2}/\delta k = 0.015$, $\sqrt{\tilde{I}_2/\tilde{I}_1} = 56$, $\alpha = 0$ and $\delta k = 0.004$. Reprinted figure with permission from [101]. Copyright (2012) by the American Physical Society.

Chapter 5

Third harmonic generation

Now we know from the results of the previous chapter it is possible to produce second harmonic resonances in the JV photonic crystal. The next obvious step is to expand the nonlinearity of the Josephson medium to third order and attempt to locate resonances for the third harmonic. We can extend the approach used in Chapter 4.

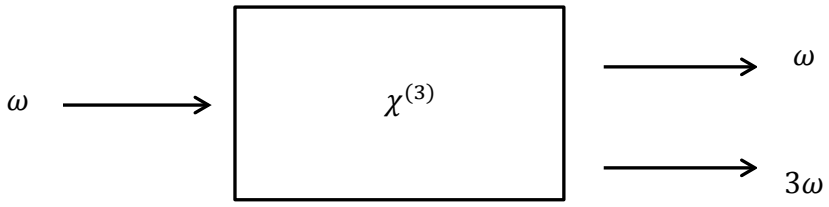

Figure 5.1: Schematic for third harmonic generation in a nonlinear material with non-zero third order susceptibility $\chi^{(3)}$ represented by the rectangular box. The left arrow represents an input at frequency ω and the two right arrows represent the waves generated from the crystal at ω (first harmonic) and 3ω (third harmonic).

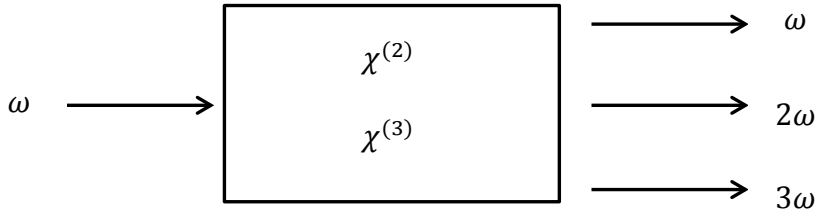

Figure 5.2: Schematic for combined second and third harmonic generation in a nonlinear material with non-zero values of both second order susceptibility $\chi^{(2)}$ and third order susceptibility $\chi^{(3)}$.

As shown in Fig. 5.1 above, a nonlinear material with third order susceptibility $\chi^{(3)}$ should produce a third harmonic at frequency 3ω in response to an applied electromagnetic wave at frequency ω. A material with nonzero values of both $\chi^{(2)}$ and $\chi^{(3)}$ can generate second and third harmonics simultaneously as illustrated in Fig. 5.2. To take into account the possibility of feedback from the third harmonic to the second harmonic, the second order susceptibility will also be included in the analysis for this chapter.

5.1 Deriving the third harmonic equations

The principle to derive the equations for third harmonic amplitudes is the same as in the previous chapter for second harmonic generation, we start with the continuous limit of the coupled sine-Gordon equations (Eq. 6.1) and substitute the solution Eq. (5.1) where $\psi_{1,2,3}$ represent the amplitudes for first, second and third harmonics respectively.

$$\varphi_1 = \psi_1 \cos(\omega t - qy) + \psi_2 \cos(2\omega t - 2qy) + \psi_3 \cos(3\omega t - 3qy) \qquad (5.1)$$

This time when taking the Taylor expansion of the term $\sin\varphi$ we include the third order term proportional to φ^3 so the full expansion is given by $\sin\varphi \approx \sin\varphi_0 + (\cos\varphi_0)\varphi_1 - (\sin\varphi_0)\varphi_1^2/2 - (\cos\varphi_0)\varphi_1^3/6$. Using this expansion and the substitution (5.1), three equations (Eq. (5.2),Eq. (5.3) and Eq. (5.4)) can be derived for the three harmonic amplitudes $\psi_{1,2,3}$ respectively.

$$(\langle\cos\varphi_0\rangle - \omega^2)\psi_1 - \frac{\lambda_c^2}{(1+\lambda_{ab}^2 q^2)}\psi_1'' = \frac{\langle\sin\varphi_0\rangle}{2}(\psi_1\psi_2) + \frac{\langle\cos\varphi_0\rangle}{8}(\psi_1^3), \tag{5.2}$$

$$(\langle\cos\varphi_0\rangle - 4\omega^2)\psi_2 - \frac{\lambda_c^2}{(1+4\lambda_{ab}^2 q^2)}\psi_2'' = \frac{\langle\sin\varphi_0\rangle}{2}(\frac{1}{2}\psi_1^2), \tag{5.3}$$

$$(\langle\cos\varphi_0\rangle - 9\omega^2)\psi_3 - \frac{\lambda_c^2}{(1+9\lambda_{ab}^2 q^2)}\psi_2'' = \frac{\langle\sin\varphi_0\rangle}{2}\psi_1\psi_2 + \frac{\langle\cos\varphi_0\rangle}{4}(\frac{1}{6}\psi_1^3). \tag{5.4}$$

We make the assumption that the magnitude a of the first harmonic amplitude is subject to the condition $a \ll 1$, so we are considering a small amplitude input wave. Based on this the second and third harmonic amplitudes are proportional to a^2 and a^3 respectively. Again as with the second harmonic case, we are ignoring all terms higher than the order of expansion in this case, i.e. all terms higher order than a^3. Eq. (5.3) for the second harmonic amplitude has no third order term since these terms are higher order with respect to a. This indicates that the feedback to the second harmonic from this model is negligible.

5.2 Numerical results

As for the second harmonic analysis we can introduce new variables $P_{1,2,3} = \psi_{1,2,3}$ to reduce the equations to first order and simplify the problem numerically. A

second order Taylor expansion about each point seems to be sufficient for this calculation, where the expansions are given by Eq. (5.5) and Eq. (5.6).

$$P_{1,2,3}(\tilde{x}+d\tilde{x}) = P_{1,2,3}(\tilde{x}) + P'_{1,2,3}(\tilde{x})d\tilde{x} + \frac{1}{2!}P''_{1,2,3}(\tilde{x})d\tilde{x}^2 \tag{5.5}$$

$$\psi_{1,2,3}(\tilde{x}+d\tilde{x}) = \psi_{1,2,3}(\tilde{x}) + P_{1,2,3}(\tilde{x})d\tilde{x} + \frac{1}{2!}P'_{1,2,3}(\tilde{x})d\tilde{x}^2 \tag{5.6}$$

To be concise the expressions for the derivatives $P'_{1,2,3}$ and second derivatives $P''_{1,2,3}$ are given in Appendix 2 and the values of $\langle\cos\varphi_0\rangle(\tilde{x})$ and $\langle\sin\varphi_0\rangle(\tilde{x})$ are the same as in Chapter 4 using the nearest vortex approximation for $\langle\sin\varphi_0\rangle(\tilde{x})$. Using this model we can calculate the values of $\psi_{1,2,3}(x)$ for many values of $\tilde{\omega}$. Once again the amplitudes for both second and third harmonics are set to zero at the crystal interface ($x = 0$), assuming both harmonics are created within the JV photonic crystal.

Plotting the second harmonic resonances using the third order expansion in this chapter (shown in Fig. 5.3) shows that resonances occur at the same values of $\tilde{\omega}$ as in the previous chapter, which validates the approach used here. This is expected since there is no contribution from the third order nonlinearity in Eq. (5.3).

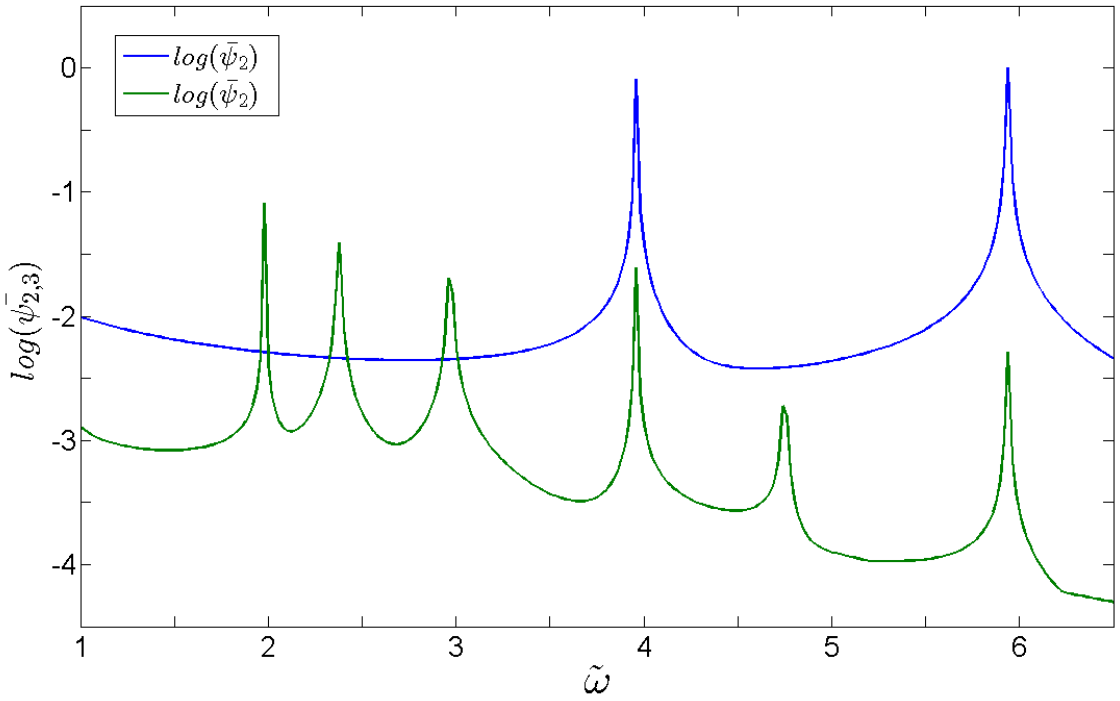

Figure 5.3: Third harmonic resonances(green) as a function of frequency for $Q = 0.07$, also shown are the second harmonic resonances (blue). All amplitudes are normalised by the largest second harmonic resonance and plotted on a log_{10} scale. $l_0/d_x = 0.2$, $\psi_{2,3}(0) = \psi'_{2,3}(0) = 0$,$\psi_1(0) = 0.5$,$\psi'_1(0) = 0.2$,$dx = 0.001$.

It can be clearly seen that there are two types of resonance here, shared resonances for the second and third harmonics as well as resonances exclusive to the third harmonic only. The third harmonic resonances are much smaller in amplitude than the second harmonic resonances by at least an order of magnitude for the shared resonance cases. Third harmonic resonances also seem to decay in amplitude faster above the plasma frequency. However for the cases where we have a resonance for the third harmonic alone, the amplitude can exceed that of the second harmonic by an order of magnitude.

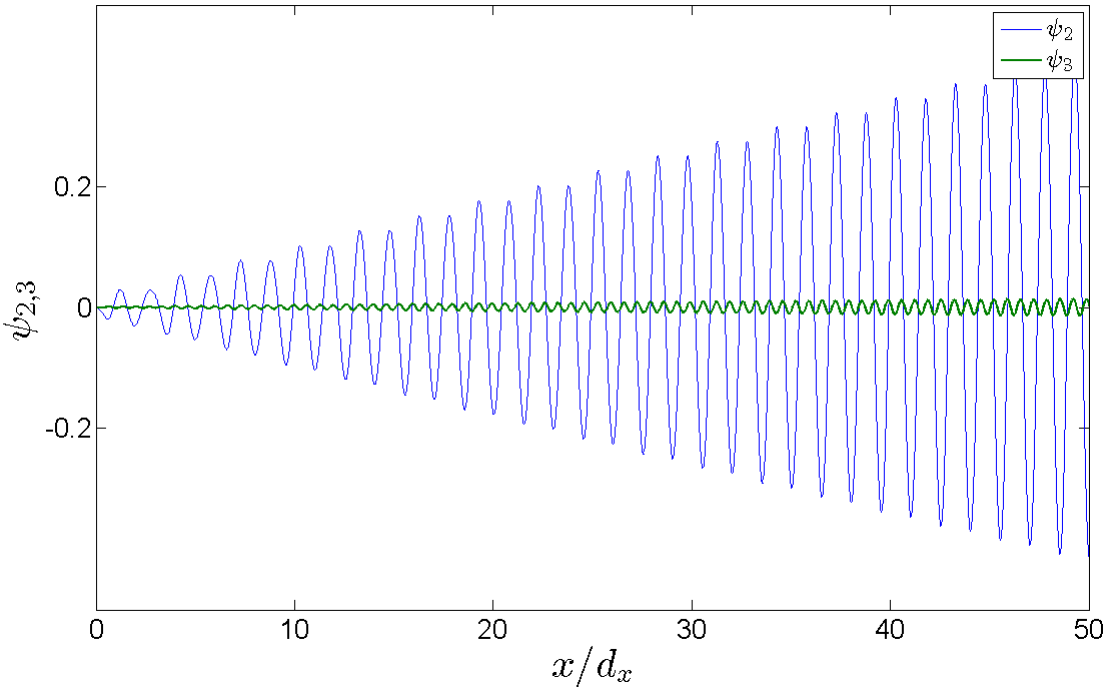

Figure 5.4: ψ_2 and ψ_3 as a function of x/d_x for $Q = 0.09$,at shared resonance $\omega = 3.50$ for the second and third harmonics. All other paramaters are the same as in Fig. 5.3.

Fig. 5.4 shows the harmonic amplitudes ψ_2 and ψ_3 as a function of propagation distance for a shared resonance for the second and third harmonics, showing that at resonance the third harmonic amplitude steadily increases but at a much slower rate than the second harmonic at resonance. In both cases the amplitudes reach a maximum value and display a long range oscillation as for the second harmonic amplitude in Chapter 4.

We can also see in Fig. 5.5 the case where ψ_3 grows beyond ψ_2. Since ψ_2 is not at resonance in this case its oscillations are disordered compared to ψ_3 , whereas ψ_3 grows steadily and displays a regular pattern of oscillation over a longer distance scale.

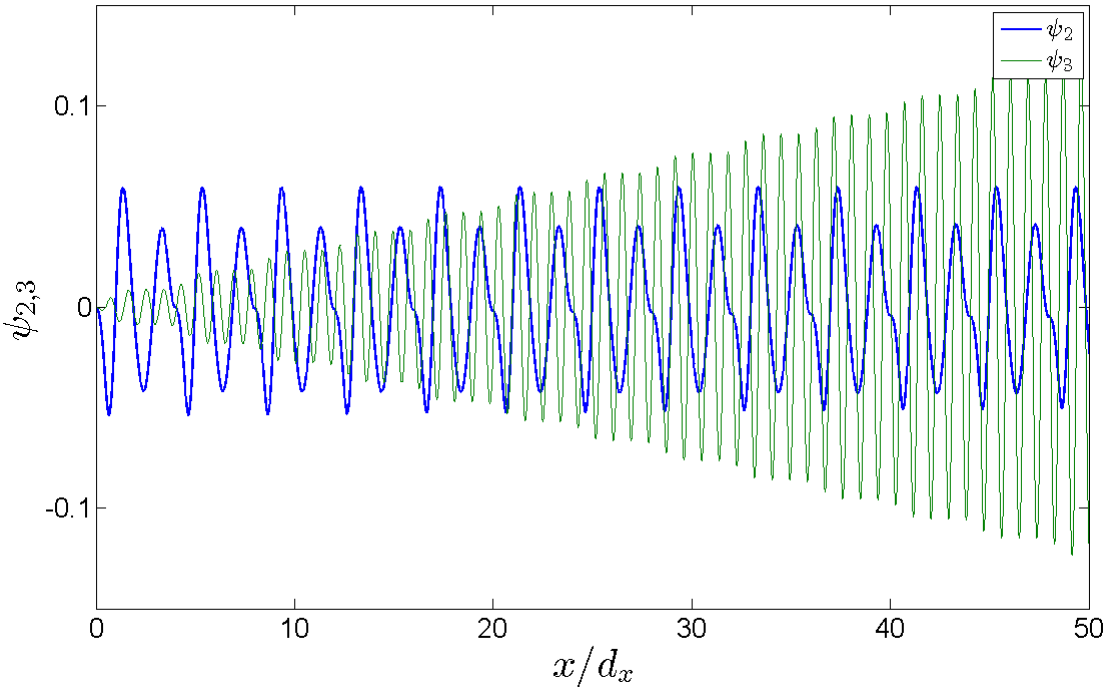

Figure 5.5: ψ_2 and ψ_3 as a function of x/d_x for $Q = 0.09$,at resonance $\omega = 2.62$ for the third harmonic. $l_0/d_x = 0.2$, $\psi_{2,3}(0) = \psi'_{2,3}(0) = 0$,$\psi_1(0) = 0.5$,$\psi'_1(0) = 0.2$,$d\tilde{x} = 0.001$.

The effect of varying the tuning parameter Q is also the same for both second and third harmonic resonances. Fig. 5.6 shows that increasing the component of the wavevector perpendicular to the superconducting layers also shifts the third harmonic resonances to lower frequency $\tilde{\omega}$. This indicates that third harmonic resonances can be controlled in the same manner as second harmonic resonances by varying the applied field as well as relative longitudinal and transverse wavevectors.

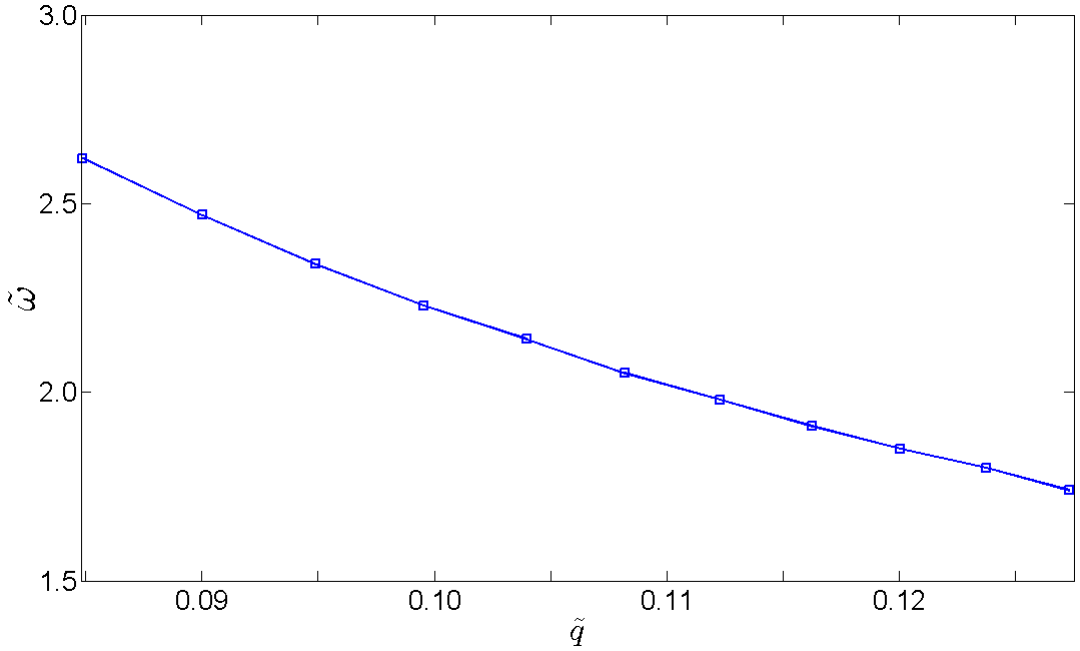

Figure 5.6: Dependence of the third harmonic resonance frequency from Fig. 4.8 at $\tilde{\omega} = 2.62$ on the normalised y-axis wavevector $\tilde{q}$. All other parameters are the same as in Fig. 5.3.

Third harmonic resonances can also exceed the amplitude of the second harmonic in certain cases

Chapter 6

Frequency mixing

Another well known nonlinear effect in photonic crystals described in Chapter 2 is sum and difference frequency generation [91]. The nonlinear mixing of two frequencies ω_1 and ω_2 in a material can produce harmonics with the sum $\omega_1 + \omega_2$ and difference $\omega_1 - \omega_2$ of the input frequencies. Due to the nonlinearity of the JV photonic crystal it should be possible to produce these sum and difference harmonics when two input frequencies are applied to the crystal. The sum and difference waves are produced as a result of the product of two harmonic waves with differing frequencies.

Sum and difference generation offers the possibility of shifting to both higher and lower frequencies than the plasma frequency in layered superconductors. We would expect a higher degree of control over the resonances produced, since we can vary the difference between the frequency inputs and the difference between the angle of incidence of each wave.

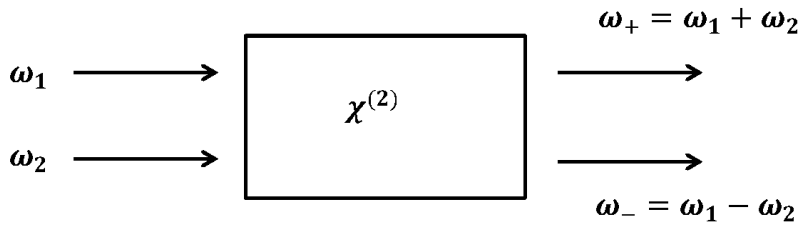

Figure 6.1: Schematic diagram of frequency mixing with two inputs to a nonlinear photonic crystal, the arrows on the left representing the inputs to the crystal at frequencies ω_1 and ω_2, while the arrows on the right represent the output harmonics ψ_+ and ψ_- generated within the crystal.

6.1 Deriving the sum-difference amplitude equations

Again the starting point is the coupled sine-Gordon equation:

$$\left[1 - \lambda_{ab}^2 \frac{\partial^2}{\partial y^2}\right] \left(\frac{1}{\omega_J^2}\frac{\partial^2 \varphi}{\partial t^2} + \sin\varphi\right) - \lambda_c^2 \frac{\partial^2 \varphi}{\partial x^2} = 0. \tag{6.1}$$

Here, we must use a solution (6.2) containing two frequency input waves as well as the sum and difference of two input frequencies ω_1 and ω_2. We consider the $\sin\varphi_0$ term expanded to second order as for the second harmonic case in Chapter 4.

$$\begin{aligned} \varphi_1 \;=\; & \psi_1(x)\cos(\omega_1 t - q_1 y) + \psi_2(x)\cos(\omega_2 t - q_2 y) + \\ & \psi_+(x)\cos((\omega_1+\omega_2)t - (q_1+q_2)y) + \\ & \psi_-(x)\cos((\omega_1-\omega_2)t - (q_1-q_2)y) \end{aligned} \tag{6.2}$$

Here ψ_+ is the amplitude of the sum harmonic with frequency $\omega_1 + \omega_2$ and ψ_- is the amplitude of the difference harmonic with frequency $\omega_1 - \omega_2$. q_1 and q_2 are the y-axis wavevectors for the two input THz waves respectively. We can substitute this solution to Eq. (6.1) and derive from this four coupled equations for the input harmonic amplitudes ψ_1 and ψ_2, as well as the sum and difference amplitudes ψ_+ and ψ_-. These equations are reached by ignoring higher harmonics and just keeping the sum and difference terms.

$$(\langle\cos\varphi_0\rangle - {\omega_1}^2)\psi_1 - \frac{\lambda_c^2}{(1+\lambda_{ab}^2 q_1^2)}\psi_1'' = \frac{\langle\sin\varphi_0\rangle}{2}(\psi_2\psi_- - \psi_2\psi_+) \tag{6.3}$$

$$(\langle\cos\varphi_0\rangle - {\omega_2}^2)\psi_2 - \frac{\lambda_c^2}{(1+4\lambda_{ab}^2 q_2^2)}\psi_2'' = \frac{\langle\sin\varphi_0\rangle}{2}(\psi_1\psi_- - \psi_1\psi_+) \tag{6.4}$$

$$(\langle\cos\varphi_0\rangle - (\omega_1+\omega_2)^2)\psi_+ - \frac{\lambda_c^2}{(1+\lambda_{ab}^2(q_1+q_2)^2)}\psi_+'' = \frac{\langle\sin\varphi_0\rangle}{2}\psi_1\psi_2 \tag{6.5}$$

$$(\langle\cos\varphi_0\rangle - (\omega_1-\omega_2)^2)\psi_- - \frac{\lambda_c^2}{(1+\lambda_{ab}^2(q_1-q_2)^2)}\psi_-'' = \frac{\langle\sin\varphi_0\rangle}{2}\psi_1\psi_2 \tag{6.6}$$

In the case of frequency mixing we have more potential ways of tuning the system since we can vary not only the frequencies ω_1 and ω_2 but the relative difference between the two. The same is true for the q_1 and q_2 which can be changed by varying the angle of the incident radiation of each input as well as the difference between them.

6.2 Numerical results

Again using a second order multiderivative method we can numerically analyze these equations and find the distribution of each harmonic in the JV photonic

crystal for a wide range of input parameters.

Although we have four coupled equations in this case, we can simplify things by making the assumption that $\psi_{+,-} \ll \psi_{1,2}$, i.e. the sum and difference amplitudes are much smaller than the two input amplitudes and ignoring feedback to ψ_1 and ψ_2 due to nonlinearity. This allows the nonlinear parts of (6.3) and (6.4) to be ignored, so they can be written in the homogeneous form (6.7).

$$(\langle \cos \varphi_0 \rangle - \tilde{\omega_{1,2}^2})\psi_{1,2} - \frac{\lambda_c^2}{(1 + \lambda_{ab}^2 q_{1,2}^2)}\psi_{1,2}^{''} = 0 \tag{6.7}$$

Again introducing new variables $P_{1,2,+,-} = \psi_{1,2,+,-}^{'}$ allows us to reduce the equations to first order. Now initial values of P and ψ at point x can be used to calculate subsequent values using the following Taylor expansions, for which the expressions for $P_{1,2,+,-}^{'}$ and $P_{1,2,+,-}^{''}$ are given in Appendix 2.

$$P_{1,2,+,-}(x + dx) = P_{1,2,+,-}(x) + P_{1,2,+,-}^{'} dx + P_{1,2,+,-}^{''} \frac{(dx)^2}{2}$$

$$\psi_{1,2,+,-}(x + dx) = \psi_{1,2,+,-}(x) + P_{1,2,+,-} dx + P_{1,2,+,-}^{'} \frac{(dx)^2}{2}$$

From these simulations using the method just described the spatial distribution of both ψ_+ and ψ_- can be plotted as a function of x, setting $\psi_+ = \psi_- = 0$ at $x = 0$. Again we are assuming that the sum and difference waves are produced within the crystal due to its nonlinearity. Fig. 6.2 shows the spatial distribution of the sum and difference frequency harmonics at a shared resonance for both amplitudes ψ_+ and ψ_-. Both amplitudes increase steadily with increased distance through the crystal, although it can be seen that the period of oscillation for ψ_- is larger than

for ψ_+.

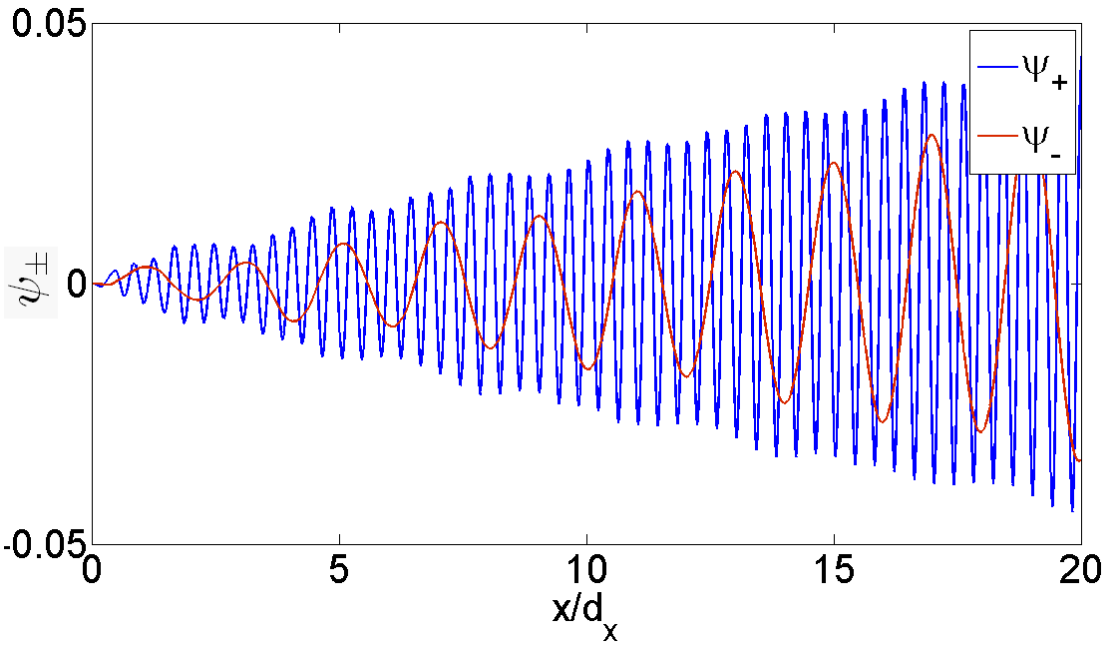

Figure 6.2: Spatial distribution for the sum and difference harmonic amplitudes $\psi_\pm(x)$ for $\tilde{q}_1 = 0.10, \tilde{q}_2 = 0.20$, $\omega_1 = 1.10,\ \omega_2 = 4.47$. Both the sum and difference amplitudes $\psi_\pm(x)$ increase at this resonance point with increasing distance of propagation through the JV photonic crystal. Taken from [102], with kind permission of the European Physical Journal (EPJ).

In Fig. 6.3 we can see the spatial distribution for both harmonics again for the case when we have a resonance of ψ_- only, whereas ψ_+ has a relatively small amplitude. It should be noted that the spatial period of the sum and difference waves can be altered by changing ω_1 and ω_2. This can be seen by comparing Fig. 6.2 with the inset of Fig. 6.3 where there is a larger difference between the wavelengths of sum and difference waves for a larger value of ω_2.

By fixing ω_1 constant and varying ω_2 (and hence varying the ratio ω_2/ω_1), the maximum value $\bar{\psi_\pm} = \max \psi_\pm$ can be plotted as a function of ω_2/ω_1. All amplitudes have been normalised by the amplitude of the largest peak and plotted on a log

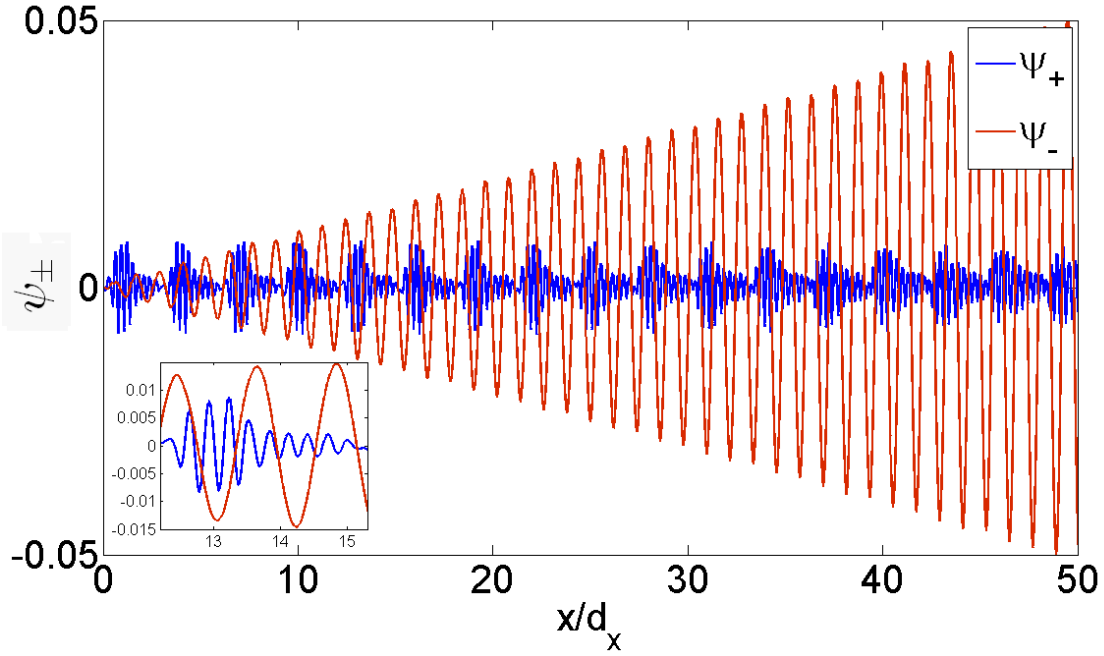

Figure 6.3: Spatial distribution for the sum and difference harmonic amplitudes $\psi_\pm(x)$ when $\tilde{q}_1 = 0.10, \tilde{q}_2 = 0.20$, $\omega_1 = 1.10$, $\omega_2 = 6.67$. Here the distribution of the sum and difference frequencies are plotted where there is a resonance of the difference frequency harmonic (red) but no resonance for the sum frequency harmonic (blue). The diagram inset shows the oscillation of ψ_+ for a smaller spatial interval. Taken from [102], with kind permission of the European Physical Journal (EPJ).

scale which gives much clearer comparison between peaks of different magnitude. All q values have been normalised by the characteristic value $q_{max} = 0.3\pi/s$, so we have a dimensionless y-axis wavevector $\tilde{q}_{1,2} = q_{1,2}/q_{max}$. The continuous limit of sine-Gordon equations used here requires that $\tilde{q} \ll 1$.

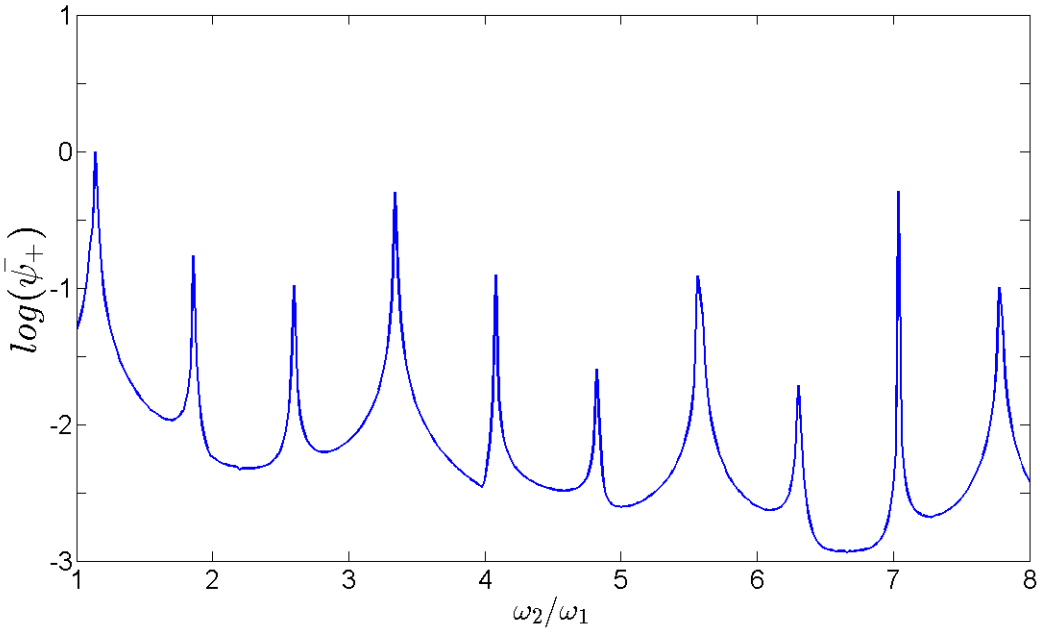

Figure 6.4: Resonances for the maximum sum harmonic amplitude $\bar{\psi}_+$ plotted on a log_{10} scale and normalised by the maximum resonance. $\tilde{q}_1 = \tilde{q}_2 = 0.15$, $\omega_1 = 1.10$. Resonances are roughly equally spaced but varying in amplitude. In this case $\bar{\psi}_- \ll \bar{\psi}_+$ for all values of ω_2 so there are no resonances for the difference amplitude $\bar{\psi}_-(\omega_2)$. The largest resonance for $\bar{\psi}_+(\omega_2)$ is at $\omega_2/\omega_1 = 1.14$.

We can see in Fig. 6.4 a large number of resonances when the ratio ω_2/ω_1 has certain values for which $\bar{\psi}_+$ increases by at least an order of magnitude, the largest resonance occurs at $\omega_2/\omega_1 = 1.14$. Fig. 6.5 displays the same results but for different values of $\tilde{q}_1$ and $\tilde{q}_2$, showing that the largest resonance in this case is at $\omega_2/\omega_1 = 3.11$. It's clear that the largest amplitude resonance can be shifted over a large frequency range by a small change in $\tilde{q}_1$ and $\tilde{q}_2$.

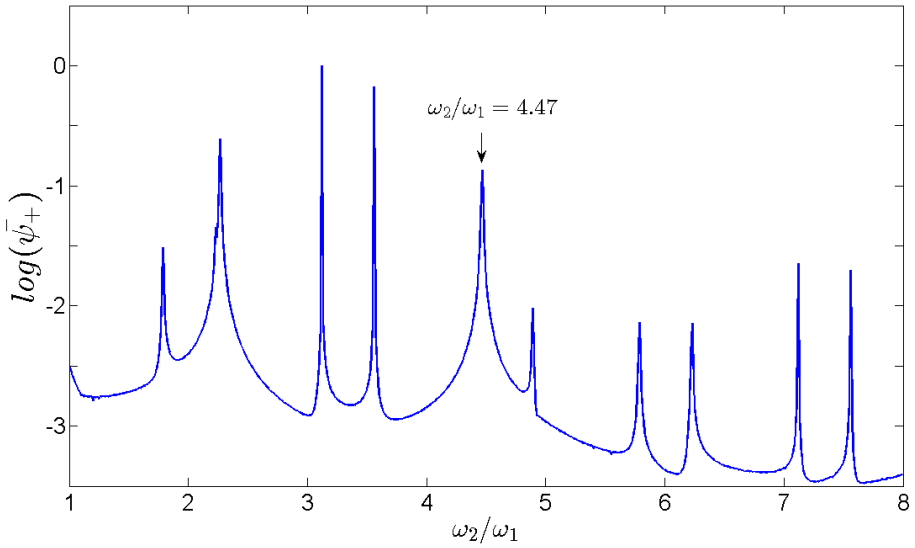

Figure 6.5: Resonances for sum harmonic amplitude $\bar{\psi}_+(\omega_2)$ plotted on a log scale when $\tilde{q}_1 = 0.10, \tilde{q}_2 = 0.20$, $\omega_1 = 1.10$. The resonance marked by the arrow at $\omega_2/\omega_1 = 4.47$ is shared by the difference amplitude $\bar{\psi}_-(\omega_2)$ (see Fig. 6.6), the largest resonance however is at $\omega_2/\omega_1 = 3.11$.

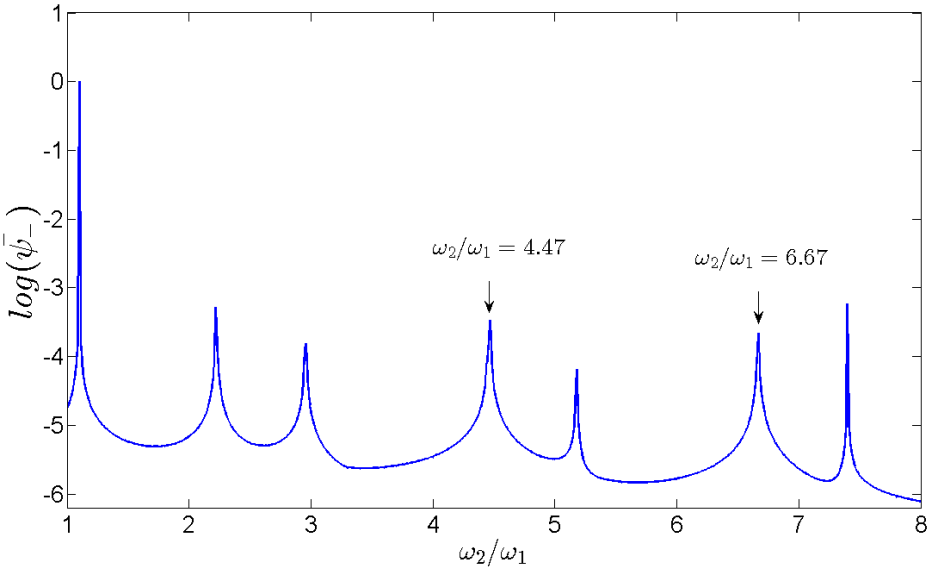

Figure 6.6: Resonances for the maximum difference harmonic amplitude $\bar{\psi}_-(\omega_2)$ plotted on a log_{10} scale when $\tilde{q}_1 = 0.10, \tilde{q}_2 = 0.20$, $\omega_1 = 1.10$. The resonance at $\omega_2/\omega_1 = 4.47$ is shared by the sum amplitude $\bar{\psi}_+(\omega_2)$ in Fig. 6.5.

Fig. 6.6 shows a series of resonances for $\bar{\psi}_-$ when this amplitude is strongly enhanced for specific values of ω_2/ω_1, in this case we have one large resonance at $\omega_2 \approx \omega_1$ and a series of smaller resonances for higher values of ω_2. The parameters used in this case are the same as Fig. 6.5. It can be seen that some of these resonances are shared by sum and difference harmonics as was shown in Fig. 6.2. Others are unique to either $\bar{\psi}_+$ or $\bar{\psi}_-$, as was the case for the spatial distribution plotted in Fig. 6.3 which corresponds to the marked resonance at $\omega_2/\omega_1 = 6.67$ in Fig. 6.6.

As with the second harmonic we can investigate the effect of changing $\tilde{q}_{1,2}$. When keeping the difference $(\tilde{q}_1 - \tilde{q}_2)$ fixed we can vary the sum $(\tilde{q}_1 + \tilde{q}_2)$ as shown in Fig. 6.7 for the same shared resonance of ψ_+ and ψ_- shown in both Fig. 6.5 and Fig. 6.6 for the ratio $\omega_2/\omega_1 = 4.47$. It can be seen in Fig. 6.7 that increasing the sum $(\tilde{q}_1 + \tilde{q}_2)$ lowers the frequency ω_2/ω_1 of this resonance.

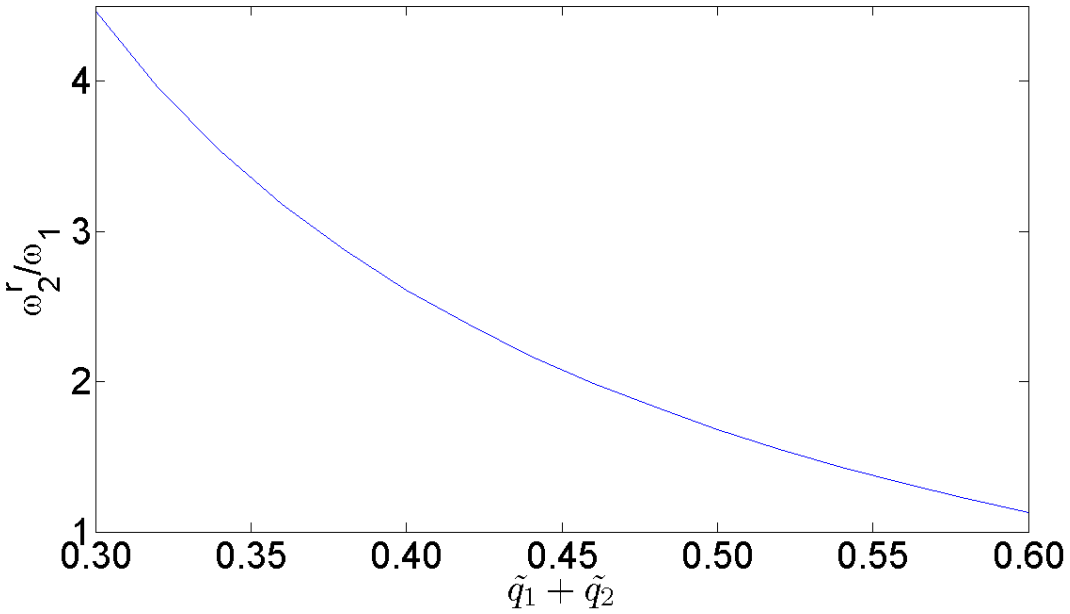

Figure 6.7: The dependence of the resonance frequency ω_2^r on the sum $(\tilde{q}_1 + \tilde{q}_2)$ of y-components of wave vectors of the input waves. All other parameters are kept constant: $\omega_1 = 1.10$, $(\tilde{q}_1 - \tilde{q}_2) = 0.1$. The resonance frequency ω_2^r decreasing with increasing $(\tilde{q}_1 + \tilde{q}_2)$ indicates the decay of resonance frequency when incident angles of input waves become simultaneously larger. Taken from [102], with kind permission of the European Physical Journal (EPJ).

Likewise we can fix the sum $(\tilde{q}_1 + \tilde{q}_2)$ and vary the difference $(\tilde{q}_1 - \tilde{q}_2)$ for the same resonance at $\omega_2/\omega_1 = 4.47$ which is shown in Fig. 6.8. Increasing the difference $(\tilde{q}_1 + \tilde{q}_2)$ moves the resonances to a higher value of ω_2/ω_1. It appears that the resonance frequency 'diverges' as $\tilde{q}_1$ gets close to zero.

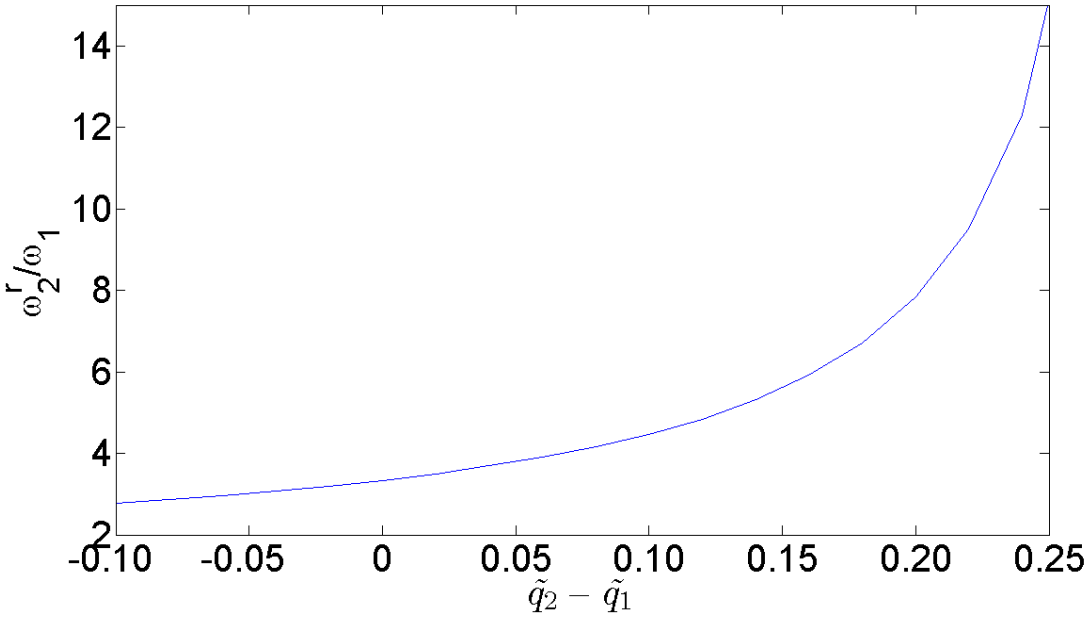

Figure 6.8: The dependence of the resonance frequency ω_2^r on the difference $(\tilde{q}_1 - \tilde{q}_2)$ of y-components of wave vectors of the input waves. All other parameters are kept constant: $\omega_1 = 1.10$, $(\tilde{q}_1 + \tilde{q}_2) = 0.3$. The resonance frequency ω_2^r growing with increasing $(\tilde{q}_1 - \tilde{q}_2)$ indicates the fast enhancement of resonance frequency with an increase of the relative angle between input waves. Taken from [102], with kind permission of the European Physical Journal (EPJ).

6.3 Origin of sum and difference resonances

As in Chapter 4 we can attempt to describe the resonances seen with an analytical approach similar to the one used there. We can consider weak input waves with small amplitudes $a \ll 1$. The right hand sides of Eq. (6.5) and Eq. (6.6) are proportional to $|\psi_1\psi_2| \propto a^2$. Since the nonlinear coupling in Eq. (6.3) and Eq. (6.4) is roughly $|\psi_{1,2}\psi_{+,-}| \propto a^3$, which is an order of magnitude smaller than $|\psi_+\psi_-| \propto a^2$.

Following this we can ignore the nonlinear coupling in Eq. (4.4) and Eq. (4.5) by only approximating to second order with respect to a, giving us two linear and two

nonlinear equations which are decoupled from each other.

$$(\langle\cos\varphi_0\rangle - {\omega_1}^2)\psi_1 - \frac{\lambda_c^2}{(1+\lambda_{ab}^2 q_1^2)}\psi_1'' = 0, \tag{6.8}$$

$$(\langle\cos\varphi_0\rangle - {\omega_2}^2)\psi_2 - \frac{\lambda_c^2}{(1+4\lambda_{ab}^2 q_2^2)}\psi_2'' = 0, \tag{6.9}$$

$$(\langle\cos\varphi_0\rangle - (\omega_1+\omega_2)^2)\psi_+ - \frac{\lambda_c^2}{(1+\lambda_{ab}^2(q_1+q_2)^2)}\psi_+'' = \frac{\langle\sin\varphi_0\rangle}{2}\psi_1\psi_2, \tag{6.10}$$

$$(\langle\cos\varphi_0\rangle - (\omega_1-\omega_2)^2)\psi_- - \frac{\lambda_c^2}{(1+\lambda_{ab}^2(q_1-q_2)^2)}\psi_-'' = \frac{\langle\sin\varphi_0\rangle}{2}\psi_1\psi_2. \tag{6.11}$$

The nonlinear right hand sides of Eq. (6.10) and Eq. (6.11) can be thought of as the driving 'forces' of the system induced by the inputs ψ_1 and ψ_2. The linear solutions here are denoted by ψ_{L1} and ψ_{L2}. The spectrum of these waves was already calculated in Chapter 4. It should be noted that here ψ_{L2} refers to the linear amplitude of the second input. This is in contrast to Chapter 4, where ψ_{L2} was the linear amplitude of the second harmonic.

$$(\langle\cos\varphi_0\rangle - (\omega_1+\omega_2)^2)\psi_{L+} - \frac{\lambda_c^2}{(1+\lambda_{ab}^2(q_1+q_2)^2)}\psi_{L+}'' = 0, \tag{6.12}$$

$$(\langle\cos\varphi_0\rangle - (\omega_1-\omega_2)^2)\psi_{L-} - \frac{\lambda_c^2}{(1+\lambda_{ab}^2(q_1-q_2)^2)}\psi_{L-}'' = 0. \tag{6.13}$$

Again separating the linear solutions $\psi_{L\pm}$ from the nonlinear amplitudes $A_\pm$ for sum and difference harmonics, we can write the solution as

$$\psi_\pm(x) = A_\pm(x)\psi_{L\pm}(x). \tag{6.14}$$

An equation can be derived for $P_{\pm} = A_{\pm}^{'}$, reducing the equation to a first order differential equation with variable coefficients:

$$P_{\pm}^{'}\psi L\pm + 2P_{\pm}\psi_{L\pm} = F_{\pm}, \tag{6.15}$$

where the driving 'force' $F_{\pm}$ is given by

$$F_{\pm} = -\frac{(q_1+q_2)^2}{2\gamma^2}\langle \sin\varphi_0\rangle \psi_{L1}\psi_{L2}.$$

The complementary function for Eq. (6.15) can be given by

$$P = \frac{C_{\pm}}{\psi_{L\pm}^2},$$

so using the method of variational constants [100], introducing an x dependence in the constant C, we can solve Eq. (6.15) using a substitution of the form Eq. (6.16):

$$P = \frac{C_{\pm}(x)}{\psi_{L\pm}^2}. \tag{6.16}$$

This gives an expression for $C_{\pm}$ which can be written as:

$$C^{'} = F_{\pm}\psi_{L\pm}. \tag{6.17}$$

Now we apply the usual boundary condition that $C_{\pm}(x=0) = 0$ so the electric and magnetic fields of the sum and difference harmonics are zero at the surface of the crystal. Integrating Eq. (6.17), also making use of Eq. (6.16) we can derive:

$$P_{\pm}(x) = \frac{1}{\psi_{L\pm}^2(x)} \int_0^x d\tilde{x} F_{\pm}(\tilde{x}) \psi_{L\pm}(\tilde{x}).$$

Now also using Eq. (6.14), we can derive a final expression for $\psi_{\pm}(x)$

$$\psi_{\pm}(x) = \psi_{L\pm}(x) \int_0^x \frac{d\tilde{x}}{\psi_{L\pm}^2(\tilde{x})} \int_0^{\tilde{x}} d\tilde{\tilde{x}} F_{\pm}(\tilde{\tilde{x}}) \psi_{L\pm}(\tilde{\tilde{x}}). \tag{6.18}$$

It can be concluded from this analysis that resonances for the sum and difference amplitudes are displayed at the maximum value of the integral of $F_{\pm}\psi_{L\pm}$. This condition occurs when both $F_{\pm}$ and $\psi_{L\pm}$ have the same spatial period, leading to constructive interference and a larger overall amplitude. Knowing the linear solutions ψ_{L1}, ψ_{L2} and $\psi_{L\pm}$ allows the solutions for $\psi_{\pm}$ to be calculated using a step approximation for both $\langle \cos \varphi_0 \rangle$ and $\langle \sin \varphi_0 \rangle$.

Chapter 7

Conclusions

7.1 Summary

The work studied in this thesis on the second harmonic, third harmonic and harmonic mixing all shows that the Josephson-vortex photonic crystal can be potentially very useful as a nonlinear THz device and can increase the frequency range reachable by tuneable THz frequency emitters, detectors and filters. The frequency ranges of the crystal can be readily tuned by varying the applied magnetic field and by adjusting the orientation of the layered superconductor with respect to the incoming THz waves.

The equations derived here for these nonlinear cases take the form of a Schrödinger equation for THz waves with an effective mass in the JV photonic crystal and moving under the 'potential' of the Josephson vortices. This helps illustrate how nonlinear waves can have particle like behaviour. It should be stated that the vortices in the JV photonic crystal allow much more efficient control of THz waves due to nonlinearity. Layered superconductors with no applied magnetic field and

hence no vortices will have an odd-like nonlinearity which will not allow for second harmonic generation (or any other even harmonic). The frequency mixing process in Chapter 6 is also based on the second order nonlinearity of the JV photonic crystal.

With a single frequency input to the JV photonic crystal, we can see resonances for the second and third harmonic amplitudes which are enhanced by several orders of magnitude for these input frequencies. The second harmonic resonance frequencies are also shared with the third harmonic, although the third harmonic amplitudes in this case are several orders of magnitude smaller. The third harmonic also displays extra resonances during which the third harmonic amplitude can exceed that of the second harmonic by an order of magnitude.

When inputting two discrete frequencies ω_1 and ω_2 to the JV photonic crystal we can see resonances again for specific values of the ratio ω_2/ω_1. The sum and difference resonances displayed in Chapter 6 show that the JV photonic crystal can give a high degree of control over the frequencies of JPWs produced within it when a two frequency THz input is allowed to propagate.

For both the second harmonic and frequency mixing harmonics, the resonances can be described by the resonance condition where the driving radiation has the same period as the linear oscillations in the crystal. For the second harmonic we see resonances where the condition $k_2 = 2k_1$ is met for wavevectors k_1 and k_2 for the first and second harmonic respectively. The second harmonic resonance approximation well matches the nonlinear increase of the second harmonic amplitude close to resonance.

The equations used in this thesis neglect damping of JPWs which is valid only for samples thinner than around 0.3mm (the skin depth), within which damping can be

considered negligible at low enough temperatures. We also neglect the capacitive coupling between the superconducting layers which for layered superconductors has shown to be much weaker than the inductive coupling considered here.

The theoretical work presented in this thesis could have a practical application in helping to bridge the THz gap with compact and controllable devices since the JV photonic crystal offers a high level of control over THz waves. This could have application in compact and readily tunable THz filters and THz waveguides. The work on second harmonic generation in the JV photonic crystal has been published in the Physical Review B [101] and was presented at CMMP 2012 (Condensed Matter and Materials Physics conference), in Edinburgh. A paper on frequency mixing has been accepted for publication in the European Physical Journal B [102].

7.2 Further research

There is much potential for further research in the area of nonlinearity in the Josephson-vortex photonic crystal. It would be interesting to study the effect of the motion of the Josephson-vortex lattice on the harmonic generation discussed in this thesis, which can be achieved by applying a c-axis current perpendicular to the layers.

It has been noticed that there is a region of negative refractive index for THz waves in layered superconductors. It would be interesting to look into how the presence of vortices with an applied magnetic field would effect this region. This could have applications as a superlens for THz waves which would not be subject to the diffraction limit.

Chapter 8

Bibliography

[1] M. Tonouchi, 'Cutting-edge terahertz technology', Nature Photonics **1**, 97 (2007).

[2] B. Ferguson and X. C. Zhang, 'Materials for terahertz science and technology', Nat. Mater. **1** 26-33 (2006).

[3] X.C Zhang, Jingzhou Xu, 'Introduction to THz wave photonics', Springer Science (2010).

[4] A. Dobroiu, C. Otani, K. Kawase, 'Terahertz-wave sources and imaging applications', Measurement Science and Technology **17**, R161 (2006).

[5] J. Faist et al., 'Terahertz quantum cascade lasers', Phil. Trans. R. Soc. Lond. A vol. 362 no. 1815 215-231 (2004).

[6] M.Asada, S. Suzuki, N. Kishimoto, 'Resonant tunnelling diodes for Sub-Terahertz and Terahertz Oscillators' , Jpn. J. Appl. Phys. **47** pp. 4375-4384 (2008).

[7] N.Orihashi, S. Suzuki, M. Asada, 'One THz harmonic oscillation of resonant tunneling diodes', Appl. Phys. Lett. **87** 233501 (2005).

[8] T. Otsuji, M. Hanabe, T. A. Nishimura, 'Granting-bicoupled plasma-wave photomixer resonant-cavity enhanced structure', Opt. Express **14** 4815-4825 (2006).

[9] N. Sekine, K. Hirakawa, 'Dispersive terahertz gain of a nonclassical oscillator: Bloch oscillation in semiconductor superlattices', Phys. Rev. Lett. **94** 057408 (2005).

[10] M. Tani, K. Lee, and X.-C. Zhang, 'Detection of terahertz radiation with low-temperature-grown GaAs-based photoconductive antenna using 1.55 μm probe', Appl. Phys. Lett. **77**, 1396 (2000).

[11] G. Gallot and D. Grischkowsky, 'Electro-optic detection of terahertz radiation', J. Opt. Soc. Am. B, Vol 16, No. 8 (1999).

[12] C. Kubler, R. Huber and A. Leitenstorfer, 'Ultrabroadband terahertz pulses : generation and field-resolved detection', Semicond. Sci. Technol. **20** S128-S133 (2005).

[13] Yun-Shik Lee, 'Principles of Terahertz Science and Technology', Springer Science (2009).

[14] A.J.Miller, A. Luukanen, E. N. Grossman, 'Micromachined antenna-coupled uncooled microbolometers for terahertz imaging arrays', Proc. SPIE **5411** 8-24 (2004).

[15] T. Fuse et al., 'Coulomb peak shifts under terahertz-wave irradiation in carbon nanotube single-electron transistors', Appl. Phys. Lett. **90**, 013119 (2007).

[16] G. Gallot, S. P. Jamison, R. W. McGowan and D. Grisch-kowsky, 'Terahertz waveguides', J. Opt. Soc. Am. B **17**, 851-863 (2000).

[17] R. Mendis and D. Grischkowsky, 'Plastic ribbon THz waveguides', J. Appl. Phys. **88**, 4449-4451 (2000).

[18] V. P. Koshelets, S.V.Shitov, 'Integrated superconducting recievers', Supercond. Sci. Technol. **13**, R53 (2000).

[19] S. Savel'ev, V. A. Yampol'skii, A. L. Rakhmanov and F. Nori, 'Terahertz Josephson plasma waves in layered superconductors: spectrum, generation, nonlinear and quantum phenomena', Rep. Prog. Phys. **73** 026501 (2010).

[20] H. B Wang et al., 'Terahertz ocsillation in submicron sized intrinsic Josephson junctions', Appl. Phys. Lett. **89**, 252506 (2006).

[21] S. Savel'ev, A. L. Rakhmanov, F. Nori, 'Using Josephson vortex lattices to control terahertz radiation: Tunable transparency and terahertz photonic crystals', Phys. Rev. Lett. **94**, 157004 (2005).

[22] B.D Josephson, 'Possible new effects in superconductive tunnelling' Phys. Lett. **1** 251 (1962).

[23] B.D Josephson, 'Coupled superconductors' Rev. Mod. Phys. **36** 216 (1964).

[24] David J. Griffiths, 'Introduction to electrodynamics',San Francisco : Pearson/Benjamin Cummings 3rd ed. (2008).

[25] S. N. Artemenko and S.V. Remizov, Physica C (Amsterdam) 362, 200 (2001).

[26] J. D. Joannopoulos, R. D. Meade and J. N. Winn, 'Photonic Crystals: Molding the Flow of Light', Princeton University Press, 2nd ed.(2008).

[27] S. Savel'ev, A.L. Rakhmanov, F. Nori, 'Josephson vortex lattices as scatterers of terahertz radiation: Giant magneto-optical effect and Doppler effect using terahertz tunable photonic crystals', Phys. Rev. B **74**, 184512 (2006).

[28] Xiao Hu and Shi-Zeng Lin, 'Phase dynamics in a stack of inductively coupled intrinsic Josephson junctions and terahertz electromagnetic radiation', Supercond. Sci. Technol. **23** 053001 (2010).

[29] M. Tinkham, 'Introduction to superconductivity', Dover, 2nd ed. (1996).

[30] B.D Josephson, 'Supercurrents through barriers' Adv. Phys. **14** 419 (1965).

[31] P. Muller, A. V. Ustinov, 'The Physics of superconductors : Introduction to fundamentals and applications', Springer (1997).

[32] A. A. Abrikosov, 'The magnetic properties of superconducting alloys', J. Phys. Chem. Solids 2(3) 199-208 (1957).

[33] G. Blatter et al., 'Vortices in high-temperature superconductors', Rev. Mod. Phys. **66** 1125-1388 (1994).

[34] Y. Matsuda et al., 'Excitation of Josephson plasma and vortex oscillation modes in $Bi_2Sr_2CaCu_2O_8$ in parallel magnetic fields', Phys. Rev. B **55**, R8685 (1997).

[35] D. G. Swanson, 'Plasma waves', Institute of Physics publishing, 2nd ed. (2003).

[36] S. Shapiro, 'Josephson currents in superconducting tunneling: the effect of microwaves and other observations', Phys. Rev. Lett. **11** 80 (1963).

[37] S. Shapiro, S. Holly and A. R. Janus, 'Effect of microwaves on Josephson currents in superconducting tunneling', Rev. Mod. Phys. **36** 223 (1964)

[38] R. L. Kautz, 'Noise, chaos, and the Josephson voltage standard', Rep. Prog. Phys. **59** 935-92 (1996).

[39] H. B. Wang et al., 'Observation of Shapiro steps and spectroscopic applications of stacked intrinsic Josephson junctions up to the terahertz region', Supercond. Sci. Technol. **15** 90-93 (2002).

[40] A. Barone and G. Paterno, 'Physics and Applications of the Josephson Effect', New York : Wiley (1982).

[41] J. G. Bednorz and K. A. Müller , 'Possible high-Tc superconductivity in the Ba-La-Cu-O system', Z. Phys. B **64** 189-93 (1986).

[42] R. Kleiner, F. Steinmeyer, G Kunkel and P Müller, 'Intrinsic Josephson effects in $Bi_2Sr_2CaCu_2O_8$ single-crystals', Phys. Rev. Lett. **68** 2394-7 (1992).

[43] R. Kleiner and P. Müller, 'Intrinsic Josephson effects in high-Tc superconductors', Phys. Rev. B **49** 1327-41 (1994).

[44] I. E. Batov et al., 'Detection of 0.5 THz radiation from intrinsic $Bi_2Sr_2CaCu_2O_8$ Josephson junctions', Appl. Phys. Lett. **88** 262504 (1994).

[45] L. Ozyuzer et al., 'Emission of coherent THz radiation from superconductors', Science **318** 1291-3 (2007).

[46] M. Tsujimoto et at., 'Terahertz imaging system using high-T_c superconducting oscillation devices', J. Appl. phys. **111** 123111 (2012).

[47] K. Delfanazari et al., 'Tunable terahertz emission from intrinsic Josephson junctions in acute isoceles triangular $Bi_2Sr_2CaCu_2O_{8+\delta}$ mesas' Opt. Express, vol.21, issue 2, pp. 2171-2184 (2013).

[48] H. Susanto, E. Goldobin et al., 'Controllable plasma energy bands in a one-dimensional crystal of fractional Josephson vortices', Phys. Rev. B **71**, 174510 (2005).

[49] S. Savel'ev, V. Yampol'skii, F. Nori, 'Surface Josephson plasma waves in layered superconductors', Phys. Rev. Lett. **95** 187002 (2005).

[50] S. Savel'ev, V. Yampol'skii, A. L. Rakhmanov, F. Nori, 'Layered superconductors as nonlinear waveguides for terahertz waves', Phys. Rev. B **75** 184503 (2007).

[51] S. Savel'ev, A. L. Rakhmanov, V. Yampol'skii, F. Nori, 'Analogues of nonlinear optics using terahertz Josephson plasma waves in layered superconductors', Nature Physics **2**, 521-525 (2006).

[52] V. A. Yampol'skii et al., 'Nonlinear Josephson plasma waves in slabs of layered superconductors', Physica C, **468**, 499-502 (2008).

[53] N. Engheta, R. W. Ziolkowski, 'Metamaterials : Physics and engineering explorations', Wiley and sons (2006).

[54] V. A. Golick et al., 'Surface Josephson plasma waves in layered superconductors above the plasma frequency : Evidence for a negative index of refraction', Phys. Rev. Lett. **104** 187003 (2010).

[55] A. L. Rakhmanov et al., 'Layered superconductors as negative-refractive-index metamaterials' Phys. Rev. B **81** 075101 (2010).

[56] Rudolf Uitham, 'Electromagnetic pulse propagation in one-dimensional photonic crystals', Zernike Institute Ph.D. thesis series 2008-23 (2008).

[57] K. Sakoda, 'Optical Properties of Photonic Crystals', Springer: New York (2001).

[58] C. Kittel, 'Introduction to Solid State Physics', Wiley, 7th ed. (1995).

[59] A. Goswami, 'Quantum Mechanics'. Wm. C. Brown Publishers, 2nd ed., (1997).

[60] M Bertolotti, 'Wave interactions in photonic band structures: an overview' , J. Opt. A: Pure Appl. Opt. **8** S9-S32 (2006).

[61] E. R. Brown and O. B. McMahon, 'Large electromagnetic stop bands in metallodielectric photonic crystals', Appl. Phys. Lett. **67** no. 15, 2138-2140 (1995).

[62] A. Banerjee, 'Optical filtering characteristics of 1D photonic crystals', Lambert academic publishing (2012).

[63] R. D. Meade, A. Devenyi, J. D. Joannopoulos, O. L. Alerhand, D. A. Smith and K. Kash, 'Novel applications of photonic band gap materials: low-loss bends and high-Q cavities', J. Appl. Phys. **75** 4753 (1994).

[64] M. Loncar, J. Vuckovic and A. Scherer, 'Methods for controlling positions of guided modes of photonic crystal waveguides', J. Opt. Soc. Amer. B. Opt. Phys. **18** 1362-1368 (2001).

[65]] H. O. Benisty et al., 'Models and measurements for the transmission of submicron-width waveguide bends defined in two-dimensional photonic crystals', IEEE J. Quantum Electron. **38**,no. 7, 770-785 (2002).

[66] A. Chutinan, M. Okano and S. Noda, 'Wider bandwidth with high transmission through waveguide bends in two-dimensional photonic crystal slabs', Appl. Phys. Lett. **80** 1698-1700 (2002).

[67] E. Yablonovitch and T. J. Gmitter, 'Donor and acceptor modes in photonic band structures', Phys. Rev. Lett. **67** 3380-3383 (1991)

[68] P. T. Lee, T. W. Lu, J. H. Fan and F. M. Tsai, 'High quality factor microcavity lasers realized by circular photonic crystal with isotropic photonic band gap effect', Appl. Phys. Lett. **90** 151125 (2007).

[69] T. Yoshie, J. Vuckovic and A. Scherer, 'High quality two-dimensional photonic crystal slab cavities', Appl. Phys. Lett. **79** 4289-4291 (2001).

[70] P. Lalanne and J. P. Hugonin, 'Bloch-wave engineering for high-q small-v microcavities', IEEE. J. Quantum Electron. **39**, no. 11, 1430-1438 (2003).

[71] P. Lalanne, S. Mias and J. P. Hugonin, 'Two physical mechanisms for boosting the quality factor to cavity volume ratio of photonic crystal microcavities', Opt. Exp. **12** 458-467 (2004)

[72]] R. K. Lee, O. J. Painter, D. D'Urso, A. Scherer and A. Yariv, 'Measurement of spontaneous emission from a two-dimensional photonic band gap defined microcavity at near-infrared wavelengths', Appl. Phys. Lett. **74** 1522-1524 (1999)

[73] M. Bayindir, B. Temelkuran and E. Ozbay, 'Photonic crystal based beam splitters', Appl. Phys. Lett. **77** 3902-3904 (2000)

[74] M. Qiu et al., 'Photonic crystal optical filter based on contra-directional coupling', Appl. Phys. Lett. **83** 5121-5123 (2003)

[75] E. A. Camargo, H. M. H. Chong and R. M. Rue, '2D photonic crystal thermo-optic switch based on AlGaAs/GaAs epitaxal structure', Opt. Exp. **12** 1048-1059 (2004).

[76] A. Sharkawy, S. Shouyuan, D. W. Prather and R. A. Soref, 'Electro-optical switching using coupled photonic crystal waveguides', Opt. Exp. **10**, 1048-1052 (2002).

[77] S. Fan, S. G. Johnson and J. D. Joannopoulos, 'Waveguide branches in photonic crystals', J. Opt. Soc. Amer. B **18**, 162-165 (2001).

[78] M. F. Yanik, S. Fan, M. Soljacic and J. D. Joannopoulos, 'All-optical transistor action with bistable switching in a photonic crystal cross-waveguide geometry', Opt. Lett. **28**, 2506 (2003).

[79] J. S. Shirk et al., 'Nonlinear nanolayered polymers : 1D photonic materials with applications to optical limiting', Tech. Dig. Conf. Lasers and Electro-Optics 83-84 (2001)

[80] H. B. Lin, R. J. Tonucci and A. J. Campillo, 'Two-dimensional photonic band gap optical limiter in the visible', Opt. Lett. **23** 94-96 (1998)

[81] A. M. Zheltikov, N. I. Koroteev, S. A. Magnitsky and A. V. Tarasishin, 'Self-phase modulation and compression of short laser pulses in a non-linear photonic crystal', Izvestiya Akademii Nauk Seriya Fizicheskaya **63** 717-724 (1999).

[82] I. Abdulhalim, 'Reflective phase-only modulation using one-dimensional photonic crystals', J. Opt. A. Pure Appl. Opt. **2** L9-L11 (2000).

[83] K. G. Hougaard, J. Broeng and A. Bjarklev, 'Low pump power photonic crystal fibre amplifiers', Electron. Lett. **39**, no. 7, 599-600 (2003).

[84] T. V. Andersen, S. R. Thogersen, S. R. Keiding and J. J. Larsen, 'High-power intracavity frequency doubling of a Ti:sapphire femtosecond oscillator, Appl. Phys. B. Lasers Opt. **76** 639-644 (2003).

[85] S. Lan et al., 'Similar role of waveguide bends in photonic crystal circuits and disordered defects in coupled cavity waveguides: an intrinsic problem in realizing photonic crystal circuits', Phys. Rev. B **67** 115208 (2003).

[86] S. Noda, A. Chutinan and M. Imada, 'Trapping and emission of photons by a single defect in a photonic band gap structure', Nature **407** 608-610 (2000).

[87] Y. Ohtera et al., 'Photonic crystal polarisation splitters', Electron. Lett. **35**, no. 15, 1271-1272 (1999).

[88] S. Lin et al., 'Low-loss wide-angle Y splitter at similar to 1.6-μm wavelengths built with a two-dimensional photonic crystal', Opt. Lett. **27** 1400-1402 (2002).

[89] R. Wison, T. J. Karle, I. Moerman and T. F. Krauss, 'Efficient photonic crystal Y-junctions', J. Opt. A **5** S76-S80 (2003).

[90] M. H. Shih et al., 'Two-dimensional photonic crystal Mach-Zehnder interferometers', Appl. Phys. Lett. **84** 460-462 (2004).

[91] Robert W.Boyd., 'Nonlinear optics', Academic press ISBN 0-12-121682-9 (2003).

[92] P. A. Franken et al.,'Generation of optical harmonics',Phys. Rev. Lett. **7** 118 (1961).

[93] E.A Ostrovskaya, Y.S Kivshar, 'Photonic crystals for matter waves: Bose-Einstein condensates in optical lattices', Opt. Exp. **12**(1) (2004).

[94] L. de Broglie, Ann. Phys. (Paris) **3** , 22 (1925).

[95] Yu. S. Kivshar and G. P. Agrawal, 'Optical Solitons: From Fibers to Photonic Crystals' , Academic Press, San Diego (2003).

[96] H. Matsumoto and T. Koyama, 'Josephson plasma and Josephson vortex lattice in high T_c superconductors with an applied magnetic field parallel to the layers' Physica C, 412-414, 444-448 (2004).

[97] V. G. Kogan, 'London approach to anisotropic type-II superconductors', Phys. Rev. B, **24** 1572-1575 (1981).

[98] S. Rother et al., 'Charge-imbalance effects in intrinsic Josephson systems', Phys. Rev. B **67** 024510 (2003).

[99] A.Gurevich, 'Nonlocal Josephson electrodynamis and pinning in superconductors', Phys. Rev. B **46** 5 (1992).

[100] K. F. Riley, M. P. Hobson, S. J. Bence, 'Mathematical methods for Physics and Engineering', Cambridge University press, 3rd ed. (2006).

[101] A. Wall-Clarke, S. Savel'ev, 'Nonlinear effects in the Josephson-vortex terahertz photonic crystal : Second harmonic generation', Phys. Rev. B **85** 214521 (2012);

[102] A. Wall-Clarke, S. Savel'ev, 'Nonlinear effects in the Josephson-vortex terahertz photonic crystal : Frequency mixing, Eur. Phys. J. B **86** 205 (2013);

Chapter 9

Appendix 1: Second harmonic resonance approximation integrals

Multiplying Eq. (4.30) by Ψ'_{L1} and Eq. (4.31) by Ψ'_{L2} and averaging over one unit cell L of the Josephson-vortex THz photonic crystal, we can derive Eq. (9.1) and Eq. (9.2)

$$\begin{aligned}\left(Y_{1,1}\cos^2 k_1 x - 2Y_{1,2}\cos k_1 x \sin k_1 x + Y_{1,3}\sin^2 k_1 x\right) A'_1 \\ = -\frac{q^2}{2\gamma^2} A_1 A_2 \Big(Z_{1,1}\cos^2 k_1 x \cos k_2 x \\ -Z_{1,2}\cos k_1 x \sin k_1 x \cos k_2 x + Z_{1,3}\sin^2 k_1 x \cos k_2 x \\ -Z_{1,4}\cos^2 k_1 x \sin k_2 x + Z_{1,5}\sin k_1 x \cos k_1 x \sin k_2 x \\ -Z_{1,6}\sin^2 k_1 x \sin k_2 x \Big),\end{aligned} \tag{9.1}$$

$$\begin{aligned}\left(Y_{2,1}\cos^2 k_2x - 2Y_{2,2}\cos k_2x\sin k_2x + Y_{2,3}\sin^2 k_2x\right)A_1' \\ = -\frac{q^2}{\gamma^2}A_1^2\Big(Z_{2,1}\cos^2 k_1x\cos k_2x \\ -Z_{2,2}\cos k_1x\sin k_1x\cos k_2x + Z_{2,3}\sin^2 k_1x\cos k_2x \\ -Z_{2,4}\cos^2 k_1x\sin k_2x + Z_{2,5}\cos k_1x\sin k_1x\sin k_2x \\ -Z_{2,6}\sin^2 k_1x\sin k_2x\Big),\end{aligned} \tag{9.2}$$

where the coefficients are given by the following integrals

$$Y_{j,1} = \frac{1}{L}\int_0^L (u_j' - v_jk_j)^2dx,$$

$$Y_{j,2} = \frac{1}{L}\int_0^L (u_j' - v_jk_j)(v_j' + k_ju_j)dx,$$

$$Y_{j,3} = \frac{1}{L}\int_0^L (v_j' + k_ju_j)^2dx,$$

$$Z_{1,1} = \frac{1}{L}\int_0^L \langle\sin\varphi_0\rangle(u_1' - v_1k_1)u_1u_2dx,$$

$$Z_{1,2} = \frac{1}{L}\int_0^L \langle\sin\varphi_0\rangle[(u_1' - k_1v_1)v_1u_2 + (v_1' + k_1u_1)u_1u_2]dx,$$

$$Z_{1,3} = \frac{1}{L}\int_0^L \langle\sin\varphi_0\rangle(v_1' + k_1u_1)v_1u_2dx,$$

$$Z_{1,4} = \frac{1}{L}\int_0^L \langle\sin\varphi_0\rangle(u_1' - k_1v_1)u_1v_2dx,$$

$$Z_{1,5} = \frac{1}{L}\int_0^L \langle\sin\varphi_0\rangle[(u_1' - k_1v_1)v_1v_2 + (v_1' + k_1u_1)u_1v_2]dx,$$

$$Z_{1,6} = \frac{1}{L}\int_0^L \langle\sin\varphi_0\rangle(v_1' + k_1u_1)v_1v_2dx,$$

$$Z_{2,1} = \frac{1}{L}\int_0^L \langle \sin\varphi_0\rangle (u_2' - v_2 k_2) u_1^2 dx,$$

$$Z_{2,2} = \frac{2}{L}\int_0^L \langle \sin\varphi_0\rangle (u_2' - k_2 v_2) u_1 v_1] dx,$$

$$Z_{2,3} = \frac{1}{L}\int_0^L \langle \sin\varphi_0\rangle (u_2' - k_2 v_2) v_1^2 dx,$$

$$Z_{2,4} = \frac{1}{L}\int_0^L \langle \sin\varphi_0\rangle (v_2' + k_2 u_2) u_1^2 dx,$$

$$Z_{2,5} = \frac{2}{L}\int_0^L \langle \sin\varphi_0\rangle (v_2' + k_2 u_2) v_1 u_1 dx,$$

$$Z_{2,6} = \frac{1}{L}\int_0^L \langle \sin\varphi_0\rangle (v_2' + k_2 u_2) v_1^2 dx.$$

Now we can assume that the amplitudes A_1 and A_2 vary slowly also on scales of the order of the wave length of the first and the second harmonics, thus we can also average the derived equations on the scale of $\mathcal{L} > \max(2\pi/k_1, 2\pi/k_2)$. Due to fast oscillations of $\cos k_{1,2}x$ and $\sin k_{1,2}x$, this averaging results in trivial equations $A_1' = A_3' = 0$ for all k_1 and k_2 apart of resonance points $k_2 = 2k_1$ where the coupling of the first and the second harmonics are most efficient. At the resonance point $k_2 = 2k_1$ we obtain:

$$\left(\frac{Y_{1,1}}{2} + \frac{Y_{1,3}}{2}\right) A_1' = -\frac{q^2}{2\gamma^2} A_1 A_2 \left(\frac{Z_{1,1}}{4} - \frac{Z_{1,3}}{4} + \frac{Z_{1,5}}{4}\right), \tag{9.3}$$

$$\left(\frac{Y_{2,1}}{2} + \frac{Y_{2,3}}{2}\right) A_1' = -\frac{q^2}{\gamma^2} A_1^2 \left(\frac{Z_{2,1}}{4} - \frac{Z_{2,3}}{4} + \frac{Z_{2,5}}{4}\right). \tag{9.4}$$

The approach discussed above also allows analyzing spatial distribution of harmonics near the resonance $\delta k = 2k_1 - k_2$, $|\delta k|/k_2 \ll 1$. In this case we have to assume that oscillations $\cos \delta kx$ and $\sin \delta kx$ are slow and keep the corresponding terms in (9.1,9.2). All other spatial oscillations can be averaged out. As a result we derive:

$$\begin{aligned}(Y_{1,1} &+ Y_{1,3})A_1' = -\frac{q^2}{4\gamma^2} A_1 A_2 \Big[(Z_{1,1} - Z_{1,3} + Z_{1,5}) \cos \delta kx \\ &+ (-Z_{1,2} + Z_{1,4} + Z_{1,6}) \sin \delta kx \Big], \end{aligned} \tag{9.5}$$

$$\begin{aligned}(Y_{2,1} &+ Y_{2,3})A_1' = -\frac{q^2}{2\gamma^2} A_1 A_2 \Big[(Z_{2,1} - Z_{2,3} + Z_{2,5}) \cos \delta kx \\ &+ (-Z_{2,2} + Z_{2,4} + Z_{2,6}) \sin \delta kx \Big]. \end{aligned} \tag{9.6}$$

The above equations can be easily rewritten in the form presented in Section 4.5.

Chapter 10

Appendix 2: Expressions for numerical derivatives

For the third harmonic numerical method discussed in Section 5.2, first derivatives are given by

$$P_1^{'} = \frac{4l_0^2q^2}{h_{ab}\gamma^2}\left[(\langle\cos\varphi_0\rangle - \omega^2)\psi_1 - \frac{\langle\sin\varphi_0\rangle}{2}\psi_1\psi_2 - \frac{\langle\cos\varphi_0\rangle}{8}\psi_1^3\right],$$

$$P_2^{'} = \frac{16l_0^2q^2}{h_{ab}\gamma^2}\left[(\langle\cos\varphi_0\rangle - 4\omega^2)\psi_2 - \frac{\langle\sin\varphi_0\rangle}{4}\psi_1^2\right],$$

$$P_3^{'} = \frac{36l_0^2q^2}{h_{ab}\gamma^2}\left[(\langle\cos\varphi_0\rangle - 9\omega^2)\psi_3 - \frac{\langle\sin\varphi_0\rangle}{2}\psi_1\psi_2 - \frac{\langle\cos\varphi_0\rangle}{24}\psi_1^3\right].$$

Second derivatives are given by

$$P_1^{''} = \frac{4l_0^2q^2}{h_{ab}\gamma^2}\begin{bmatrix} \langle\cos\varphi_0\rangle - \omega^2)P_1 + \langle\cos\varphi_0\rangle'(\psi_1 + \frac{1}{8}\psi_1^3) - \\ \frac{\langle\sin\varphi_0\rangle}{2}(P_1\psi_2 + P_2\psi_1) - \frac{\langle\sin\varphi_0\rangle}{2}'(\psi_1\psi_2) - \\ \langle\cos\varphi_0\rangle\left(\frac{3}{8}P_1\psi_1^2\right) \end{bmatrix},$$

$$P_2^{''} = \frac{16l_0^2q^2}{h_{ab}\gamma^2}\begin{bmatrix} \langle\cos\varphi_0\rangle - 4\omega^2)P_2 + \langle\cos\varphi_0\rangle'\psi_2 - \\ \frac{\langle\sin\varphi_0\rangle}{2}(P_1\psi_1) - \frac{\langle\sin\varphi_0\rangle}{4}'\psi_1^2 \end{bmatrix},$$

$$P_3^{''} = \frac{36l_0^2q^2}{h_{ab}\gamma^2}\begin{bmatrix} \langle\cos\varphi_0\rangle - 9\omega^2)P_3 + \langle\cos\varphi_0\rangle'(\psi_3 + \frac{1}{24}\psi_1^3) - \\ \frac{\langle\sin\varphi_0\rangle}{2}(\psi_1P_2 + \psi_2P_1) - \frac{\langle\sin\varphi_0\rangle}{2}'(\psi_1\psi_2) - \\ \langle\cos\varphi_0\rangle(\frac{1}{24}\psi_1^3) \end{bmatrix}.$$

For the sum and difference numerical method discussed in Section 6.2 the first derivatives are given by

$$d\psi_{1,2,+,-} = P_{1,2,+,-}dx,$$

$$P_{1,2}^{'} = \frac{q^2}{\gamma^2}\left[(\langle\cos\varphi_0\rangle - \tilde{\omega_{1,2}^2})\psi_{1,2}\right], \tag{10.1}$$

$$P_{+}^{'} = \frac{(q_1+q_2)^2}{\gamma^2}\left[(\langle\cos\varphi_0\rangle - (\omega_1 \tilde{+} \omega_2)^2)\psi_+ - \frac{\langle\sin\varphi_0\rangle}{2}\psi_1\psi_2\right], \tag{10.2}$$

$$P_{-}^{'} = \frac{(q_1-q_2)^2}{\gamma^2}\left[(\langle\cos\varphi_0\rangle - (\omega_1 \tilde{-} \omega_2)^2)\psi_- - \frac{\langle\sin\varphi_0\rangle}{2}\psi_1\psi_2\right]. \tag{10.3}$$

Second derivatives are given by

$$P''_{1,2} = \frac{q^2}{\gamma^2}\left[(\langle\cos\varphi_0\rangle - \tilde{\omega^2_{1,2}})P_{1,2} + \langle\cos\varphi_0\rangle'\psi_{1,2}\right], \tag{10.4}$$

$$P''_{+} = \frac{(q_1+q_2)^2}{\gamma^2}\left[\begin{array}{c} \langle\cos\varphi_0\rangle - (\omega_1 \tilde{+} \omega_2)^2)P_{+} + \langle\cos\varphi_0\rangle\psi_{+} \\ -\frac{\langle\sin\varphi_0\rangle}{2}(\psi_1 P_2 + P_1\psi_2) - \frac{\langle\sin\varphi_0\rangle'}{2}\psi_1\psi_2 \end{array}\right], \tag{10.5}$$

$$P''_{-} = \frac{(q_1-q_2)^2}{\gamma^2}\left[\begin{array}{c} \langle\cos\varphi_0\rangle - (\omega_1 \tilde{-} \omega_2)^2)P_{-} + \langle\cos\varphi_0\rangle\psi_{-} \\ -\frac{\langle\sin\varphi_0\rangle}{2}(\psi_1 P_2 + P_1\psi_2) - \frac{\langle\sin\varphi_0\rangle'}{2}\psi_1\psi_2 \end{array}\right]. \tag{10.6}$$